QC
1
U56
V.54
NO. 1

836
10v

Journal of Research

of the

National Bureau of Standards

JANUARY 1955

VOLUME 54 NUMBER 1

UNIVERSITY OF MICHIGAN
GENERAL LIBRARY

U. S. DEPARTMENT OF COMMERCE
Sinclair Weeks, Secretary
NATIONAL BUREAU OF STANDARDS
A. V. Astin, Director

JANUARY • 1953
VOLUME • 54
NUMBER • 1

JOURNAL OF RESEARCH

of the

NATIONAL BUREAU OF STANDARDS

PERIODICALS OF THE NATIONAL BUREAU OF STANDARDS

(Published monthly)

The National Bureau of Standards is engaged in fundamental and applied research in physics, chemistry, mathematics, and engineering. Projects are conducted in fifteen fields: electricity and electronics, optics and metrology, heat and power, atomic and radiation physics, chemistry, mechanics, organic and fibrous materials, metallurgy, mineral products, building technology, applied mathematics, data processing systems, cryogenic engineering, radio propagation, and radio standards. The Bureau has custody of the national standards of measurement and conducts research leading to the improvement of scientific and engineering standards and of techniques and methods of measurement. Testing methods and instruments are developed; physical constants and properties of materials are determined; and technical processes are investigated.

JOURNAL OF RESEARCH

The Journal presents research papers by authorities in the specialized fields of physics, mathematics, chemistry, and engineering. Complete details of the work are presented, including laboratory data, experimental procedures, and theoretical and mathematical analyses. Annual subscription: domestic, $4.00; foreign, $5.25.

TECHNICAL NEWS BULLETIN

Summaries of current research at the National Bureau of Standards are published each month in the Technical News Bulletin. The articles are brief, with emphasis on the results of research, chosen on the basis of their scientific or technologic importance. Lists of all Bureau publications during the preceding month are given, including Research Papers, Handbooks, Applied Mathematics Series, Building Materials and Structures Reports, Miscellaneous Publications, and Circulars. Each issue contains 12 or more two-column pages; illustrated. Annual subscription: domestic, $1.00; foreign, $1.35.

BASIC RADIO PROPAGATION PREDICTIONS

The Predictions provide the information necessary for calculating the best frequencies for communication between any two points in the world at any time during the given month. The data are important to all users of long-range radio communications and navigation, including broadcasting, airline, steamship, and wireless services, as well as to investigators of radio propagation and ionosphere. Each issue, covering a period of one month, is released three months in advance and contains 16 large pages, including pertinent charts, drawings, and tables. Annual subscription: domestic, $1.00; foreign, $1.25.

Order all publications from the Superintendent of Documents
U. S. Government Printing Office, Washington 25, D. C.

The printing of this publication has been approved by the Director of the Bureau of the Budget, May 12, 1953.

Journal of Research of the National Bureau of Standards Vol. 54, No. 1, January 1955 Research Paper 2559

Calibration of Meter Line Standards of Length at the National Bureau of Standards

Benjamin L. Page

The results of intercomparisons of the total lengths of several meter bars and of calibrations of the subintervals of some of these bars for the past twenty years are reported. Information both on the degree of stability of these standards and on the precision with which such measurements can be repeated was obtained. The results are critically analyzed and comments made as to the precautions necessary in the precision comparisons of line standards of length.

1. Introduction

It is known that the length of a linear standard, at any specified temperature, cannot be assumed to remain the same over a period of years. The changes in length may be attributed to secular changes, although these changes are not necessarily uniform throughout the length of any linear standard. It is essential, therefore, that linear standards be recalibrated at sufficiently frequent intervals so that these calibrations may be relied upon to the requisite accuracy in their use.

The standard length in the United States is Prototype Meter 27, kept at the National Bureau of Standards. In addition to this meter bar, the National Bureau of Standards has other line standards of length that are used as working standards, and nine of these were included in the calibrations described in this paper. To calibrate these standards, intercomparisons by pairs are made, using different combinations in order to determine the most probable corrections to their total lengths. As these intercomparisons require measurements of the highest accuracy, only one pair of bars can be compared on any one day. A complete intercomparison, therefore, requires an observing period of months, and these complete intercomparisons are made at intervals of several years. A previous paper [1] describes the determination of the total lengths of some of the present NBS standards and also the results of that and earlier intercomparisons.

Inasmuch as a complete intercomparison of 10 meter bars is a time-consuming labor, the question arises as to whether or not statistical methods would diminish this labor without significant loss of accuracy. This paper discusses this question and gives the analysis. It also reports the intercomparisons that have been made since the report in 1934 and shows the trends in the length changes of these bars. Redeterminations of the calibration corrections of some of the subintervals of the subdivided linear standards have also been made.

2. Description of meter bars

Nine meter bars were intercompared in 1952 and 1953, and the results of these comparisons are discussed. Four of these bars are made of platinum-iridium, one of 42 percent nickel-steel, three of invar, and one of stainless steel (Fe-Cr).

The four platinum-iridium bars have a modified X cross section generally referred to as the Tresca section; the others have the more familiar H cross section, and all intervals are defined by lines ruled on the plane of the neutral axis. When in use, each bar is supported at the Airy points, which are located 28.55 cm in each direction from the center of the bar.

Prototype Meter 27 is the primary standard of length of the United States, and meter 21 is a second bar of the same series. The other two platinum-iridium meters, 4 and 12, are of an earlier melt known as Alloy of 1874. The four nickel-steel bars are: Meter 39, made of invar, was obtained in 1903; meter 153R, made of 42 percent nickel-steel, with an inlaid platinum strip on which the graduations are ruled, was obtained in 1911; meter 814B, made of invar, was obtained in 1931; and meter 752, made of a type of invar termed "Fix Invar", was obtained in 1938. The other bar of this group, meter 50, is made of stainless steel and was graduated by C. G. Peters, formerly of the Bureau, by use of wavelengths of light.

The four nickel-steel bars were obtained from the Société Génevoise d'Instruments de Physique of Geneva, Switzerland, and are graduated at intervals of 1 mm throughout their lengths. Meter 4 is similarly graduated. Meters 27 and 21 have only the 1-m interval, which is defined as the interval from a central line of a group of three at one end to the central line of a similar group at the other end. Meter 12 was recently regraduated by C. G. Peters, while a member of the Bureau. Originally, this bar had rather inferior graduations at the terminal ends. This bar is considered as two linear standards for the purpose of these calibrations, because two 1-m intervals were graduated on it with a common zero; one interval is nominally correct at 0° C and the other at 20° C.

On all the bars subdivided to millimeters there is a 1-mm interval subdivided to tenths ruled outside of the terminal graduations. These may be conveniently used for the determination of the screw values of the micrometer microscopes.

Meter 50 has only a zero line and a 1-m line.

[1] Lewis V. Judson and Benjamin L. Page, J. Research NBS **13**, 757 (1934) RP743.

322661—55——1

On each bar two parallel lines approximately 0.2 mm apart are ruled at right angles to the graduations. Only that portion of a graduation lying between the two parallel lines is considered when measurements are made. These longitudinal lines are also very convenient when alining the bars in the comparator.

Table 1 gives coefficients of the linear thermal expansion of the meter bars, previously determined at the Bureau International des Poids et Mesures (BIPM) and the National Bureau of Standards (NBS). This table gives the values of a and b of the general equation

$$L_t = L_0(1 + at + bt^2), \qquad (1)$$

where L_t is the length of the bar at any temperature near 20° C, and L_0 is the length at 0° C.

TABLE 1. *Coefficients of expansion of the meter bars*

Meter bars [1]	Alloy	Coefficients of expansion	
		a	b
27	Platinum-iridium	8.6210×10^{-6}	$+0.00180\times10^{-6}$
4 (1874)	do	8.6014	+.00180
12 (1874)	do	8.6014	+.00180
21	do	8.6210	+.00180
39	Invar	1.54	
153R	42% nickel-steel	7.009	+.00083
752	Fix Invar	0.997	+.00402
814B	Invar	1.13	
50	Stainless steel (Fe-Cr)	10.25	

[1] Meters 27 and 21 are of the principal national series of prototypes; meters 12 and 4 of the alloy of 1874; meters 39, 153R, 752, and 814B have serial numbers of the Société d'Instruments de Physique; and meter 50 was graduated at the National Bureau of Standards. Meter 153R has an inlaid platinum strip on which the graduations are ruled.

3. Description of Longitudinal Comparator

The comparator (fig. 1) used in these calibrations is located in a constant-temperature room in the basement of the NBS South Building. It is mounted on a massive concrete pier whose upper surface is approximately 20 cm below the level of the floor of the room and entirely independent of it. This comparator is a longitudinal comparator; the relative motion of the microscope beam and of the bars being calibrated is in the direction longitudinal to the axis of the bars. In the NBS comparator the bars are stationary with their axes colinear, and a carriage with a beam bearing two microscopes is movable in a longitudinal direction. The microscopes may be clamped to the beam so that a simultaneous comparison of two bars may be made. Subdivisions of a bar up to 2 m in length (approximately 80 in.) may also be calibrated. The comparator has an over-all length of 4½ m.

The longitudinal movement of the carriage is effected by two electric motors geared to provide linear speeds of the carriage from 0.1 to 10 mm/sec. Automatic braking is provided so that the carriage can be stopped within a few microns of any desired position. An automatic cutoff is also provided for stopping the motion of the carriage to prevent its running off the ways of the bed. The total travel of the carriage is 130 cm.

The beam on which the microscopes are mounted is attached to the movable carriage through a system of self-alining ball bearings and a link, so that the beam will have a minimum strain resulting from any distortions of the carriage caused by longitudinal displacement of any magnitude up to 130 cm, regardless of the distance between microscopes.

The two microscopes have tubes approximately 45 mm in diameter and 450 mm in length and have provision for adjustment. The total magnification as used in these calibrations is approximately 160 diam. The smallest division of the micrometer drums is equivalent to 0.50 μ, measured at the focal plane of the microscope. By use of a vernier-scale adjacent to the micrometer drum, it is possible to estimate to 0.005 μ.

The graduations on the standards are illuminated by means of the vertical illuminators in the microscopes, using low-voltage lamps. Heat-absorbing glass installed between the lamps and microscopes greatly reduces the heat radiation from the lamps and therefore the temperature gradients within the bars being calibrated. Each microscope is mounted in a holder that can be moved along the ways of the beam, and may be securely clamped at any position. Also provided is a slow-motion mechanism for the longitudinal movement of the microscopes. The range in separation of the microscopes is from 15 to 210 cm.

Two main supports for the bars are provided, and each is capable of complete adjustment for focusing and alining the bars, so that the parallel longi-

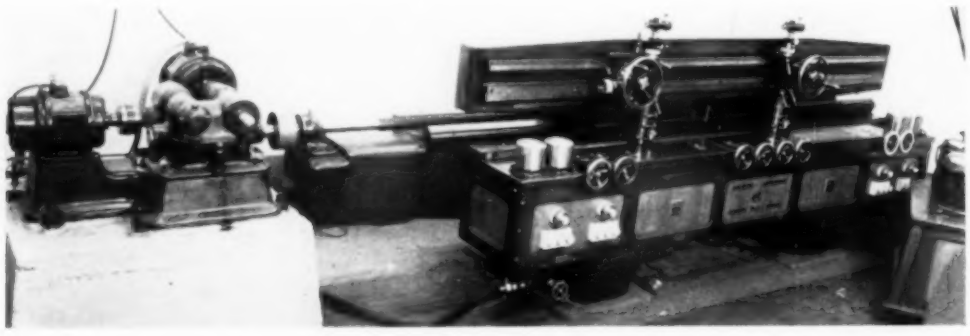

FIGURE 1. *Longitudinal comparator of the National Bureau of Standards.*

tudinal lines on the bars are parallel to the motion of the microscopes and are centrally located in the fields of the microscopes. Two adjustable roller supports, about 1 cm in diameter, are clamped to each of the main supports, with the proper separation, for supporting the bars. These supports are mounted in the inner of two tanks, which may serve as a double bath, the outer one being suitably insulated. Water may be used in either or both tanks and circulated by means of motor-driven propellers. Apertures, about 25 mm in diameter, are provided in the cover directly above the bar graduations that are under observation.

During the measurements the entire instrument is protected against external sources of heat by a thick quilted insulating cover, so that only the micrometer boxes are exposed.

4. Calibration of the Meter Bars

The latest fundamental measurements on this group of nine meter bars (considered as 10 for the purpose of these calibrations) were begun in 1952 and completed in 1953. The results of previous fundamental and auxiliary measurements of the total lengths of these bars, together with some repetitions of present measurements of some of the subintervals to show the stability of various standards over a period of years and the repeatability of present comparisons, are included in this paper. Another important part of the work was the calibration of certain of the subintervals of the bars subdivided to millimeters to provide accurate secondary standards for the calibration of line standards that are shorter than 1 m.

4.1. Determination of Total Length

All measurements on the bars were made on the longitudinal comparator, with the temperature of the room thermostatically controlled at 20° C. The bars were allowed to remain in the comparator for 24 hr, so that they would be in thermal equilibrium at a temperature very near 20° C before the measurements were begun. All measured differences in the lengths between any two bars were reduced to 20° C, by using the values for their respective coefficients of linear thermal expansion shown in table 1, before computing their respective corrections. For convenience, the corrections to the standards are given instead of the actual lengths. The actual length is equal to the nominal length plus the correction; hence, a plus correction indicates that a standard is longer than the nominal length.

Prior to the comparison in 1952 and 1953, the thermal conditions of the bars in the comparator were investigated. The temperature differences between bars, as indicated either by thermocouples or by mercury thermometers, were in agreement to approximately 0.005 deg C.

In order to determine the effect that water in the outer tank would have on the temperature of the bars in the inner tank, the outer tank was filled with water at nearly the same temperature as the bars. After the water had been circulated manually, there was no perceptible reduction in the temperature gradients within each bar nor was the difference in temperature less between the bars. The motors were then used to circulate the water for 2 min. Over the period of an hour after the motors had been turned off the temperature of the air rose 0.03 deg C, and the temperature of the bars remained constant. The conclusion is that the thermal conditions in this comparator are considerably less stable when the circulating bath is used, because of the heat generated by the motors.

The 10 bars selected for standardization were placed in the comparator, two at a time and in a random manner with respect to their relative positions, either to the right or to the left. To determine the magnitude of any possible bias because of the location of a standard in either the left or right end of the comparator, several auxiliary intercomparisons of groups of 5 and 6 of the bars were made. A special observing schedule suggested by the Statistical Engineering Section of the National Bureau of Standards, whereby the bars were mounted in a symmetrical manner, showed that there was possibly a small bias, which was considerably smaller than the reproducibility claimed for the measurements. All measurements were made with the bars in air at a controlled temperature of approximately 20° C, and no water was circulated in the outer tank.

To obtain the difference in length of two bars, two microscopes separated by a distance of 1 m were focused on the 0- and 1-m graduations of one of the bars. Micrometer observations were then made on this bar, the procedure being to record 2 observations on the left microscope, 4 on the right, and then 2 on the left. The carriage was then moved so that the microscopes were over the 0- and 1-m graduations of the other bar, and these graduations were brought into focus. Observations were then made on this bar. For convenience in computing, the bar at the right was always designated as A and the other as B. The comparisons between each pair of bars, A and B, were repeated 10 times, and the temperature of each bar was recorded. The procedure was to observe first on B, move the carriage to the right, observe on A, repeat the observations on A, return the carriage to the left, and observe on B. This cycle was repeated 5 times, and thus a total of 10 differences was obtained. The mean of these 10 differences was reduced to 20° C, and the difference in the length of the bars, $L=A-B$, thus determined. This method was continued until each bar had been compared with all others, and a total of $[N(N-1)]/2$, or 45 differences, had been determined. The results obtained are shown in table 2.

The reduction of these observed differences by the method of least squares was carried out by the use of the form[2] shown in table 3.

The differences, r, between the observed and calculated differences are shown in table 3. These

[2] A. Pérard and C. Volet, Les mètres prototypes du Bureau International, Travaux et Mémoires du Bureau International des Poids et Mesures **21**, (1945).

TABLE 2. *Differences in length of meter bars at 20° C*

(1953 series of comparisons)

Observations made at temperature, t, and reduced to 20° C, using the values of the coefficients of linear thermal expansion given in table 1.

Meter bars compared			Observed difference, L	Observed temperature, t	
				A	B
A		B	μ	°C	°C
4	minus	27	−4.33	19.87	19.78
12a[a]	minus	27	+0.87	20.13	20.03
12b[b]	minus	27	−171.93	20.17	20.05
21	minus	27	+5.11	19.96	19.88
39	minus	27	−177.13	19.89	19.81
153R	minus	27	−23.70	20.01	19.90
752	minus	27	−179.80	20.14	20.04
814B	minus	27	−170.34	19.93	19.89
50	minus	27	−171.40	20.07	20.01
12a[a]	minus	4	+5.36	19.86	19.84
12b[b]	minus	4	−167.68	19.88	19.90
21	minus	4	+9.36	19.89	19.89
39	minus	4	−172.88	20.06	20.04
153R	minus	4	−19.50	20.10	20.00
752	minus	4	−175.53	19.97	19.93
814B	minus	4	−165.99	20.13	20.05
50	minus	4	−167.19	19.87	19.86
12b[b]	minus	12a[a]	−173.01	19.81	19.81
21	minus	12a[a]	+4.33	20.10	20.10
39	minus	12a[a]	−177.99	19.72	19.74
153R	minus	12a[a]	−24.68	20.14	20.13
752	minus	12a[a]	−180.65	19.83	19.84
814B	minus	12a[a]	−171.40	19.89	19.90
50	minus	12a[a]	−172.56	20.09	20.10
21	minus	12b[b]	+177.36	20.12	20.13
39	minus	12b[b]	−5.01	19.74	19.75
153R	minus	12b[b]	+148.40	20.18	20.18
752	minus	12b[b]	−7.62	19.81	19.79
814B	minus	12b[b]	+1.96	19.90	19.91
50	minus	12b[b]	+0.50	20.05	20.05
39	minus	21	−182.36	20.13	20.13
153R	minus	21	−28.80	19.90	19.83
752	minus	21	−184.94	19.86	19.84
814B	minus	21	−175.46	19.96	19.95
50	minus	21	−176.45	19.95	19.95
153R	minus	39	+153.20	19.80	19.85
752	minus	39	−2.66	19.70	19.66
814B	minus	39	+6.96	20.06	19.93
50	minus	39	+5.66	20.04	20.05
752	minus	153R	−155.86	20.00	19.92
814B	minus	153R	−146.68	19.86	19.88
50	minus	153R	−147.62	19.99	19.96
814B	minus	752	+9.35	19.95	19.97
50	minus	752	+8.46	19.82	19.78
50	minus	814B	−1.03	19.98	19.95
Mean of all temperatures				19.95	

[a] Interval nominally correct at 0° C. [b] Interval nominally correct at 20° C.

45 residuals range from 0.02 to 0.20 μ and the average, neglecting sign, is 0.08 μ. The probable error of the calculated value of the differences in the corrections between any two bars, r, is given by the formula[3]

$$r=0.6745\sqrt{\frac{\sum v^2}{\frac{N}{N_t}(N-N_t)}}, \qquad (2)$$

where $\sum v^2$ is the sum of the squares of the residuals; N, the number of observational equations; and N_t, the number of unknowns. In the example considered, N_t is equal to 9 and N equal to 45. For the case given in table 3, r is calculated to be ± 0.03.

[3] T. W. Wright and J. F. Hayford, The adjustment of observations, p. 133, 137, 143, (1906).

During the period from 1933 to 1953, inclusive, seven series of determinations of the corrections to different groups of the 16-m bars under consideration were made. These determinations were made with groups of 7, 6, 7, 8, 9, 6, and 10 bars. All observations were made at approximately 20° C, and the results reduced to 20° C. The reductions of the observations were carried out by the method of least squares in all cases. The corrections to the total lengths of the bars, together with the new corrections for the prototype meter bars determined at the BIPM and authorized in 1933 by the Eighth General (International) Conference on Weights and Measures, are given in table 4.

The results of any auxiliary comparisons, made primarily because they served as checks in the interim between fundamental determinations, are not included in the table.

Several points should be noted in considering the data in table 4. The seven values determined for the corrections to meter 4 are consistently smaller than the value reported by BIPM, whereas 6 of the 7 values determined for meter 21 and 4 of the 5 values determined for meter 12, before regraduation, are larger than the values reported by BIPM. The differences between the corrections obtained by by NBS and those reported by BIPM for prototype meters 4, 12, and 21 are −0.22, +0.22, and +0.15 μ, respectively. If we disregard the 1936 and 1938 values for meters 12 and 21, respectively, the maximum range in the NBS corrections is 0.25 μ. The maximum range in the corrections for meter 4 is 0.22 μ.

Figure 2 shows the change in the determined correction to the total length of each of the two prototype meter bars, 4 and 21, from 1933 to 1953, inclusive, and of meter 12 from 1933 to 1947, inclusive, and from 1949 to 1953, inclusive.

From the above data it appears that there is considerable evidence that these three bars may have changed in length, two lengthening and one shortening, by about 0.2 μ since first received. It is rather difficult to state to what extent the differences between the BIPM and NBS values represent changes in the actual length of the bars. As the measurements at the NBS were made under most favorable conditions and with extreme care, it is believed that the NBS is justified in using the latest determinations instead of those obtained several decades ago, as representing the true value for the corrections to be applied to the respective meter bars when calibrating line standards of length submitted to the Bureau.

Referring again to table 4, it will be noted that the five laboratory standards of length, meters 39, 153R, 752, 814B, and 50, have changed in length during the 20-year period by a much greater amount than have the platinum-iridium meters. The three nickel-steel meters, 39, 153R, and 814B, and stainless steel meter 50 have continually elongated during this period, but Fix Invar meter 752 has shortened. The magnitudes of the changes in length between successive determinations, however, have generally

TABLE 3. *Calculations of corrections to meter bars at 20° C*

(1953 series of comparisons, using all 45 values for observed differences)

Directly observed differences of $A-B$ are taken from table 2. Calculated ("most probable") differences for $A-B$, given in parentheses, are derived by taking the differences of $\Sigma/10$; e. g., meter 4 − meter 27 = +84.97 − (+89.26) = −4.29μ, meter 12a − meter 4 = +90.22 − (+84.97) = +5.25μ, and meter 12b − meter 12a = −82.82 − (+90.22) = −173.04μ. Correction to meter 27 = +171.66μ at 20° C (BIPM certificate). Correction to bar = correction to meter 27 + (bar − 27). Length of bar = 1 m + correction. All values expressed in microns.

B \ A	27	4	12a[a]	12b[b]	21	39	153R	752	814B	50	Residuals, v
27	0	−4.33	+0.87	−171.93	+5.11	−177.13	−23.70	−179.80	−170.34	−171.40	−0.04
		(−4.29)	(+0.96)	(−172.08)	(+5.16)	(−177.11)	(−23.75)	(−179.75)	(−170.32)	(−171.42)	−.09
											+.15
											−.05
											−.02
4	+4.33	0	+5.36	−167.68	+9.36	−172.88	−19.50	−175.53	−165.99	−167.19	+.05
			(+5.25)	(−167.79)	(+9.45)	(−172.82)	(−19.46)	(−175.46)	(−166.03)	(−167.13)	−.05
											−.02
											+.02
											+.11
12a[a]	−0.87	−5.36	0	−173.01	+4.33	−177.99	−24.68	−180.65	−171.40	−172.56	+.11
				(−173.04)	(+4.20)	(−178.07)	(−24.71)	(−180.71)	(−171.28)	(−172.38)	−.09
											−.06
											−.04
											−.07
12b[b]	+171.93	+167.68	−173.01	0	+177.36	−5.01	+148.40	−7.62	+1.96	+0.50	+.04
					(+177.24)	(− 5.03)	(+148.33)	(−7.67)	(+1.76)	(+0.66)	−.06
											+.03
											+.13
						−182.36	−28.80				+.08
21	−5.11	−9.36	−4.33	−177.36	0			−184.94	−175.46	−176.45	+.03
						(−182.27)	(−28.91)				+.06
								(−184.91)	(−175.48)	(−176.58)	−.12
											−.18
							+153.20	−2.66	+6.96	+5.66	+.12
39	+177.13	+172.88	+177.99	+5.01	+182.36	0					+.02
							(+153.36)	(−2.64)	(+6.79)	(+5.69)	+.07
											+.05
											+.20
								−155.86	−146.68	−147.62	−.16
153R	+23.70	+19.50	+24.68	−148.40	+28.80	−153.20	0				−.09
								(−156.00)	(−146.57)	(−147.67)	+.11
											−.03
											+.02
									+9.35	+8.46	+.13
752	+179.80	+175.53	+180.65	+7.62	+184.94	+2.66	+155.86	0			−.16
									(+9.43)	(+8.33)	−.02
											+.17
											−.03
										−1.03	+.14
814B	+170.34	+165.99	+171.40	−1.96	+175.46	−6.96	+146.68	−9.35	0		−.11
										(−1.10)	+.05
											−.08
											+.13
											+.07
50	+171.40	+167.19	+172.56	−0.50	+176.45	−5.66	+147.62	−8.46	+1.03	0	
											$\Sigma v^2 = 0.4084$
											[c]P.E. = ±0.03
Σ	+892.65	+849.72	+902.19	−828.21	+944.17	−878.53	+655.08	−904.87	−810.57	−821.63	
Σ/10	+89.26	+84.97	+90.22	−82.82	+94.42	−87.85	+65.51	−90.49	−81.06	−82.16	
Bar − 27	0	−4.29	+0.96	−172.08	+5.16	−177.11	−23.75	−179.75	−170.32	−171.42	
Correction to bar	+171.66	+167.37	+172.62	−0.42	+176.82	−5.45	+147.91	−8.09	+1.34	+0.24	

[a] Interval nominally correct at 0° C. [b] Interval nominally correct at 20° C. [c] Probable error of the calculated value of the differences in the corrections between any two bars.

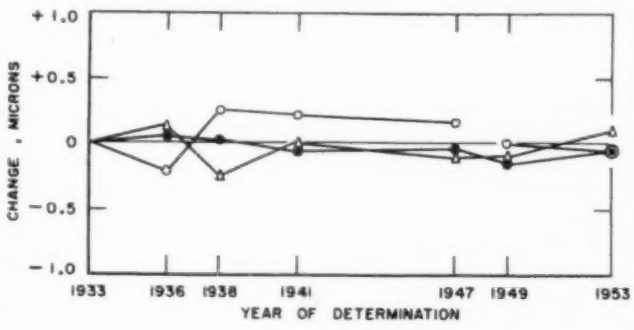

FIGURE 2. *Apparent change in lengths of bars.*

All values from fundamental determinations. ●, Meter 4; ○, meter 12; △, meter 21.

TABLE 4. *BIPM and NBS determinations of corrections to meter bars*

(1933 to 1953 series of comparisons)

Certified values reported by BIPM at 0° C and reduced to 20° C, using the respective values for their coefficients of linear thermal expansion shown in table 1. Correction to bar = correction to meter 27 + (bar − 27). All values expressed in microns.

Meter bars	Correction at 20° C									Differences					
	BIPM	NBS								Mean NBS − BIPM	NBS 1953 − 1933	NBS 1953 − 1938	NBS 1953 − 1947	NBS 1953 − 1949	NBS 1947 − 1933
	1933	1933	1936	1938	1941	1947	1949	1953	Mean						
27	+171.66	+171.66	.....	.....	+171.66	+171.66	+171.66	+171.66	+171.66	0.00	0.00	.....	.....	.....	.....
4 (1874)	+167.62	+167.44	+167.50	+167.44	+167.36	+167.39	+167.28	+167.37	+167.40	−.22	−.07	.....	.....	.....	.....
12 [a] (1874)	+176.09	+176.23	+176.02	+176.48	+176.45	+176.39	[b]	[b]	+176.31	+.22	.....	.....	.....	.....	+0.16
12a [c] (1874)	.....	.....	.....	.....	.....	.....	+172.59	+172.62	+172.60	.....	.....	.....	.....	+0.03	.....
12b [d] (1874)	.....	.....	.....	.....	.....	.....	−0.29	−0.42	−0.36	.....	.....	.....	.....	−.13	.....
21	+176.56	+176.74	+176.88	+176.48	+176.72	+176.64	+176.67	+176.82	+176.71	+0.15	+0.08	.....	.....	.....	.....
39	.....	−10.13	−9.17	−8.42	−8.00	−6.66	.....	−5.45	.....	.....	+4.68	.....	.....	.....	.....
153R	.....	+146.32	+146.77	+147.28	+147.38	+147.74	+147.82	+147.91	.....	.....	+1.59	.....	.....	.....	.....
752	.....	−0.95	−2.73	−3.23	−4.97	−7.05	.....	−8.09	.....	.....	−7.14	.....	.....	.....	.....
814B	.....	.....	.....	−0.56	−0.04	+1.10	.....	+1.34	.....	.....	.....	+1.90	.....	.....	.....
50	.....	.....	.....	.....	.....	−0.30	.....	+0.24	.....	.....	.....	.....	+0.54	.....	.....
Probable error [f]	.....	±0.05	±0.11	±0.04	±0.02	±0.02	±0.03	±0.03	.....	.....	.....	.....	.....	.....	.....

[a] Original graduations. [b] Regraduated. [c] Interval nominally correct at 0° C. [d] Interval nominally correct at 20° C. [e] The mean correction for the 1-m interval on meter 12a, graduated to be nominally correct at 0° C, is +172.60 μ, and the total expansion for a 1-m interval on this bar is 172.75 μ for a change in temperature of 20° C; hence, the correction to the interval is −0.15 μ at 0° C. [f] Probable error of the calculated value of the differences in the corrections between any two bars.

tended to decrease during the period from 1933 to 1953, as shown in figure 3.

How long a period might be required for these standards to become sufficiently stable to eliminate frequent standardizations is difficult to estimate. These laboratory standards are frequently used, between their restandardization, for measurements of moderate precision, where the changes in length over a comparatively short period of time are not significant. When they are used in measurements of the highest precision, they are compared with at least one platinum-iridium standard as a check on their assigned corrections.

The changes in the corrections during the periods between 1933 and 1938, 1938 and 1947, and 1947 and 1953, are shown in table 5.

Meter 39 is one of the first laboratory standards obtained by NBS, and it is of interest to note the average yearly change in length over a period of nearly a half century. The changes in length for this bar during the period from 1907 to 1953 are shown in figure 4. The average changes in length per year, for the first 4, the following 10, and the last 32 years, are +1.2, +0.6, and +0.2 μ, respectively. This shows that the magnitude of the changes in length is gradually becoming smaller.

TABLE 5. *Length changes of meter bars*

Meter bars	Average changes per year		
	1933 to 1938	1938 to 1947	1947 to 1953
	μ	μ	μ
39	+0.3	+0.2	+0.2
153R	+.2	+.1	<+.1
752	−.5	−.4	−.2
814B	.....	+.2	<+.1
50	.....	.....	+.1

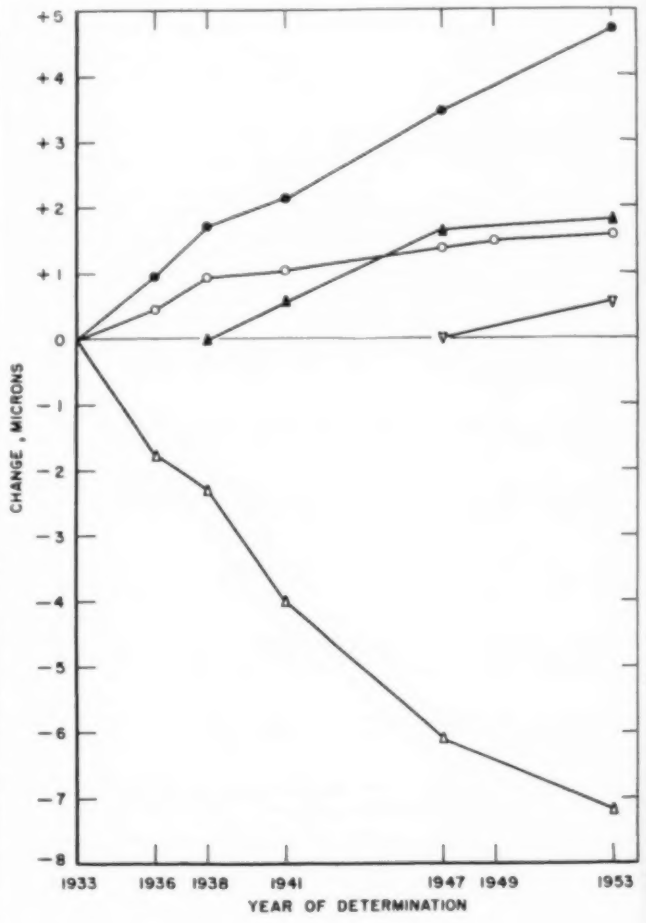

FIGURE 3. *Change in lengths of bars.*

All values from fundamental determinations. ●, Meter 39; ○, meter 153R; △, meter 752; ▲, meter 814B; ▽, meter 50.

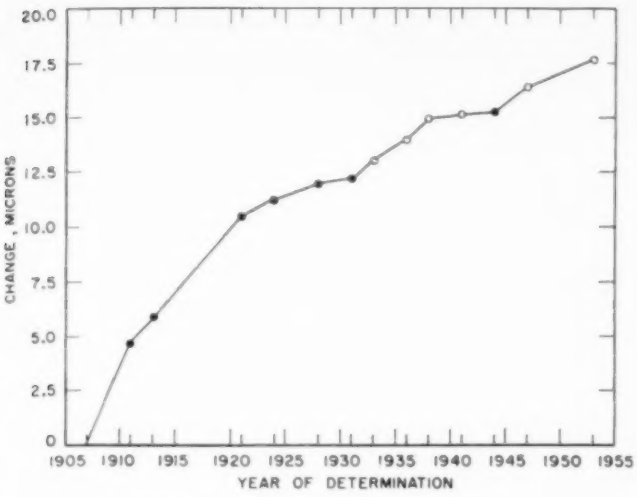

FIGURE 4.—*Change in length of meter 39.*

○, From fundamental determinations; ●, from check determinations.

As the work required to observe and determine 45 values for the differences between the lengths of a group of 10 standards is rather laborious and consumes considerable time, it was decided to use the information obtained in the 1952 and 1953 series of comparisons for a study of the possibility of using fewer measurements for future intercomparisons of the same number of standards.

According to a scheme,[4] calculations were made by using 30, 25, and 15 directly observed differences with the remaining differences computed from the observed values. The reduction of these differences, observed and computed, by the method of least squares was carried out by the use of forms (see footnote 2) shown in tables 6, 7, and 8.

The scheme for using 30 directly observed differences and selecting the remaining 15 to be computed is as follows:

Arrange the numbers of the 10-m bars as shown below.

*	27	4	12a	12b
27	*	21	39	153R
4	21	*	752	814B
12a	39	752	*	50
12b	153R	814B	50	*

Then cancel out the rows and columns that contain the number 27; this leaves the numbers 752, 814B, and 50 as the serial numbers of the bars whose differences from meter 27 are to be computed. Restore the rows and columns and next cancel out the rows and columns that contain number 4; this then leaves the numbers 39, 153R, and 50 as the numbers of the bars whose differences from meter 4 are to be computed. This procedure is continued until each number has been cancelled out of its respective rows and columns and until all the differences between the 15 pairs of bars, whose differences are to be computed from directly observed differences, are determined. To compute these differences, the following method, illustrated by 752—27, was used. First, the mean of the differences between 752 and each of the other bars with which it was directly compared and for which there is a corresponding directly observed comparison of that other bar with 27 was found. Next, the mean of the differences between 27 and each of the others with which it was compared, and for which there is a corresponding directly observed comparison of that other bar with 752, was found. Finally, the mean values were added algebraically. This is the computed value for 752—27, or −179.82 μ, as is shown in brackets in table 6. The other bracketed figures shown in table 6 were computed in a similar manner. All further computations to determine the corrections to the bars in this case are the same as in table 3.

The scheme for selecting and using 25 directly observed differences and for leaving the remaining 20 differences to be computed is as follows:

Arrange the numbers of the 10 bars as shown below.

Group 1	27	4	12a	12b	21
Group 2	39	153R	752	814B	50

The 25 directly observed differences to be used are those which are indicated by subtracting each of the numbers in group 1 from each of the numbers in group 2, i. e., 39—27, 153R—27, 752—27, 814B—27, 50—27, . . . , 50—21. The remaining 20 differences are computed in the same manner that was used when 30 directly observed differences were used, and are the bracketed figures shown in table 7. All further computations to determine the corrections to the bars in this case are the same as in table 3.

The scheme for using 15 directly observed differences and computing the remaining 30 differences is the opposite of the scheme for which the 30 directly observed differences were used and the remaining 15 computed. The 30 computed differences were obtained in the same manner that was used where 15 and 20 differences were determined, and are the bracketed figures shown in table 8. All further computations to determine the corrections to the bars in this case are the same as in table 3.

In computing the probable errors in tables 6, 7, and 8, the same formula (see footnote 3) was used as in table 3. This was done for simplicity, although the probable errors thus obtained may be somewhat too small. Alternative methods for computing the differences and probable error are given by Youden and Connor (see footnote 4).

The corrections to the bars obtained in the calibration in which all differences were directly observed, and those obtained when only 30, 25, and 15 were directly observed, are tabulated in table 9. The corrections to the various bars are in good agreement, even though a lesser number of direct differences were observed. This will be true only when all the

[4] W. J. Youden and W. S. Connor, New experimental designs for paired observations, J. Research NBS **53**, 191 (1954) RP2532.

observed differences in length between bars are accurately determined.

The values in columns 6 to 8 of table 9 were obtained by taking differences between the corresponding values in columns 3 and 2, 4 and 2, and 5 and 2, respectively. The average difference in the corrections (columns 6 to 8) increases with decrease in the number (30, 25, and 15) of directly observed differences. The conclusion is that in the comparison of basic standards, a full calibration, where all the differences between bars are directly observed, may be justified. However, for secondary standards or others submitted for calibration, a lesser number of direct comparisons should be sufficient.

TABLE 6. *Calculations of corrections to meter bars at 20° C*

(1953 series of comparisons, using 30 values for observed differences)

Directly observed differences of $A-B$ are taken from table 2 and are the values not in brackets or parentheses. Values in brackets have been computed from the directly observed differences. All further computations are the same as in table 3. All values expressed in microns.

A / B	27	4	12a[a]	12b[b]	21	39	153R	752	814B	50	Residuals, v
27	0	−4.33	+0.87	−171.93	+5.11	−177.13	−23.70	[−179.82]	[−170.26]	[−171.48]	0.00
		(−4.33)	(+0.96)	(−172.06)	(+5.13)	(−177.09)	(−23.73)	(−179.79)	(−170.34)	(−171.44)	−.09
											+.13
											−.02
											−.04
											+.03
4	+4.33	0	+5.36	−167.68	+9.36	[−172.82]	(−19.35)	−175.53	−165.99	[−167.12]	−.03
			(+5.29)	(−167.73)	(+9.46)	(−172.76)	(−19.40)	(−175.46)	(−166.01)	(−167.11)	+.08
											−.04
											+.07
											+.05
											−.10
12a[a]	−0.87	−5.36	0	−173.01	[+4.22]	−177.99	[−24.73]	−180.65	[−171.31]	−172.56	−.06
		+167.68	+173.01	(−173.02)	(+4.17)	(−178.05)	(−24.69)	(−180.75)	(−171.30)	(−172.40)	+.05
											−.07
											+.02
											−.01
											+.01
12b[b]	+171.93			0	[+177.18]	[−5.04]	+148.40	[−7.71]	+1.96	+0.50	+.05
					(+177.19)	(−5.03)	(+148.33)	(−7.73)	(+1.72)	(+0.62)	+.06
											−.04
											+.10
											−.01
											−.16
21	−5.11	−9.36	[−4.22]	[−177.18]	0	−182.36	−28.80	−184.94	−175.46	[−176.52]	−.01
						(−182.22)	(−28.86)	(−184.92)	(−175.47)	(−176.57)	−.01
											+.07
											+.02
											+.24
											−.12
39	+177.13	[+172.82]	+177.99	[+5.04]	+182.36	0	+153.20	−2.66	[+6.70]	+5.66	−.14
							(+153.36)	(−2.70)	(+6.75)	(+5.65)	+.06
											−.02
											+.01
											+.05
											−.16
153R	+23.70	[+19.35]	[+24.73]	−148.40	+28.80	−153.20	0	[−156.03]	−146.68	−147.62	+.04
								(−156.06)	(−146.61)	(−147.71)	−.05
											+.01
											+.03
											−.07
											+.09
752	[+179.82]	+175.53	+180.65	[+7.71]	+184.94	+2.66	[+156.03]	0	+9.35	+8.46	−.10
									(+9.45)	(+8.35)	+.11
											+.07
814B	[+170.26]	+165.99	[+171.31]	−1.96	+175.46	[−6.70]	+146.68	−9.35	0	−1.03	
										(−1.10)	$\Sigma v^2 = 0.2836$
											[c] P.E. $= \pm 0.03$
50	[+171.48]	[+167.12]	+172.56	−0.50	[+176.52]	−5.66	+147.62	−8.46	+1.03	0	
Σ	+892.67	+849.44	+902.26	−827.91	+943.95	−878.24	+655.35	−905.15	−810.66	−821.71	
Σ/10	+89.27	+84.94	+90.23	−82.79	+94.40	−87.82	+65.54	−90.52	−81.07	−82.17	
Bar−27	0	−4.33	+0.96	−172.06	+5.13	−177.09	−23.73	−179.79	−170.34	−171.44	
Correction to bar	+171.66	+167.33	+172.62	−0.40	+176.79	−5.43	+147.93	−8.13	+1.32	+0.22	

[a] Interval nominally correct at 0° C. [b] Interval nominally correct at 20° C. [c] Probable error of the calculated value of the differences in the corrections between any two bars.

TABLE 7. *Calculations of corrections to meter bars at 20° C.*

(1953 series of comparisons, using 25 values for observed differences).

Directly observed differences of A−B are taken from table 2 and are the values not in brackets or parentheses. Values in brackets have been computed from the directly observed differences. All further computations are the same as in table 3. All values expressed in microns.

A / B	27	4	12a [a]	12b [b]	21	39	153R	752	814B	50	Residuals, r
27	0	[−4.26]	[+0.98]	[−172.12]	[+5.13]	−177.13	−23.70	−179.80	−170.34	−171.40	−0.01
		(−4.25)	(+0.99)	(−172.12)	(+5.13)	(−177.12)	(−23.71)	(−179.76)	(−170.30)	(−171.47)	−.01
											.00
											.00
											−.01
4	[+4.26]	0	[+5.24]	[−167.86]	[+9.38]	−172.88	−19.50	−175.53	−165.99	−167.19	+.01
			(+5.24)	(−167.87)	(+9.38)	(−172.87)	(−19.46)	(−175.51)	(−166.05)	(−167.22)	−.04
											−.04
											+.07
											.00
											+.01
12a [a]	[−0.98]	[−5.24]	0	[−173.10]	[+4.14]	−177.99	−24.68	−180.65	−171.40	−172.56	.00
				(−173.11)	(+4.14)	(−178.11)	(−24.70)	(−180.75)	(−171.29)	(−172.46)	−.01
											−.04
											−.02
											+.06
											+.03
12b [b]	[+172.12]	[+167.86]	[+173.10]	0	[+177.25]	−5.01	+148.40	−7.62	+1.96	+0.50	+.01
					(+177.25)	(−5.00)	(+148.41)	(−7.64)	(+1.82)	(+0.65)	.00
											+.12
											+.02
											+.10
											−.11
21	[−5.13]	[−9.38]	[−4.14]	[−177.25]	0	−182.36	−28.80	−184.94	−175.46	−176.45	−.10
						(−182.25)	(−28.84)	(−184.89)	(−175.43)	(−176.60)	.00
											−.01
											−.01
											+.02
											+.14
39	+177.13	+172.88	+177.99	+5.01	+182.36	0	[+153.42]	[−2.63]	[+6.79]	[+5.65]	−.15
							(+153.41)	(−2.64)	(+6.82)	(+5.65)	−.11
											+.04
											−.05
											−.03
											+.15
153R	+23.70	+19.50	+24.68	−148.40	+28.80	[−153.42]	0	[−156.05]	[−146.59]	[−147.76]	+.01
								(−156.05)	(−146.59)	(−147.76)	+.01
											−.03
											.00
											.00
											.00
752	+179.80	+175.53	+180.65	+7.62	+184.94	[+2.63]	[+156.05]	0	[+9.46]	[+8.29]	.00
									(+9.46)	(+8.29)	.00
											.00
											.00
814B	+170.34	+165.99	+171.40	−1.96	+175.46	[−6.79]	[+146.59]	[−9.46]	0	[−1.17]	Σr^2=0.1432
										(−1.17)	[c] P. E.=±0.02
50	+171.40	+167.19	+172.56	−0.50	+176.45	[−5.65]	[+147.76]	[−8.29]	[+1.17]	0	
Σ	+892.64	+850.07	+902.46	−828.56	+943.91	−878.60	+655.54	−904.97	−810.40	−822.09	
Σ/10	+89.26	+85.01	+90.25	−82.86	+94.39	−87.86	+65.55	−90.50	−81.04	−82.21	
Bar −27	0	−4.25	+0.99	−172.12	+5.13	−177.12	−23.71	−179.76	−170.30	−171.47	
Correction to bar	+171.66	+167.41	+172.65	−0.46	+176.79	−5.46	+147.95	−8.10	+1.36	+0.19	

[a] Interval nominally correct at 0° C. [b] Interval nominally correct at 20° C. [c] Probable error of the calculated value of the differences in the corrections between any two bars.

TABLE 8. *Calculations of corrections to meter bars at 20° C.*

(1953 series of comparisons, using 15 values for observed differences)

Directly observed differences of $A - B$ are taken from table 2 and are the values not in brackets or parentheses. Values in brackets have been computed from the directly observed differences. All further computations are the same as in table 3. All values expressed in microns.

A / B	27	4	12a[a]	12b[b]	21	39	153R	752	814B	50	Residuals, v
27	0	[−4.21]	[+1.06]	[−172.18]	[+5.05]	[−177.30]	[−23.94]	−179.80	−170.34	−171.40	+0.09
		(−4.30)	(+0.89)	(−172.20)	(+5.14)	(−177.24)	(−23.83)	(−179.77)	(−170.38)	(−171.40)	+.17
											+.02
											−.09
											−.06
											−.11
4	[+4.21]	0	[+5.18]	[−167.87]	[+0.26]	−172.88	−19.50	[−175.36]	[−165.92]	−167.19	−.03
			(+5.19)	(−167.90)	(+9.44)	(−172.94)	(−19.53)	(−175.47)	(−166.08)	(−167.10)	+.04
											.00
											−.01
											+.03
											−.18
12a[a]	[−1.06]	[−5.18]	0	[−173.03]	+4.33	[−178.36]	−24.68	[−180.54]	−171.40	[−172.12]	+.06
				(−173.09)	(+4.25)	(−178.13)	(−24.72)	(−180.66)	(−171.27)	(−172.29)	+.03
											+.11
											+.16
											−.09
											+.06
12b[b]	[+172.18]	[+167.87]	[+173.03]	0	+177.36	−5.01	[+148.24]	−7.62	[+1.95]	[+0.91]	+.08
					(+177.34)	−5.04	(+148.37)	(−7.57)	(+1.82)	(+0.80)	−.23
											+.04
											+.12
											−.13
											+.17
21	[−5.05]	[−9.26]	−4.33	−177.36	0	[−182.37]	[−29.01]	[−184.98]	[−175.73]	−176.45	+.02
						(−182.38)	(−28.97)	(−184.91)	(−175.52)	(−176.54)	+.03
											−.13
											−.05
											+.13
											+.11
39	[+177.30]	+172.88	[+178.36]	+5.01	[+182.37]	0	[+153.38]	[−2.61]	+6.96	[+5.69]	+.01
							(+153.41)	(−2.53)	(+6.86)	(+5.84)	−.04
											−.07
											−.21
											+.09
											−.03
153R	[+23.94]	+19.50	+24.68	[−148.24]	[+29.01]	[−153.38]	0	−155.86	[−146.72]	[−147.69]	−.08
								(−155.94)	(−146.55)	(−147.57)	+.10
											−.15
											+.08
											−.17
											−.12
752	+179.80	[+175.36]	[+180.54]	+7.62	[+184.98]	[+2.61]	+155.86	0	[+9.46]	[+8.40]	+.07
									(+9.39)	(+8.37)	+.03
											−.04
											$\Sigma v^2 = 0.4775$
814B	+170.34	[+165.92]	+171.40	[−1.95]	[+175.73]	−6.96	[+146.72]	[−9.46]	0	[−1.06]	[c] P. E. $= \pm 0.03$
										(−1.02)	
50	+171.40	+167.19	[+172.12]	[−0.91]	+176.45	[−5.69]	[+147.69]	[−8.40]	[+1.06]	0	
Σ	+893.06	+850.07	+902.04	−828.91	+944.54	−879.34	+654.76	−904.63	−810.68	−820.91	
Σ/10	+89.31	+85.01	+90.20	−82.89	+94.45	−87.93	+65.48	−90.46	−81.07	−82.09	
Bar-27	0	−4.30	+0.89	−172.20	+5.14	−177.24	−23.83	−179.77	−170.38	−171.40	
Correction to bar	+171.66	+167.36	+172.55	−0.54	+176.80	−5.58	+147.83	−8.11	+1.28	+0.26	

[a] Interval nominally correct at 0° C. [b] Interval nominally correct at 20° C. [c] Probable error of the calculated value of the differences in the corrections between any two bars.

TABLE 9. *Summary of corrections to the total length of meter bars, using different numbers of directly observed differences*

(1953 series of comparisons)

1	2	3	4	5	6	7	8
Meter bars	Corrections at 20° C for various numbers of direct differences				Differences in corrections		
	45	30	25	15	30−45	25−45	15−45
	μ	μ	μ	μ	μ	μ	μ
27	+171.66	+171.66	+171.66	+171.66	0	0	0
4	+167.37	+167.33	+167.41	+167.36	−0.04	+0.04	−0.01
12a [a]	+172.62	+172.62	+172.65	+172.55	.00	+.03	−.07
12b [b]	−0.42	−0.40	−0.46	−0.54	+.02	−.04	−.12
21	+176.82	+176.79	+176.79	+176.80	−.03	−.03	−.02
39	−5.45	−5.43	−5.46	−5.56	+.02	−.01	−.11
153R	+147.91	+147.93	+147.95	+147.83	+.02	+.04	−.08
752	−8.09	−8.13	−8.10	−8.11	−.04	−.01	−.02
814B	+1.34	+1.32	+1.36	+1.28	−.02	+.02	−.06
50	+0.24	+0.22	+0.19	+0.26	−.02	−.05	+.02
Average difference					±0.02	±0.03	±0.05

[a] Interval nominally correct at 0° C.
[b] Interval nominally correct at 20° C.

5. Calibration of the Subintervals

Methods for the calibration of the subintervals of a standard of length have been described in Bureau Circular 329, Calibration of a Divided Scale, by Lewis V. Judson. In the recent calibrations of the subdivided meter bars, the methods described in Circular 329 have been used. In certain cases the method [5] of double or cross calibration has been used.

The calibration of the subintervals of subdivided meter bars 4, 39, 153R, 752, and 814B was carried out in four steps, namely, the decimeter intervals, the centimeter intervals of all of the decimeter intervals, the millimeter intervals of the 1- and 92-cm intervals, and the 1/10-m intervals at each end of the bars.

Because of these calibrations, it is possible to compare lengths from 0.1 mm up to and including 1 m with calibrated intervals on any of these five standards.

The results are expressed as "elements of calibration", that is, the corrections which the subintervals will have at a temperature at which the whole interval has its nominal length. Thus, it is only necessary to distribute proportionately any newly determined total correction to the elements of calibration in order to obtain the new corrections to the subintervals.

5.1. Calibration of the Decimeter Intervals

The computed values for the several elements of calibration of the decimeter intervals of the 5 meter bars are given in table 10. The probable errors of the calculated values for the elements of calibration

[5] C. E. Guillaume, L'étallonage des échelles divisées, Travaux et Mémoires du Bureau International des Poids et Mesures **13,** 1 (1907).

TABLE 10. *Elements of calibration of meter bars to decimeters*

(1953 series of calibrations)

Elements of calibration = corrections to intervals, assuming that the meter bars have their nominal lengths. Relative length of interval = nominal length + element of calibration.

Interval	Elements of calibration of meter bars—				
	4 [a]	39	153R	752	[a]814B
dm	μ	μ	μ	μ	μ
0 to 1	−0.46	−7.36	+1.41	+1.91	−0.76
0 to 2	−3.16	−1.39	+3.86	+4.18	−.54
0 to 3	+0.06	+0.98	+3.51	+3.60	−.74
0 to 4	−.60	+2.26	+4.09	+2.43	−.88
0 to 5	−2.36	−1.61	+5.36	+1.86	−.48
0 to 6	−2.28	+2.12	+2.37	+1.87	−.94
0 to 7	−1.58	−0.06	+2.82	+1.78	−.14
0 to 8	+0.08	−5.87	+4.84	+0.60	−1.56
0 to 9	−1.64	+0.94	+2.82	+.50	−1.25
0 to 10	0.00	.00	0.00	.00	0.00
Probable error range	±0.02 to ±0.03	±0.02 to ±0.03	±0.02 to ±0.03	±0.02 to ±0.03	±0.02 to ±0.03

[a] Mean of two calibrations.

are also shown. They were computed by using the formula [6]

$$r_x = 0.6745\sqrt{\frac{\sum v^2}{K}}, \qquad (3)$$

where $\sum v^2$ is the sum of the squares of the differences between the observed and computed values for the elements of calibration. As there are $(N-1)(N-2)$ equations of condition, K is $[(N-1)(N-2)]/2$, the value r_x is the probable error of any x, and x_2 is the element of calibration to the first interval, x_3 is the element of calibration to the first two intervals, x_4 is the element of calibration to the first three intervals, etc.

That the differences between the observed and calculated values for the elements of calibretion are relatively small is indicated by the small probable errors, and that all of the measurements are apparently of nearly equal accuracy, regardless of the character of the lines on the various bars, is indicated by the probable errors being of the same magnitude.

It is of interest to note how well the values for the elements of calibration of the decimeter intervals determined during the past 25 years agree with each other, and also to note the differences between the mean of these values and those obtained 50 years earlier. For this purpose, meter 39 was selected as an example, and the values determined in 1903 and those determined in 1928, 1931, 1932, 1947, and 1953 are given in table 11.

The maximum deviations from the mean of five determinations from 1928 to 1953, inclusive, range from 0.04 to 0.17 μ, the average being 0.11 μ.

The probable cause of some of the large differences between the mean of the 1928 to 1953 determinations and those determined in 1903 is that the old Saxton

[6] O. J. Broch, Note sur l'étalonnage des sous-divisions d'une règle, Travaux et Mémoires du Bureau International des Poids et Mesures **5,** 1 (1886).

TABLE 11. *Elements of calibration of meter 39 to decimeters*

(1903 to 1953 series of calibrations)

Elements of calibration = corrections to intervals, assuming that the meter bar has its nominal length. Relative length of interval = nominal length + element of calibration.

Interval	Elements of calibration in the year							Differences	
	1903	1928	1931	1932	1947	1953	Mean	Maximum deviation from mean	Mean − 1903
dm	μ	μ	μ	μ	μ	μ	μ	μ	μ
0 to 1	−7.43	−7.20	−7.38	−7.38	−7.20	−7.36	−7.30	0.10	+0.13
0 to 2	−1.45	−1.41	−1.48	−1.52	−1.28	−1.39	−1.42	.14	+.03
0 to 3	+1.10	+1.02	+0.95	+1.06	+0.87	+0.98	+0.98	.11	−.12
0 to 4	+2.29	+2.29	+2.25	+2.30	+2.23	+2.26	+2.27	.04	−.02
0 to 5	−1.48	−1.59	−1.56	−1.54	−1.48	−1.61	−1.56	.08	−.08
0 to 6	+2.42	+2.27	+2.25	+2.25	+2.36	+2.12	+2.25	.13	−.17
0 to 7	+0.29	+0.05	+0.02	+0.02	+0.22	−0.06	+0.05	.17	−.24
0 to 8	−6.13	−5.75	−5.85	−5.84	−5.62	−5.87	−5.79	.17	+.34
0 to 9	+0.72	+0.97	+0.95	+0.86	+1.11	+0.94	+0.97	.14	+.25
0 to 10	.00	.00	.00	.00	.00	.00	.00	.00	.00
Probable error range	±0.10 to ±0.11	±0.03 to ±0.04	±0.02 to ±0.03	±0.02 to ±0.03	±0.03 to ±0.04	±0.03 to ±0.04	------	----	------

comparator used in 1903 was not entirely adequate for the work. It is fortunate, however, that the values for the elements of calibration thereby determined are in fairly good agreement with those obtained by the use of more recent and better equipment.

5.2. Calibration of the Centimeter Intervals

In determining the elements of calibration to the centimeter subintervals, the double- or cross-calibration method was used, that is, a comparison of each interval with the others in all possible combinations; namely, the centimeter intervals of the first and sixth decimeters, those of the second and seventh, the third and eighth, the fourth and ninth, and the fifth and tenth.

5.3. Calibration of the Millimeter Intervals

The elements of calibration of the millimeter intervals of the centimeter intervals, 0 to 1 cm and 91 to 92 cm, were obtained by the same method as was used to determine the elements of calibration of the centimeter subintervals.

For the sake of brevity the results of the determinations of the elements of calibration of the subintervals of only meter 4 are reported in this paper. The two NBS calibrations for the decimeter, centimeter, and millimeter subintervals on meter 4, together with those reported in 1907 for the same subintervals by BIPM, are shown in table 12.

The probable errors for the elements of calibration of any centimeter or millimeter subinterval range from ± 0.03 to ± 0.07 μ, and were computed by the use of the formula [7]

$$r_x = 0.6745 \frac{\sqrt{2}}{(N-1)\sqrt{N-1}} \sqrt{\sum v^2}, \qquad (4)$$

[7] T. W. Wright and J. F. Hayford, The adjustment of observations, p. 133 and 142 (1906); Dziobek, Ueber die Ermittelung der inneren Theilungsfehler zweier Maassstäbe nach der Methode des Durchschiebens, Wiss. Abhandl Kaiserlichen Normal-Aichungs-Kommission **4**, 1 (1903).

TABLE 12. *Elements of calibration of meter 4 to millimeters at BIPM and NBS*

(NBS 1953 series of calibrations)

Elements of calibration = corrections to intervals, assuming that the meter bar has its nominal length. Relative length of interval = nominal length + element of calibration.

Interval	Elements of calibration			NBS mean [a]	NBS maximum deviation from mean	NBS − BIPM
	BIPM	NBS				
mm	μ	μ	μ	μ	μ	μ
0 to 1	−0.2	+0.01	−0.15	−0.07	0.08	+0.1
0 to 2	+.3	+.42	+.34	+.38	.04	+.1
0 to 3	−.8	−.56	−.67	−.62	.06	+.2
0 to 4	−1.1	−.72	−.78	−.75	.03	+.4
0 to 5	−1.3	−1.06	−1.05	−1.06	.01	+.2
0 to 6	−1.6	−1.31	−1.24	−1.28	.04	+.3
0 to 7	−1.8	−1.43	−1.41	−1.42	.01	+.4
0 to 8	−1.7	−1.45	−1.46	−1.46	.01	+.2
0 to 9	−1.8	−1.50	−1.55	−1.52	.03	+.3
0 to 10	−2.2	−1.93	−2.02	−1.98	.05	+.2
0 to 20	−2.5	−2.20	−2.37	−2.28	.09	+.2
0 go 30	−2.4	−2.30	−2.37	−2.34	.04	+.1
0 to 40	−0.8	−1.03	−1.09	−1.06	.03	−.3
0 to 50	−.7	−0.96	−0.90	−0.93	.03	−.2
0 to 60	−.9	−1.12	−1.22	−1.17	.05	−.3
0 to 70	−1.4	−1.60	−1.53	−1.56	.04	−.2
0 to 80	−1.2	−1.52	−1.36	−1.44	.08	−.2
0 to 90	−1.1	−1.24	−1.22	−1.23	.01	−.1
0 to 100	−0.5	−0.42	−0.49	−0.46	.04	.0
0 to 110	−.6	−.42	−.62	−.52	.10	+.1
0 to 120	−.4	−.31	−.53	−.42	.11	.0
0 to 130	−1.4	−1.28	−1.48	−1.38	.10	.0
0 to 140	−1.0	−0.98	−1.17	−1.08	.10	−0.1
0 to 150	−2.0	−2.02	−2.16	−2.09	.07	−.1
0 to 160	−3.7	−3.48	−3.66	−3.57	.09	+.1
0 to 170	−2.4	−2.15	−2.36	−2.26	.11	+.1
0 to 180	−1.3	−1.29	−1.39	−1.34	.05	.0
0 to 190	−2.3	−2.10	−2.16	−2.13	.03	+.2
0 to 200	−3.6	−3.11	−3.20	−3.16	.05	+.4
0 to 210	−3.0	−2.49	−2.64	−2.56	.08	+.4
0 to 220	−2.1	−1.63	−1.82	−1.72	.10	+.4
0 to 230	−2.0	−1.50	−1.85	−1.68	.18	+.3
0 to 240	−2.6	−1.95	−2.24	−2.10	.15	+.5
0 to 250	−2.2	−1.62	−2.05	−1.84	.22	+.4
0 to 260	−1.9	−1.20	−1.60	−1.40	.20	+.5
0 to 270	−2.0	−1.41	−1.77	−1.59	.18	+.4
0 to 280	−2.6	−2.16	−2.47	−2.32	.16	+.3
0 to 290	−1.8	−1.24	−1.53	−1.38	.15	+.4
0 to 300	0.0	+0.12	+0.01	+0.06	.06	+.1
0 to 310	+.4	+.60	+.58	+.59	.01	+.2
0 to 320	+.5	+.77	+.67	+.72	.05	+.2
0 to 330	+1.6	+2.02	+1.86	+1.94	.08	+.3
0 to 340	+0.2	+0.27	+0.17	+0.22	.05	.0
0 to 350	−2.9	−2.63	−2.88	−2.76	.13	+.1
0 to 360	−3.2	−2.73	−2.90	−2.82	.09	+.4

TABLE 12. *Elements of calibration of meter 4 to millimeters at BIPM and NBS*—Continued

Interval	Elements of calibration			NBS mean [a]	NBS maximum deviation from mean	NBS−BIPM
	BIPM	NBS				
mm	μ	μ	μ	μ	μ	μ
0 to 370	−1.7	−1.20	−1.46	−1.33	.13	+.4
0 to 380	−0.3	+0.06	+0.07	+0.06	.01	+.4
0 to 390	−.1	+.17	+.20	+.18	.02	+.3
0 to 400	−.8	−.59	−.61	−.60	.01	+.2
0 to 410	−.7	−.38	−.53	−.46	.08	+.2
0 to 420	−.4	−.21	−.21	−.21	.00	+.2
0 to 430	.0	+.24	+.18	+.21	.03	+.2
0 to 440	+.4	+.60	+.57	+.58	.02	+.2
0 to 450	−.2	−.16	−.10	−.13	.03	+.1
0 to 460	+.2	+.47	+.24	+.36	.12	+.2
0 to 470	−.4	−.26	−.44	−.35	.09	.0
0 to 480	+.3	+.48	+.36	+.42	.06	+.1
0 to 490	−2.1	−2.08	−2.20	−2.14	.06	.0
0 to 500	−2.3	−2.28	−2.43	−2.36	.08	−.1
0 to 510	−1.5	−1.28	−1.38	−1.33	.05	+.2
0 to 520	−0.7	−0.50	−0.57	−0.54	.04	+.2
0 to 530	−1.9	−1.81	−1.80	−1.80	.01	+.1
0 to 540	−3.0	−2.76	−2.67	−2.72	.05	+.3
0 to 550	−2.5	−2.25	−2.21	−2.23	.02	+.3
0 to 560	−2.1	−1.80	−1.76	−1.78	.02	+.3
0 to 570	−2.5	−2.32	−2.22	−2.27	.05	+.2
0 to 580	−2.1	−2.83	−2.80	−2.82	.02	+.3
0 to 590	−2.3	−2.05	−2.09	−2.07	.02	+.2
0 to 600	−2.5	−2.22	−2.35	−2.28	.07	+.2
0 to 610	−3.2	−3.09	−3.05	−3.07	.02	+.1
0 to 620	−3.9	−3.61	−3.67	−3.64	.03	+.3
0 to 630	−2.4	−2.05	−2.22	−2.14	.09	+.3
0 to 640	−1.2	−0.94	−1.16	−1.05	.11	+.2
0 to 650	−1.2	−.79	−0.98	−0.88	.10	+.3
0 to 660	−1.3	−1.04	−1.11	−1.08	.04	+.2
0 to 670	+0.4	+0.70	+0.56	+0.63	.07	+.2
0 to 680	−2.6	−2.21	−2.29	−2.25	.04	+.4
0 to 690	−3.1	−2.83	−2.80	−2.82	.02	+.3
0 to 700	−2.0	−1.55	−1.61	−1.58	.03	+.4
0 to 710	−1.1	−0.63	−0.88	−0.76	.13	+.3
0 to 720	+0.7	+1.24	+1.00	+1.12	.12	+.4
0 to 730	−.3	+0.14	−0.04	+0.05	.09	+.4
0 to 740	−.3	−.14	−.26	−.20	.06	+.1
0 to 750	−.6	−.21	−.43	−.32	.11	+.3
0 to 760	−.1	+.02	−.17	−.08	.10	.0
0 to 770	+.7	+.86	+.70	+.78	.08	+.1
0 to 780	+.6	+.60	+.50	+.55	.05	.0
0 to 790	+.8	+1.13	+.93	+1.03	.10	+.2
0 to 800	.0	+0.11	+.06	+0.08	.03	+.1
0 to 810	+.7	+.76	+.75	+.76	.01	+.1
0 to 820	−.5	−.14	−.34	−.24	.10	+.3
0 to 830	−1.5	−1.35	−1.55	−1.45	.10	.0
0 to 840	−0.5	−0.21	−0.38	−0.30	.09	+.2
0 to 850	+.3	+.53	+.33	+.43	.10	+.1
0 to 860	−.4	−.24	−.38	−.31	.07	+.1
0 to 870	−1.0	−1.04	−1.18	−1.11	.07	−.1
0 to 880	−0.8	−0.65	−0.69	−0.67	.02	+.1
0 to 890	−1.4	−1.36	−1.36	−1.36	.00	.0
0 to 900	−2.0	−1.61	−1.66	−1.64	.03	−.4
0 to 910	−3.1	−2.99	−2.79	−2.89	.10	+.2
0 to 911	−3.1	−3.12	−2.77	−2.94	.18	+.2
0 to 912	−3.2	−3.10	−2.81	−2.96	.15	+.2
0 to 913	−3.0	−2.89	−2.79	−2.84	.05	+.2
0 to 914	−3.2	−2.96	−2.80	−2.88	.08	+.3
0 to 915	−3.3	−3.10	−3.09	−3.10	.01	+.2
0 to 916	−2.8	−2.67	−2.59	−2.63	.04	+.2
0 to 917	−3.0	−2.73	−2.73	−2.73	.00	+.3
0 to 918	−3.0	−2.78	−2.74	−2.76	.02	+.2
0 to 919	−2.7	−2.58	−2.55	−2.56	.02	+.1
0 to 920	−2.6	−2.49	−2.40	−2.44	.05	+.2
0 to 930	−2.3	−2.13	−2.12	−2.12	.01	+.2
0 to 940	−2.6	−2.44	−2.48	−2.46	.02	+.1
0 to 950	−3.7	−3.67	−3.70	−3.68	.02	.0
0 to 960	−2.6	−2.48	−2.47	−2.48	.01	+.1
0 to 970	−1.7	−1.63	−1.56	−1.60	.04	+.1
0 to 980	−1.8	−1.68	−1.65	−1.66	.02	+.1
0 to 990	−2.3	−2.08	−1.98	−2.03	.05	+.3
0 to 1000	0.0	0.00	0.00	0.00	.00	0.0

[a] Mean of two calibrations.

where Σv^2 is the sum of the squares of the differences between the observed and computed values for the elements of calibration, N, the number of subintervals into which any considered interval is divided, and r_s is the probable error of the element of calibration of any subinterval.

The deviations from the mean of two determinations for all of the elements of calibration for meter 4 range from 0.00 to 0.22 μ, the average being 0.06 μ.

The discrepancies between the values originally reported by BIPM for these elements of calibration and the values determined by NBS vary from −0.3 to +0.5 μ. However, over a period of years repeated determinations of the elements of calibration of the decimeter subintervals on meter 4 have shown highly consistent results, and it is indicated, therefore, that the NBS values are very nearly the present true values for all of the elements of calibration for the subintervals. Taking into consideration that the NBS values were determined by using a comparator of more modern design, with more accurate auxiliary equipment and under more favorable conditions than were available in 1907 at BIPM, it is believed that the NBS is justified in adopting these new values as representing more nearly the true values than those originally determined.

5.4. Calibration of the One-tenth Millimeter Intervals

The 1/10-mm subintervals at each end of the meter bars were also calibrated by using the same double- or cross-calibration method used in the calibration of the centimeter and millimeter subintervals. The

TABLE 13. *Elements of calibration of the one-tenth millimeter intervals of meter 4*

(NBS 1953 series of calibrations)

Elements of calibration = corrections to intervals, assuming that the subdivided millimeter intervals have their nominal lengths. Relative length of interval = nominal length + element of calibration.

Interval	Elements of calibration		Mean	Deviation from mean
	First	Second		
mm	μ	μ	μ	μ
−1.0 to −0.9	−1.29	−1.34	−1.32	0.03
−.8	−1.04	−1.07	−1.06	.02
−.7	−1.18	−1.26	−1.22	.04
−.6	−0.83	−1.03	−0.93	.10
−.5	−.43	−0.56	−.50	.07
−.4	−.33	−.40	−.36	.04
−.3	−.07	−.14	−.10	.04
−.2	−.07	−.06	−.06	.01
−.1	−.24	−.14	−.19	.05
.0	.00	.00	.00	.00
1000.0 to 1000.1	−0.40	−0.45	−0.42	0.03
1000.2	−.04	−.04	−.04	.00
1000.3	−.27	−.41	−.34	.07
1000.4	−.71	−.66	−.68	.03
1000.5	−.60	−.58	−.59	.01
1000.6	−.45	−.42	−.44	.02
1000.7	−.37	−.37	−.37	.00
1000.8	−.30	−.37	−.34	.04
1000.9	−.29	−.30	−.30	.01
1001.0	.00	.00	.00	.00
Probable error	±0.04	±0.04	.....	.....

values determined for the elements of calibration for meter 4 are shown in table 13.

The probable error for the elements of calibration of any $\frac{1}{10}$-mm subinterval is ± 0.04 μ. The deviations from the mean of two sets of determinations range from 0.00 to 0.10 μ, the average deviation being 0.03 μ.

6. Conclusions

In making the measurements on the meter bars, the results of which are reported in this paper, every reasonable precaution was taken so that the results would reflect the accuracy and precision that is obtainable with the present NBS equipment.

In the comparison of the bars to determine their total corrections and the corrections to the subintervals, the smallness of the residuals indicates that the standards were in good thermal equilibrium while the observations were being made. Although the observations were made when the temperatures of the bars were very close to 20° C, the small residuals also indicate that the values used for their respective coefficients of linear expansion are very nearly the true values. In calibrating these meter bars, the effect of any error of 0.01 deg C in temperature varies from approximately 0.01 μ/m for the invar bars to 0.10 μ/m for the stainless steel (Fe–Cr) bar.

To a large extent the effect of the imperfections of the lines and surfaces of the bars was compensated for by sufficient repetitions of the observations. It is believed that the final correction to the total length of each of the standards calibrated is not in error by more than 0.2 μ, and in most cases is not in error by more than 0.1 μ.

There is no evidence that the lengths of the platinum-iridium bars have changed a significant amount during the past 20 years, whereas there is definite evidence that the other bars have changed. These changes, however, have become smaller during the ensuing years.

Regarding the possibility of making fewer measurements when intercomparing a group of standards, the 1952 and 1953 series of calibrations showed remarkably good agreement with the final corrections to the bars if a lesser number of direct differences had been considered. This could only be the case if the observed differences in length between the standards are all in excellent agreement. In the calibration of basic standards, a full calibration should be made where all differences between lengths of the bars are directly observed. However, where standards of a lower degree of accuracy are calibrated, a lesser number of direct comparisons would suffice.

As it is known that bars of many materials are unstable in length, the 1952 and 1953 series of comparisons continues the program of maintaining all line standards of length and of obtaining additional knowledge about them, so as to enable the NBS to meet the needs and demands of the present and future for increased accuracy.

The author expresses his appreciation to Lewis V. Judson, Chief, NBS Length Section, for his untiring assistance and guidance and for the many helpful suggestions through the years during which the data reported in this paper were obtained, and to John S. Beers for his assistance with recent observations and computations.

Washington, July 30, 1954.

Journal of Research of the National Bureau of Standards Vol. 54, No. 1, January 1955 Research Paper 2560

Enthalpy and Specific Heat of Four Corrosion-Resistant Alloys at High Temperatures

Thomas B. Douglas and James L. Dever

Specific heats that are believed to be accurate in general to within ±2 percent are reported for four alloys: from 0° to 900° C for 80 Ni-20 Cr and two stainless steels (type 347, containing 18 percent of chromium, 11 percent of nickel, and 1 percent of niobium, and type 446, containing 26 percent of chromium); and from 0° to 300° C for Monel, containing 67 percent of nickel and 30 percent of copper. These values were calculated from enthalpies measured with a drop method and a precision Bunsen ice calorimeter. The relatively small amounts of heat lost by the alloys as they dropped from the furnace to the calorimeter were estimated and corrections were applied therefor. Discontinuities in specific heat were found only in the case of 80 Ni-20 Cr and the stainless steel type 446.

1. Introduction

During the past several years the specific heats of a large number of substances have been measured precisely between 0° and 900° C at the National Bureau of Standards. In each case this involved measurements not only with the sample in a suitable container, but also with the empty container as well, in order to determine by difference the net effect of the sample alone. Each such container consisted of a thin-walled cylinder, ⅝ in. in diameter, and was usually composed of one of four alloys: 80 Ni-20 Cr, Monel, or stainless steel type 347 or 446 (Am. Iron & Steel Inst. designation). These alloys have numerous uses because of their relatively high resistance to corrosion, but apparently few measurements of their specific heats at elevated temperatures have been reported.

In the experiments recorded in this paper, the specimens used were themselves empty containers of the type previously used for measurements on other materials, such as aluminum oxide. The accuracy is somewhat less than in the earlier work because there is no cancellation of the small heat losses resulting from subtraction of blank measurements with an empty container. In addition, the following two factors should be pointed out, which, in the present case, somewhat limit the accuracy with which such measurements on only a few specimens can be applied to all specimens of the same general alloy: (a) As these four alloys are relatively hard materials, the previous thermal and mechanical history of a given specimen may sometimes cause it to exist in some less stable state that possesses a somewhat different specific heat; (b) a single name is often applied to a group of alloys whose chemical compositions, although nearly the same, are not exactly so. Fortunately, the specific heats of the main constituent elements of these four alloys are not very different, thus tending to reduce any error from this source. In fact, only in the temperature region of a transition or where two phases coexist does it seem likely that these factors may lead to serious lack of reproducibility in specific heat.

2. Experimental Procedure

Very detailed descriptions and evaluations of the method and apparatus used for measuring the enthalpy are contained in two papers [1] [1] and in a later paper [2], describing the modified form of apparatus used in the present work. In brief, the method consisted of heating the specimen in a furnace to each of several known temperatures and then dropping it into an ice calorimeter, by means of which the heat evolved in cooling the specimen to 0° C was measured. The specimen container (which was the actual specimen in the present work) was suspended in the furnace and calorimeter by a No. 32 wire of 80 Ni-20 Cr. This container and wire were connected by a short platinum-rhodium wire to which were attached two thin platinum disks that also entered the calorimeter. These disks greatly reduced upward loss of heat from the specimen. The helium inside the container, as well as a gold gasket in the case of 80 Ni-20 Cr, also entered the calorimeter during the drop. Helium was continuously passed through the cores of the calorimeter and the furnace, in order to reduce oxidation of the sample and to hasten the attainment of thermal equilibrium. The temperature of the furnace was kept constant during each run to within ±0.01 deg for a sufficient length of time to allow the sample to attain the same temperature. The temperatures were measured up to 600° C with a platinum resistance thermometer and above 600° C with a platinum–platinum-rhodium thermocouple, both of which had been calibrated in terms of the International Temperature Scale of 1948. The calibration factor of the ice calorimeter, which was based on numerous earlier electrical determinations at the Bureau, was taken to be 64.646 calories per gram of mercury (1 cal=4.1840 absolute joules).

Because, as mentioned above, these alloys were not themselves in containers, it was necessary to estimate and apply two small but appreciable corrections to each heat measurement, namely, for

[1] Figures in brackets indicate the literature references at the end of this paper.

TABLE 1. *Chemical compositions of the alloys*

Element	80 Ni-20 Cr	Monel sample—		Stainless steel—	
		1	2	347	446
	%	%	%	%	%
Iron	0.45	1.8	1.4	(a)	(a)
Nickel	77.4	67.1	66.7	11.1	0.32
Chromium	19.5	.....	.....	18.3	25.58
Copper	.....	29.3	30.4	.....	.....
Manganese	0.59	1.0	1.0	1.30	0.42
Niobium (columbium)	.....	.....	.....	0.86	.....
Silicon	1.4	0.07	0.07	.52	0.68
Carbon	0.04	.18	.12	.08	.23
Sulfur	.....	.....	.....	.....	.016
Phosphorus	.....	.....	.....	.....	.019
Total accounted for, %	99.4	99.4	99.7	.....	.....

a Not determined.

(a) the heat lost during the drop through the region between the furnace and the calorimeter, and (b) the heat delivered by the irrelevant parts of the system dropping into the calorimeter. The value used for the first correction was the mean of the calculated and observed values previously discussed [2].

The four alloys used were of commercial grade. In those cases where measurements were made with several specimens of the same alloy, the specimens were taken from adjacent parts of the same sample of rod or tubing. Except in the case of the Monel, which was stated to be in cold-drawn condition, they were heated to above 1,000° C and allowed to cool in air before beginning measurements of their enthalpy. Each specimen had a mass between 8 and 17 g, and carried with it into the calorimeter 0.3 to 0.5 g of platinum metals. The 80 Ni-20 Cr was accompanied also by 0.3 to 0.6 g of gold, and the other three alloys, by about 0.1 g of 80 Ni-20 Cr. In the course of the measurements, all the alloys except the Monel acquired oxide coatings in varying amounts up to a few hundredths of a gram. The thermal contributions of the small amounts of these irrelevant materials, which constitute correction (b) of the preceding paragraph, were estimated from specific-heat data in the literature and were corrected for by deduction from the results found.

A separate specimen of each alloy, taken from the same sample as those used in the thermal measurements, was analyzed chemically. The resulting compositions are given in table 1, and fall within the ranges of nominal composition for alloys of these designations [3].

3. Results

The enthalpy measurements were on two specimens of 80 Ni-20 Cr, on one each of Monel and stainless steel 446, and on six of stainless steel 347 (of which two were not run above 450° C). Several duplicate measurements were made on each specimen at each furnace temperature, the average deviation from the mean being 0.03 cal g^{-1}, or about 0.05 percent of the total heat measured. The different specimens of stainless steel 347 showed small differences that were systematic with temperature and averaged 0.25 percent of the measured heat. The corrected net heat values for the two specimens of 80 Ni-20 Cr, however, differed by approximately 1.5 percent at each furnace temperature. As this difference is many times the precision of the measurements, it is attributed to differences in the two specimens.

TABLE 2. *Mean corrected enthalpy*

Temperature	Corrected enthalpy, $H_t - H_0$, cal g^{-1}					Major corrections for stainless steel 446, cal g^{-1}	
	80 Ni-20 Cr specimen—		Monel	Stainless steel—			
	1	2		347	446	Pt, 80 Ni-20 Cr	Heat lost in drop
°C							
25.0	.....	.....	2.53	.....	.....	.....	.....
50.0	.....	5.23	5.09	.....	.....	.....	.....
75.0	.....	.....	7.72	.....	.....	.....	.....
94.0	10.11	9.98	.....	.....	.....	.....	.....
100.0	.....	.....	10.33	11.39	11.31	−0.17	+0.01
150.0	.....	16.26	15.65	.....	17.38	−.25	+.04
195.8	21.76	21.56	.....	.....	.....	.....	.....
200.0	.....	.....	21.10	23.49	23.72	−.34	+.07
250.0	.....	27.93	26.63	.....	30.28	−.42	+.10
298.3	34.12	33.71	.....	.....	.....	.....	.....
300.0	.....	.....	32.24	36.07	37.17	−.51	+.14
350.0	.....	.....	.....	.....	44.32	−.59	+.19
394.6	46.13	45.54	.....	.....	.....	.....	.....
400.0	.....	.....	.....	49.13	51.75	−.68	+.25
497.8	59.55	58.65	.....	.....	.....	.....	.....
500.0	.....	.....	.....	62.61	67.31	−.84	+.40
597.6	72.93	71.91	.....	.....	.....	.....	.....
600.0	.....	.....	.....	76.42	87.67	−1.01	+.61
699.5	87.92	86.45	.....	90.65	.....	.....	.....
701.2	.....	.....	.....	.....	106.19	−1.18	+.88
796.5	102.49	100.84	.....	104.98	121.95	−1.34	+1.22
860.0	.....	110.40	.....	.....	.....	.....	.....
896.0	118.00	115.88	.....	119.87	138.11	−1.51	+1.66

Relative to that at 0° C, the mean observed enthalpy at each furnace temperature, corrected as described above but unsmoothed, is given for each alloy in table 2. The mean values for the two specimens of 80 Ni-20 Cr are listed separately because of their considerable differences. In the last two columns are given (in calories per gram of alloy) the major corrections that were made to the values for stainless steel 446. The corresponding corrections for the other three alloys were very similar in magnitude.

The following equations, derived from the values of table 2, represent the relationship between enthalpy (in cal g^{-1}) and temperature (in deg C). The average departure of the observed values from these equations is about 0.02 cal g^{-1} (less than 0.1 percent). The equations for 80 Ni-20 Cr were derived from the mean values observed with the two specimens.

80 Ni-20 Cr:

$$H_t - H_0 = 0.1033t + 3.8(10^{-5})t^2 \quad (0° \text{ to } 150° \text{ C}). \quad (1)$$

$$H_t - H_0 = -0.33 + 0.1079t + 2.32(10^{-5})t^2 \quad (150° \text{ to } 600° \text{ C}). \quad (2)$$

$$H_t - H_0 = -4.37 + 0.1147t + 2.31(10^{-5})t^2 \quad (600° \text{ to } 900° \text{ C}). \quad (3)$$

Monel:

$$H_t - H_0 = 0.1010t + 2.20(10^{-5})t^2 \quad (0° \text{ to } 300° \text{ C}). \quad (4)$$

Stainless steel 347:

$$H_t - H_0 = 0.12508t + 1.703(10^{-5})t^2 - 9.31 \log_{10}[(t+273.2)/273.2] \quad (0° \text{ to } 900° \text{ C}). \quad (5)$$

Stainless steel 446:

$$H_t - H_0 = 0.10781t + 5.37(10^{-5})t^2 \quad (0° \text{ to } 500° \text{ C}). \quad (6)$$

$$H_t - H_0 = -6.83 + 0.16178t - 123{,}000(10^{-0.0078t}) \quad (600° \text{ to } 900° \text{ C}). \quad (7)$$

Differentiation of these equations leads to the following equations for the specific heat (in cal g^{-1} deg C^{-1}):

80 Ni-20 Cr:

$$C_p = 0.1033 + 7.6(10^{-5})t \quad (0° \text{ to } 150° \text{ C}). \quad (8)$$

$$C_p = 0.1079 + 4.64(10^{-5})t \quad (150° \text{ to } 600° \text{ C}). \quad (9)$$

$$C_p = 0.1147 + 4.62(10^{-5})t \quad (600° \text{ to } 900° \text{ C}). \quad (10)$$

Monel:

$$C_p = 0.1010 + 4.40(10^{-5})t \quad (0° \text{ to } 300° \text{ C}). \quad (11)$$

Stainless steel 347:

$$C_p = 0.1251 + 3.41(10^{-5})t - 4.04/(t+273.2) \quad (0° \text{ to } 900° \text{ C}). \quad (12)$$

Stainless steel 446:

$$C_p = 0.1078 + 1.074(10^{-4})t \quad (0° \text{ to } 500° \text{ C}). \quad (13)$$

$$C_p = 0.1618 + 2209(10^{-0.0078t}) \quad (600° \text{ to } 900° \text{ C}). \quad (14)$$

Specific-heat values calculated for even temperatures from eq (8 to 14) are listed in table 3.

The specific heats of the four alloys are shown graphically in figures 1 to 4. The lines represent the smooth values given by eq (8 to 14), and the points correspond to the unsmoothed corrected values calculated for short temperature intervals from pairs of successive values given in table 2.

The representation of the specific heat of 80 Ni-20 Cr by straight lines in figure 1 is convenient and within the accuracy of the data, which however do not justify the assumption of a real discontinuity in slope at 150° C. On the other hand, real discontinuities do appear for 80 Ni-20 Cr near 600° C (fig. 1) and for stainless steel 446 between 500° and approximately 650° C (fig. 4). Although the total enthalpy changes over these regions were measured as precisely as in the other cases, the exact variation of specific heat with temperature in these regions of transition was not established because the enthalpy measurements did not cover sufficiently small temperature intervals. Otherwise the smoothed specific heats represented by eq (8 to 14), table 3, and the lines in figures 1 to 4 are believed to be accurate within ±2 percent, at least for the actual specimens measured.

TABLE 3. *Specific heat (smoothed)*

Temperature	Specific heat, cal g^{-1} deg C^{-1}			
	80 Ni-20 Cr	Monel	Stainless steel—	
			347	446
° C				
0	0.1033	0.1009	0.1104	0.1078
25	.1052	.1021	.1123	.1105
50	.1071	.1033	.1142	.1132
100	.1109	.1054	.1176	.1185
200	1171	.1097	.1233	.1293
300	1217	.1142	.1283	.1401
400	.1264	----------	.1326	.1508
500	.1310	----------	.1370	.163
600	.14	----------	.1410	.21
700	.1470	----------	.1448	.1695
800	.1515	----------	.1487	1631
900	.1563	----------	.1525	.1620

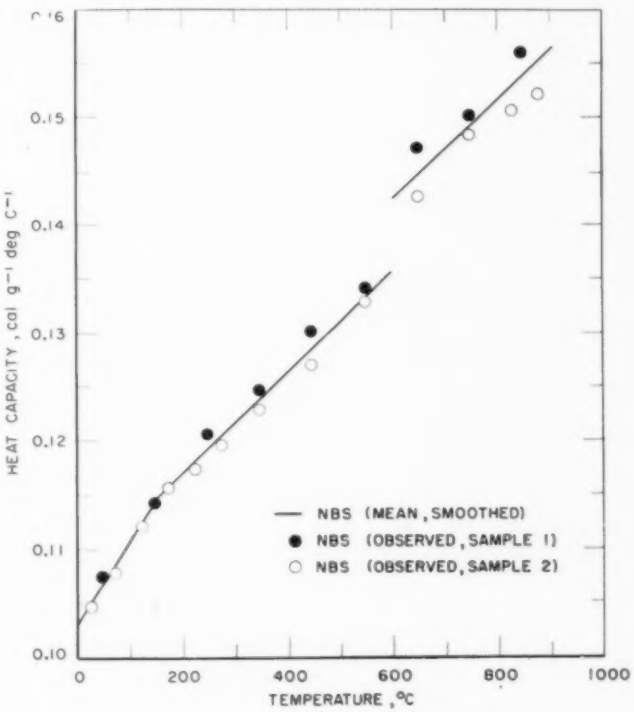

FIGURE 1. *Specific heat of 80 Ni-20 Cr.*

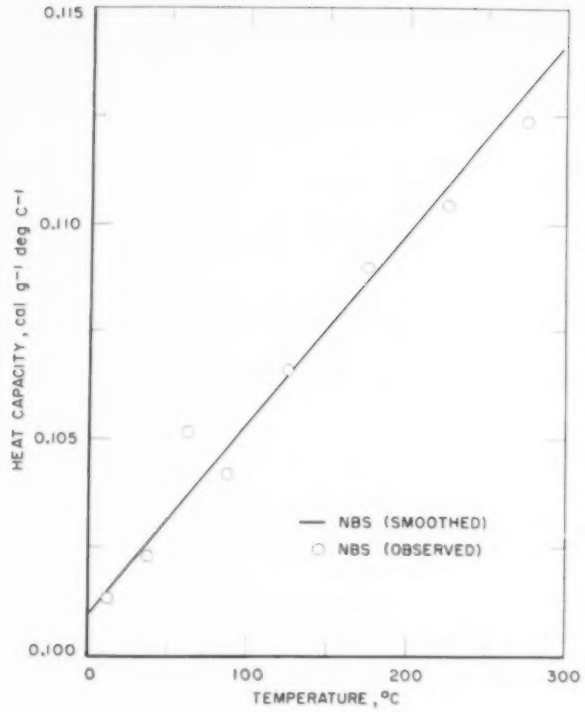

FIGURE 2. *Specific heat of Monel.*

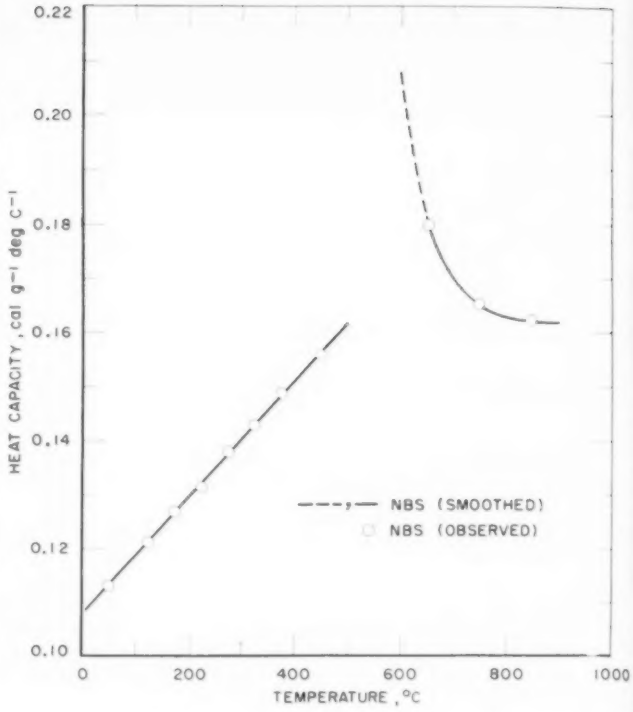

FIGURE 4. *Specific heat of stainless steel 446.*

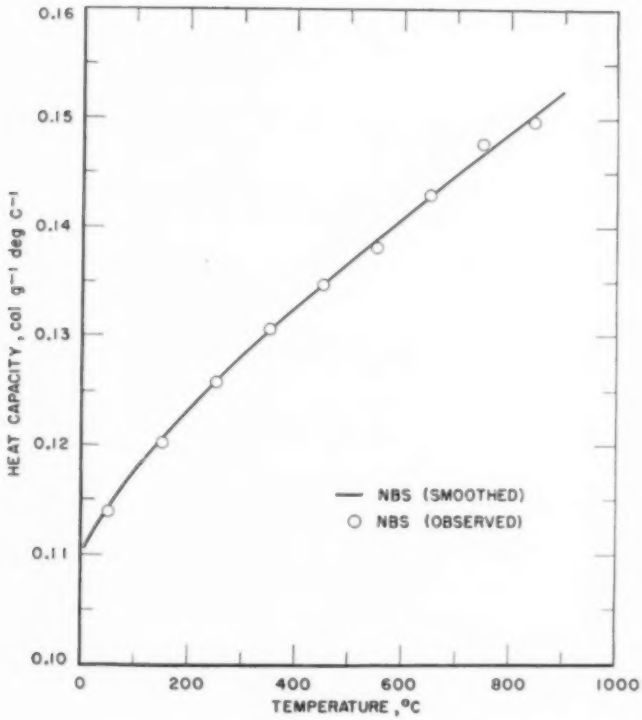

FIGURE 3. *Specific heat of stainless steel 347.*

4. Discussion

The following is a comparison of the specific-heat values (in cal g^{-1} deg C^{-1}) obtained in the present work with those given in reference [3]. A value of 0.107 given for 80 Ni-20 Cr [3, p. 1060], presumably near room temperature, is the same as that given for 50° C in table 3. For stainless steel 347, the average between 0° and 100° C is given as 0.120 [3, p. 566]; the present work gives a corresponding value 5 percent lower. For wrought stainless steel 446, 0.144 at 100° C is listed [3, p. 555]; the corresponding value of this paper for stainless steel 446 is about 20 percent lower. A value of 0.127 at 1,260° C is listed for standard Monel [3, p. 1049], but is not necessarily in disagreement with the present results, which extend up to only 300° C. Compared with a value for Monel of 0.0997 at 20° C, obtained with an adiabatic calorimeter [4], the present result is 2 percent higher.

A comparison of the specific heat found for stainless steel 347 with corresponding values measured at the National Physical Laboratory (London) [5] for a stainless steel of somewhat similar composition (8.14 percent of nickel, 19.11 percent of chromium, 0.37 percent of manganese, 0.68 percent of silicon, 0.08 percent of carbon, and 0.60 percent of tungsten) may be significant. The specific heats of the latter steel recorded in table 4 are the average values found for successive 50-deg intervals whose mean temperatures were those listed. The values given for stainless steel 347 were calculated from eq (12). Though the regularity in variation with temperature indicates the

absence of a transition in the case of stainless steel 347, the specific heat of the other steel shows, between 550° and 600° C, a small anomalous rise that is ordinarily attributed to some sort of transition.

The present investigation shows, over a temperature region above 500° C, a very marked increase in the specific heat of the particular sample of stainless steel 446 investigated. Though the details of this transition may depend somewhat critically on the exact chemical composition of the sample, it appears that the effect observed is to be associated with the magnetic-transformation point at approximately 600° C that has been reported for iron-chromium alloys of this composition [6].

Several investigators have found an anomalous behavior in a number of physical properties of 80 Ni-20 Cr in the temperature region just below and above 600° C. An abnormal change with temperature of the thermal expansion from 500° to 600° C was found [7], and a marked increase in the specific heat as the temperature rises above 500° C has been reported by others [8]. Recent measurements have been made of the specific electrical resistivity and specific heat of this alloy over the temperature range from 400° to 760° C [9]. These measurements show, with increasing temperature, a decrease of electrical resistivity and an anomalous increase in specific heat, tentatively explained by assuming that the alloy contained regions of very-short-range order whose number or size decreases as the temperature increases. The data indicated furthermore that the specific heat was somewhat less after the alloy had been quenched from 1,000° C than after it had been heated at 500° C and then cooled slowly.

The discontinuity in the specific heat of 80 Ni-20 Cr near 600° C shown in figure 1 represents a behavior not encountered in most transitions. As the temperature rises, the specific heat rather abruptly shifts to a higher, parallel line. Within the accuracy of the measurements, all the heat absorbed by the alloy is represented by the area under the curves. Since a "hump" such as that often found in the specific-heat curve of a substance in its transition region is missing, there is no heat of transition. In addition, more recent unpublished results obtained at the Bureau, which are considerably more precise than those on 80 Ni-20 Cr, unmistakably show similar behavior. These recent values are for two alloys manufactured under the trade name Inconel (approximately 8 percent of iron, 76 percent of nickel, 15 percent of chromium, and 0.05 percent of carbon), in which the amounts of the two major constituents are not greatly different from the amounts in 80 Ni-20 Cr.

The behavior of these alloys may be analogous to that of cobalt. On the basis of enthalpy measurements by a number of investigators, Kelley [10] gave the heat of its transition near 400° C as zero. This seems plausible, because according to X-ray analysis the transition is from a close-packed-hexagonal to a face-centered-cubic phase [11], a process that involves no change in atomic coordination number and only a slight change in the interatomic distance. It has similarly been found that the nickel-chromium alloys with less than 45 percent of chromium have a face-centered-cubic structure (presumably at room temperature) [12], and an explanation similar to that suggested for cobalt may hold in the case of 80 Ni-20 Cr.

TABLE 4. *Specific heat of two stainless steels of similar compositions*

Temperature	Specific heat, cal g^{-1} deg C^{-1}		
	19% Cr, 8% Ni (NPL)	Stainless steel 347 (NBS)	Difference
°C			
75	0.122	0.116	0.006
125	.126	.119	.007
175	.127	.122	.005
225	.129	.125	.004
275	.131	.127	.004
325	.134	.129	.005
375	.136	.132	.004
425	.139	.134	.005
475	.142	.136	.006
525	.150	.138	.012
575	.155	.140	.015
625	.151	.142	.009
675	.149	.144	.005
725	.150	.146	.004
775	.153	.148	.005
825	.155	.149	.006
875	.153	.151	.002

Most of the experimental work was supported by the Atomic Energy Commission. D. C. Ginnings, Anne F. Ball, and Ann W. Harman, of the National Bureau of Standards, assisted in making a large number of the measurements. The chemical analyses of the 80 Ni-20 Cr, Monel, and stainless steel 347 were performed by B. B. Bendigo, also of NBS. Stainless steel 446 and its chemical analysis were supplied by the Allegheny Ludlum Steel Corporation.

5. References

[1] D. C. Ginnings and R. J. Corruccini, J. Research NBS **38,** 583 (1947) RP1796; **38,** 593 (1947) RP1797.
[2] D. C. Ginnings, T. B. Douglas, and A. F. Ball, J. Research NBS **45,** 23 (1950) RP2110.
[3] Metals Handbook, Am. Soc. Metals (Cleveland, Ohio, 1948).
[4] W. F. Hampton and J. H. Mennie, Can. J. Research **7,** 677 (1932).
[5] The physical properties of a series of steels, part II, J. Iron Steel Inst. **154** (II) 83 P (1946).
[6] M. Hansen, Der Aufbau der Zweistofflegierungen, P. 522 (Julius Springer, Berlin, 1936).
[7] P. Chevenard, J. Inst. Metals **36,** 39 (1926).
[8] H. Grover and J. Hutzenlaub, Phys. Rev. **56,** 212 (1939).
[9] J. M. Hinkle, Microfilm Abstr. [1] **9,** 150 (University Microfilms, Ann Arbor, Mich., 1949).
[10] K. K. Kelley, Contribution to the data on theoretical metallurgy. X. High-temperature heat-content, heat-capacity, and entropy data for inorganic compounds, U. S. Bur. Mines Bull. **476,** 59 (U. S. Government Printing Office, Washington, D. C., 1949).
[11] S. B. Hendricks, M. E. Jefferson, and J. F. Schultz, Z. Krist. **73,** 376 (1930).
[12] S. Sekito and Y. Matsunaga, Kinzoku-no-Kenkyu [6] **6,** 229 (1929); J. Inst. Metals **42,** 514 (1930) (cf. Chem. Abstracts **24,** 3471 (1930)).

WASHINGTON, February 15, 1954.

Journal of Research of the National Bureau of Standards Vol. 54, No. 1, January 1955 Research Paper 2561

Effect of Temperature on the Tensile Properties of a Commercial and a High-Purity 70-Percent-Nickel–30-Percent-Copper Alloy

William D. Jenkins, Thomas G. Digges, and Carl R. Johnson

Short-time tensile tests were made at temperatures ranging from 75° to 1,700° F on two 70-percent-nickel–30-percent-copper alloys. The experimental evidence showed that discontinuous flow occurred in specimens of both alloys fractured in tension at temperatures ranging from 300° to 1700 F. This phenomenon was attributed to strain-aging at the lower temperatures and to recrystallization accompanied by grain growth at the higher temperatures. Variations in chemical composition of the two alloys also affected the degree of strain-aging, strength and ductility properties, and fracture characteristics.

1. Introduction

Tensile tests were made at temperatures ranging from 75° to 1,700° F on two lots of 70-percent-nickel–30-percent-copper alloys of the same initial grain size and structure but differing in purity. One alloy was of relatively high purity, whereas the other was a commercial grade that contained appreciable amounts of manganese, iron, and cobalt. The tensile properties of the high-purity alloy as evaluated at a lower range of temperatures (−320° to 212° F) have been investigated [1],[1] and a study of its creep behavior is now in progress.

2. Previous Investigations

The influence of temperature on the mechanical properties of commercial grades of 70-percent-nickel–30-percent-copper alloys (Monel) has been discussed in several publications [2, 3], but little information is available on the effect of impurities on these properties. An inspection of the results given in the tables [2] shows that the tensile strength of hot-rolled Monel increased as the test temperature was raised from 500° to 600° F without a corresponding decrease in elongation. However, in the range of 1,000° to 1,300° F there is a definite increase in brittleness, accompanied by a loss of strength. McVetty and Mochel [4] reported a precipitous drop in values for tensile strength and ductility of hot-rolled Monel as the test temperature was increased from 750° to 930° F.

Some creep properties of Monel have been reported by Bennett and McAdam [5], McAdam, Geil, and Woodard [6], Grant and Bucklin [7], Shahinian and Lane [8], and Betty, Eiselstein, and Huston [9]. Indications of the onset of intercrystalline fracture, aging, and discontinuity in temperature-ductility relations are evident in some of the results presented.

[1] Figures in brackets indicate the literature references at the end of this paper.

3. Alloys and Testing Procedures

The chemical composition of the alloys investigated is given in table 1.

The charges were melted in an induction furnace, and each alloy was cast into a 14- by 14- by 60-in. ingot. The ingots were milled, then forged to 8- by 8-in. blooms, hot-rolled to 2½-in. square billets, and then hot-rolled to ⅞-in. rounds. The round bars were annealed at 1,100° F. for 16 hr, then at 1,000° F for 8 hr. The alloys, as supplied by the manufacturer in the above condition, had an average grain diameter of 0.025 mm. The structures of these alloys are shown in figure 19, A and B.

Tensile specimens, 0.505-in. diameter and with 2.0-in. reduced sections, were machined from one bar of each alloy. Each specimen was heated in air in an automatically controlled electric furnace and held at the desired temperature for approximately 1 hr before testing in tension; the specimen was maintained within ±3 deg F of the desired temperature. The specimens were tested in a hydraulic-type machine, with the specimen and

TABLE 1. *Chemical composition (percentage by weight) of the alloys used*

Designation	Chemical composition					
	Ni	Cu	Mn	Fe	Si	C
High-purity	70.08	29.71	0.01	0.01	0.12	0.017
Commercial	66.97	29.79	.89	1.56	.17	.15
	S	Ca	Co	O_2	N_2	H_2
High-purity	0.002	(1)	(2)	0.001	0.0015	0.0003
Commercial	.006	0.017	0.38	.0001	None	.0001

[1] Faint trace.
[2] Not detected.

adapter occupying about 3 ft between two self-alining holders. The movement of the head during the test was recorded by means of a stress-strain recorder of the Templin type. Except for some specimens tested at 600° F, as noted in tables 2 and 3, the movement of the head of the machine was controlled to produce a rate of strain of about 1 percent a minute.

Hardness tests and metallographic examinations were carried out at room temperature on the fractured specimens in accordance with previously described procedures [10].

TABLE 2. *Results of tensile tests on high-purity 70-percent-nickel–30-percent-copper alloy*

Usual rate of strain, 1 percent a minute. Specimens at 600° F were tested (A) at usual speed, (B) to complete fracture in 21 min (speed test), (C) to complete fracture in 4 min (superspeed test).

Temperature	Yield strength (0.2% offset)	Drop of beam			Maximum load					Fracture strength	Elongation in 2 in.	Reduction of area	True strain at complete fracture [a]
		Stress at first drop of beam	Maximum drop		Tensile strength	True stress	Strain	Reduction in area	True strain				
			Stress at occurrence of	Amount of drop									
° F	lb/in.²	lb/in.²	lb/in.²	lb/in.²	lb/in.²	lb/in.²	%	%		lb/in.²	%	%	
75	26,500	None	None	None	67,350	94,550	40.4	28.8	0.339	304,900	59.1	88.4	2.150
212	25,250	None	None	None	63,050	85,200	35.1	26	.301	321,500	51	89.3	2.235
300	24,050	25,700	25,700	130	61,850	85,300	37.9	27.5	.321	277,900	52	88	2.113
500	23,600	25,350	60,800	1,370	60,800	83,500	37.3	27.2	.317	247,400	48.3	85.5	1.929
600 (A)	21,600	22,500	60,450	1,575	61,850	84,300	36.3	26.6	.309	221,500	51	85	1.894
600 (B)	22,500	22,700	50,000	1,625	60,400	83,100	37.5	27.3	.318	216,300	49	86	1.964
600 (C)	22,050	22,000	[b]	[b]	58,900	81,700	38.7	27.9	.327	263,700	50	85.7	1.948
700	23,400	23,400	24,400	875	59,950	81,250	35.5	26.2	.304	227,800	49.2	84.1	1.840
800	22,150	22,500	54,500	1,500	55,300	73,650	33.1	24.9	.286	190,300	45.2	81.7	1.698
900	19,950	33,000	33,000	500	50,050	65,800	31.4	23.9	.273	153,500	46.8	78.7	1.546
1,000	17,500	None	None	None	42,050	53,400	27	21.3	.239	98,300	47	71.6	1.257
1,100	16,700	None	None	None	37,400	38,450	22.5	17.9	.203	53,100	42	66.5	1.098
1,200	13,500	None	None	None	24,300	27,550	13.3	11.7	.125	26,800	37.5	58.1	0.869
1,350	9,700	15,700	15,700	25	15,800	17,700	12.1	10.8	.114	19,200	35	49.4	.681
1,500	5,750	10,250	10,250	50	10,300	11,250	9.2	8.4	.087	9,800	47	49	.671
1,700	4,500	1,625	5,650	125	5,850	6,600	13.4	11.8	.127	6,400	47.5	45	.598

[a] The true strain at complete fracture was based on the minimum cross-sectional area of the fractured specimen at room temperature.
[b] Not determined.

TABLE 3. *Results of tensile tests on commercial 70-percent-nickel–30-percent-copper alloy*

Usual rate of strain, 1 percent a minute. Specimens at 600° F were tested (A) at usual speed, (B) to complete fracture in 24.8 min (speed test).

Temperature	Yield strength (0.2% offset)	Drop of beam			Maximum load					Fracture strength	Elongation in 2 in.	Reduction of area	True strain at complete fracture [a]
		Stress at first drop of beam	Maximum drop		Tensile strength	True stress	Strain	Reduction in area	True strain				
			Stress at occurrence of	Amount of drop									
° F	lb/in.²	lb/in.²	lb/in.²	lb/in.²	lb/in.²	lb/in.²	%	%		lb/in.²	%	%	
75	42,000	None	None	None	88,250	121,500	37.7	27.4	0.319	194,200	51.8	71.1	1.241
212	38,650	None	None	None	83,600	110,100	31.7	24.1	.275	188,600	49	68.3	1.148
300	36,700	None	None	None	82,400	111,800	35.7	26.3	.305	208,400	48	71.2	1.247
500	35,500	35,600	81,250	350	87,200	120,400	38.1	27.6	.325	210,000	47.3	67.6	1.127
600 (A)	34,600	38,000	44,750	2,000	82,750	113,500	37.2	27.1	.316	162,500	48.6	63.8	1.016
600 (B)	34,850	36,500	80,500	375	83,600	113,900	36.3	26.6	.309	183,600	48	64.2	1.027
700	33,800	37,250	37,250	50	75,800	102,900	35.7	26.3	.305	179,200	45.5	67.7	1.131
800	31,950	None	None	None	66,650	86,300	29.4	22.7	.258	112,600	34.8	48.2	0.657
900	28,550	None	None	None	54,150	64,600	19.3	16.2	.175	80,500	27.3	34.3	.420
1,000	24,950	None	None	None	41,950	51,750	23.3	18.9	.209	63,900	27.3	36.4	.452
1,200	17,650	25,500	25,500	25	25,400	28,950	14	12.3	.131	31,600	33.5	55.2	.803
1,350	11,900	15,650	15,650	50	15,950	16,750	5.1	4.9	.051	16,500	28	40.1	.512
1,500	6,760	9,350	9,350	100	9,600	9,750	1.8	1.8	.018	6,700	24	26.2	.304
1,700	3,750	2,800	5,300	175	5,300	5,400	1.6	1.6	.016	5,000	22	18.3	.201

[a] The true strain at complete fracture was based on the minimum cross-sectional area of the fractured specimen at room temperature.

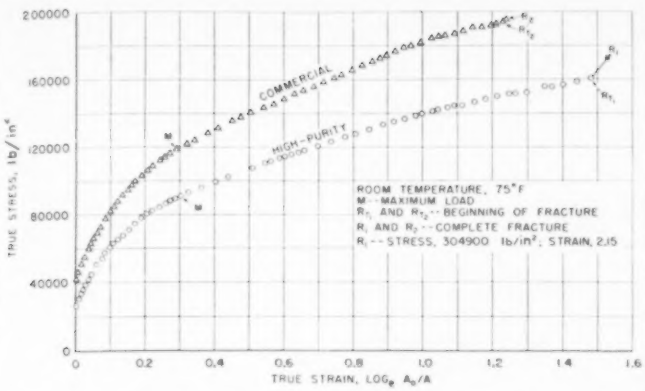

FIGURE 1. *Relation of true stress to true strain for the alloys tested in tension at room temperature.*

4. Results and Discussion

4.1. Mechanical Properties

The experimental results are summarized in tables 2 and 3 and in figures 1 to 22. A comparison of the flow characteristics in tension of the alloys at room temperature is obtained by observing the relative positions of the true-stress–true-strain [2] graphs in figure 1. The flow stresses at equal strains, stresses at maximum load (M) and at beginning of fracture (R_T), and rates of work-hardening were greater for the commercial than for the high-purity alloy. However, the true strains at maximum load and at the beginning of fracture and fracture strength [3] were correspondingly greater for the high-purity alloy.

Photographs of many of the autographic stress-strain records obtained on specimens of the alloys tested at different temperatures are reproduced in figures 2, 3, and 4. The rate of work-hardening varied with the amount of strain, the test temperature, and composition of the alloys. At the lower test temperatures, the slopes of the curves were relatively steep from the onset of plastic deformation to the maximum load. Precipitous drops in the curves in the region of maximum load to fracture are associated with necking of the specimens, whereas the flatness of some of the curves in this region is an indication of uniformity in deformation. At equal temperatures and strains, the rate of work hardening of the commercial alloy was usually somewhat higher than that of the high-purity alloy. Discontinuous flow occurred in many of the specimens as is indicated by the serrations in these curves. These serrations were often obtained both before and after the attainment of the maximum load on specimens of each alloy. Although the trend was for the serrations to attain a maximum in the specimens tested at 600° F, they were also observed in specimens tested at temperatures ranging from 300° to 900° F, and were considerably more noticeable in the stress-strain curves obtained on specimens of the high-purity alloy (fig. 2) than in the curves for the commercial alloy (fig. 3). Furthermore, increasing the speed of testing (table 2) by a factor of about 15 did not materially decrease the magnitude of serrations in the curves for the specimens of the high-purity alloy tested at 600° F (compare curves A and C, fig. 2). The serrations are believed to be associated with strain-aging and other atomic rearrangements.

Discontinuous flow was obtained in specimens of both alloys tested at the higher temperatures, as is illustrated in figure 4. The breaks in the stress-strain curves in the region of strains corresponding approximately from the drop of beam to nearly complete fracture are interpreted as being associated with recrystallization [4] and grain growth (fig. 20, E and F; fig. 21, C and D; fig. 22, E and F).

The effect of temperature on the yield strengths of the two alloys is shown in figures 5, 6, and 7. For the specimens tested at the usual rate, there appeared to be a continuous decrease in yield strength with increase in test temperature, with the exception of the specimens of high-purity alloy tested within the range of about 600° to 700° F (fig. 5). The slopes of these curves were continuously changing, however, and the magnitude of the change was affected significantly by the composition of the materials; yield strengths of each alloy at 1,500° or 1,700° F were approximately equal. Increasing the speed of application of load (points designated B) at 600° F raised the yield strengths slightly.

Certain investigators have indicated that a linear relationship exists between the yield strength and the reciprocal of the absolute (Kelvin) temperature when the experimental results are plotted on a linear or semilog (log of temperature) basis. The results obtained in the present investigation are plotted in these manners in figures 6 and 7, respectively. These assumptions were found to be approximately valid for limited ranges of temperature, but for each alloy there is a considerable difference between the slopes of the curves at high and at low temperatures. Moreover, at equal temperatures, there is also a difference in the slopes of the curves in each of the diagrams for the two alloys. This suggests that the activation energy for flow is not a simple function of the applied stress, but rather a complex function involving stress, temperature, and the size of the flow units activated by temperature.

The tensile strength of each alloy decreased with an increase in test temperature from 75° to 300° F (fig. 8). However, reversals were obtained in the

[2] The true stress was determined by dividing the current load by the current minimum cross-sectional area of the specimen. The true strain was determined as the natural logarithm of the ratio of the original cross-sectional area of the specimen (A_0) to the current minimum cross-sectional area (A).

[3] Fracture strength was determined by dividing the final load by the minimum cross-sectional area of the fractured specimen at room temperature.

[4] According to Patton (Metals Handbook, 1948, p. 1049), the commercial alloy recrystallizes at 1,220° and 1,110° F for 10- and 50-percent reduction of area, respectively.

tensile strength-temperature curves between 300° and 500° F for the commercial alloy, and between 500° and 600° F for the high-purity alloy. The tensile strength of each alloy decreased with a further increase in test temperature. Between 1,000° to 1,700° F, the tensile strengths of both alloys were nearly the same. The reversals are attributed to strain-aging, and the superior strength of the commercial alloy at the lower temperatures is considered as being due to impurities restricting the mean free path of the flow units within the grains.

Increasing the speed of testing at 600° F tended to decrease the tensile strength of the high-purity alloy and to increase slightly the tensile strength of the commercial alloy. These observations are also consistent with the concept that the impurities, acting as barriers, tended to increase the resistance to flow of the commercial alloy at the higher speeds.

The effect of temperature on the fracture strength (see footnote 3) is shown in figure 9. It should be pointed out that these values were affected by the necking characteristic (rim effect) of the alloys; the rim effect was more pronounced in the high-purity alloy than in the commercial alloy. The fracture strength of the high-purity alloy attained a maximum at 212° F. At the usual speed of testing, the strength then decreased as the test temperature was increased up to 600° F, increased slightly with a change in temperature from 600° to 700° F, and again decreased rapidly with further increase in temperature. The maximum fracture strength of the commercial alloy occurred at a higher temperature range (300° to 500° F), and then the general trend was about the same as for the high-purity alloy. At any selected test temperature below 1,100° F, the fracture strength of the high-purity alloy was higher than that of the commercial alloy. The fracture strength-temperature curves for the two alloys nearly coincide at temperatures ranging from 1,200° to 1,700° F.

Increasing the speed of testing from the normal to the intermediate rate used at 600° F (points B) resulted in raising the fracture strength of the commercial alloy, whereas the strength of the high-purity alloy was not materially affected by this change. However, the strength of the latter alloy increased markedly as the speed of testing was further increased (compare points B and C).

The relations between true stress and true strain at maximum load and at fracture are shown in figures 10 and 11, respectively. Strain-aging effects are again evident in the lower range of test temperatures. Although the trend was for the true strains at maximum load and at fracture to decrease as the true stresses decreased, and the temperatures were increased from 700° to 1,500° F for the high-purity

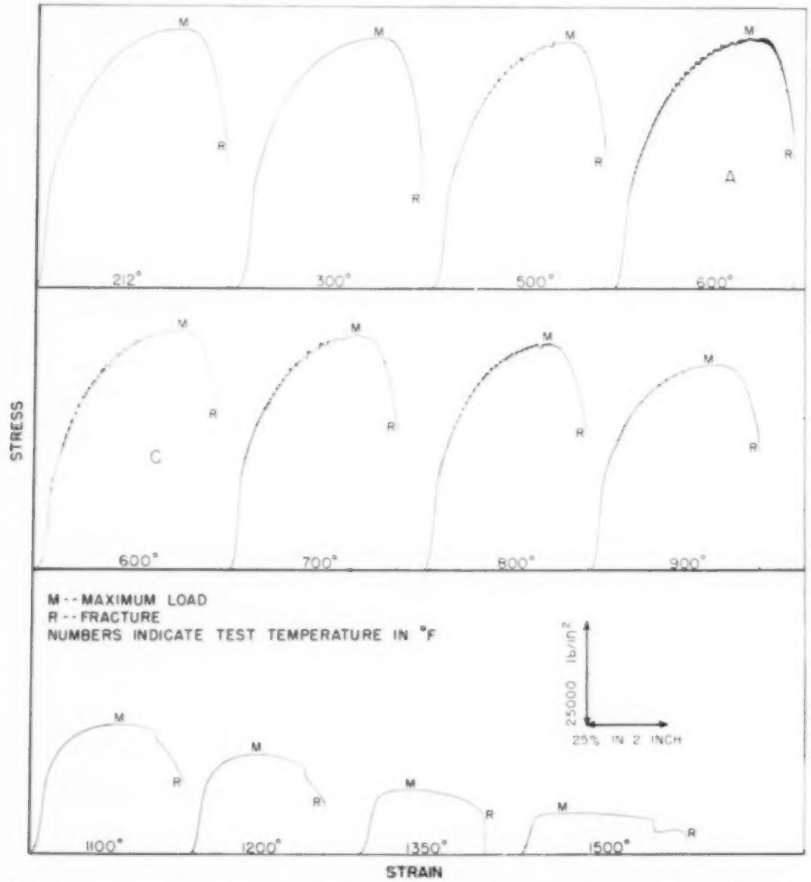

FIGURE 2. *Autographic stress-strain curves for specimens of the high-purity alloy tested in tension at different temperatures.*

alloy and from 700° to about 900° F for the commercial alloy, both curves for the latter alloy show reversals at a temperature of about 900° F.

The values obtained for strain at maximum load and elongation and reduction of area (tables 2 and 3) were not significantly affected by variation in test temperature from about 75° to 700° F (fig. 12); the values for strain and elongation for each alloy were somewhat higher at 75° F than the corresponding values at 212° F. The minima obtained in the ductility-temperature curves for specimens of the commercial alloy at a temperature of about 900° F are associated with the brittle behavior of this alloy at this temperature.

Variations in the range of speed of testing used at 600° F had no material effect on the ductility of the alloys.

The results of hardness tests made at room temperature on the specimens fractured at different temperatures are summarized in figures 13 and 14. The hardness increased continuously with the amount of deformation for the specimens of the high-purity alloy fractured at temperatures up to and including 1,000° F and also for the specimens of the commercial alloy at temperatures ranging from 75° to 800° F (fig. 13). With a further increase in temperature to about 1,200° F, the hardness at room temperature of each alloy was not significantly affected by the amount of plastic deformation. At test temperatures above 1,200° F, the hardness generally decreased as the amount of deformation increased; no marked change in hardness occurred in the specimen of the high-purity alloy, tested at 1,500° F with change in reduction in area from about 20 to 42 percent. The hardness–reduction-in-area curves for the specimens tested at 600° F are at a somewhat higher level than those for specimens tested at lower or higher temperatures. The curves of figure 14 also show that the maximum hardness of each alloy was obtained in the specimens fractured at 600° F. These curves (figs. 13 and 14) verify the fact that combination of strain-hardening and strain-aging predominated in the tensile tests carried out at temperatures ranging from about 75° to 800° or 1,000° F, whereas recovery and recrystallization predominated at temperatures in excess of 1,200° F.

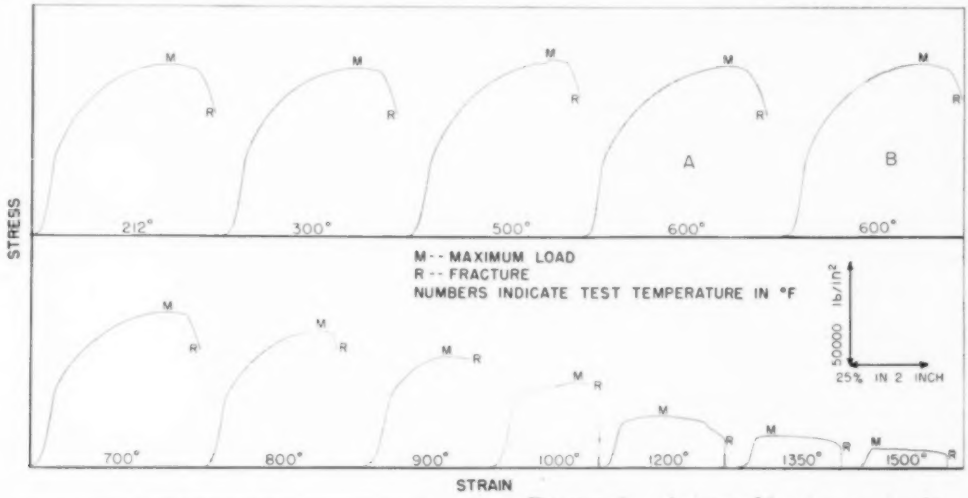

FIGURE 3. *Autographic stress-strain curves for specimens of the commercial alloy tested in tension at different temperatures.*

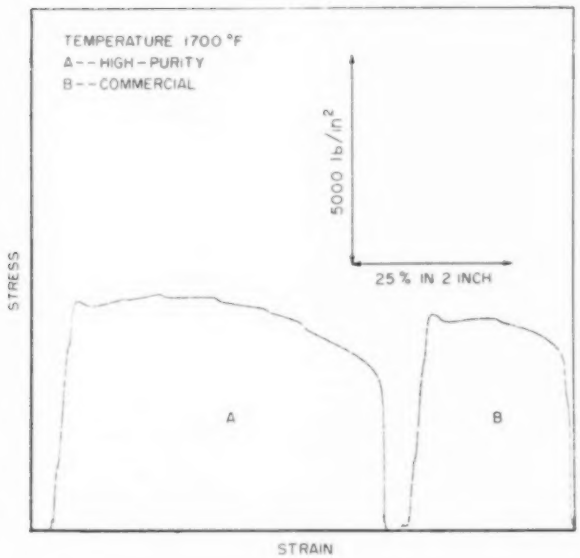

FIGURE 4. *Autographic stress-strain curves for specimens tested in tension at 1,700° F.*

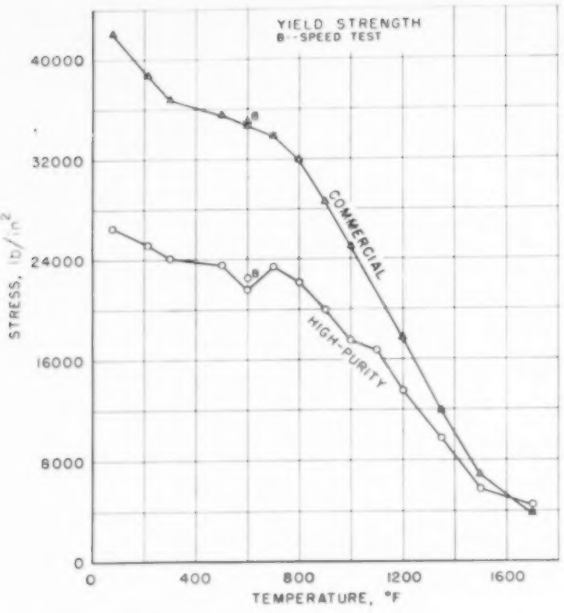

FIGURE 5. *Influence of temperature on the yield strength (0.2% offset) of the alloys.*

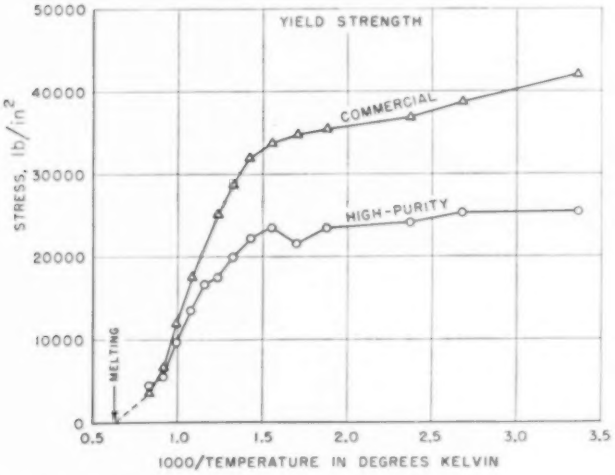

FIGURE 6. *Relation between the yield strength (0.2% offset) and the reciprocal of the temperature.*

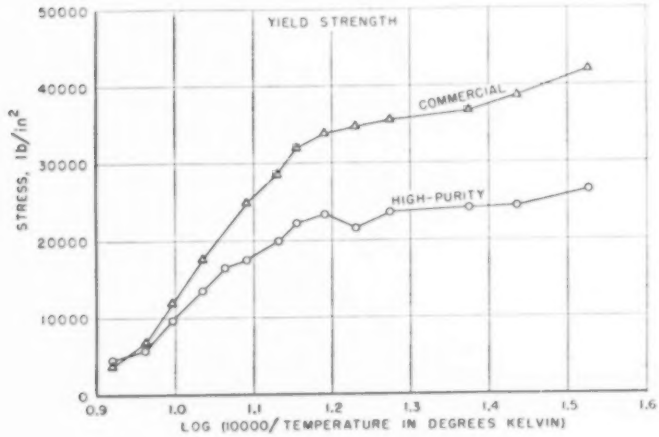

FIGURE 7. *Relation between the yield strength (0.2% offset) and logarithm of the reciprocal of the temperature.*

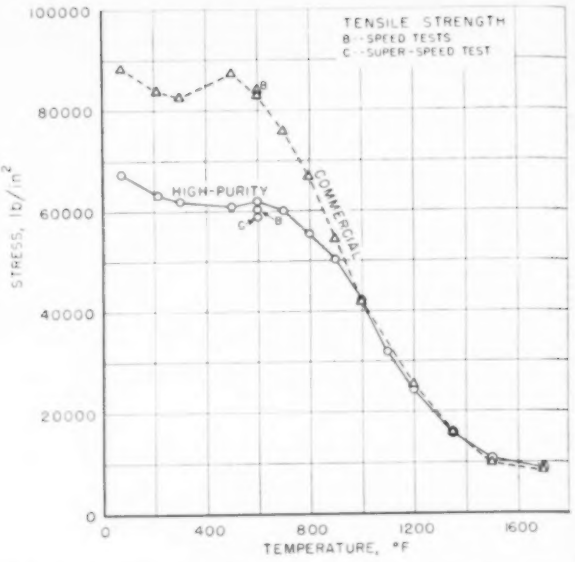

FIGURE 8. *Influence of temperature on the tensile strength of the alloys.*

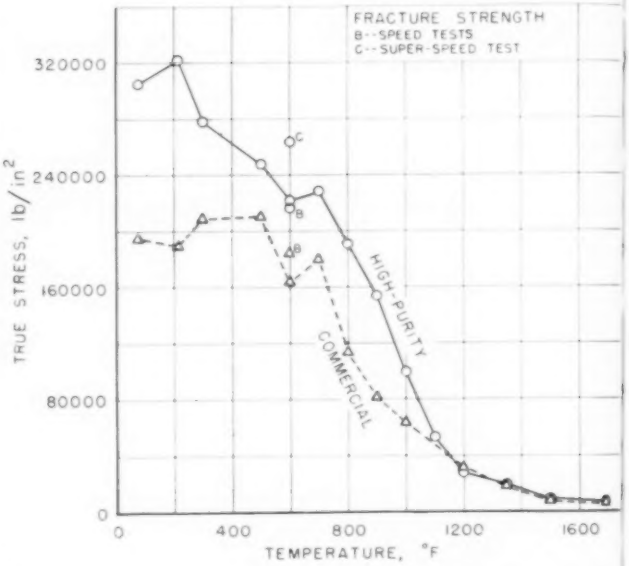

FIGURE 9. *Influence of temperature on the fracture strength of the alloys.*

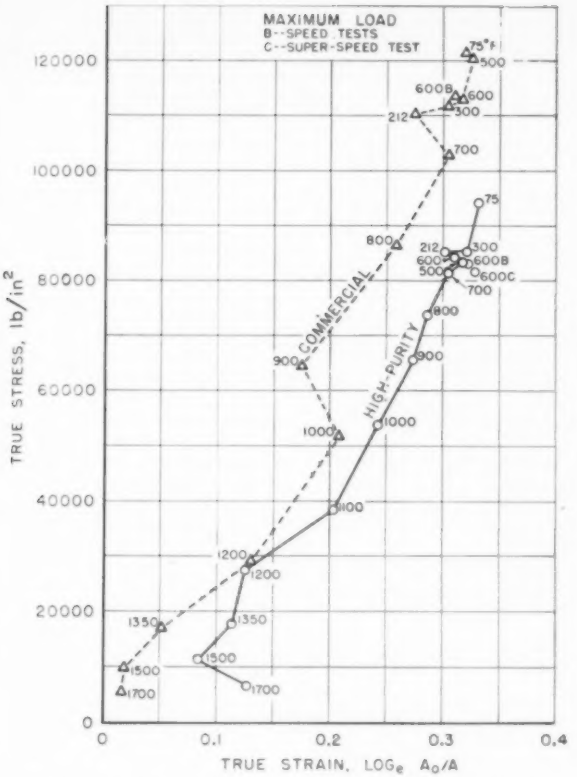

FIGURE 10. *True stress-true strain relations at maximum load as affected by temperature and strain rate for the alloys.*

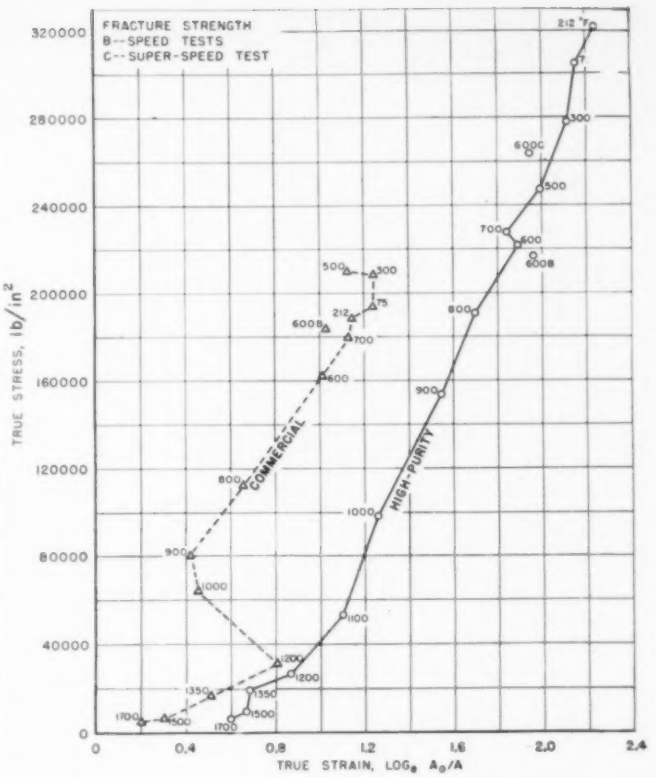

FIGURE 11. *True stress-true strain relations at fracture as affected by temperature and strain rate for the alloys.*

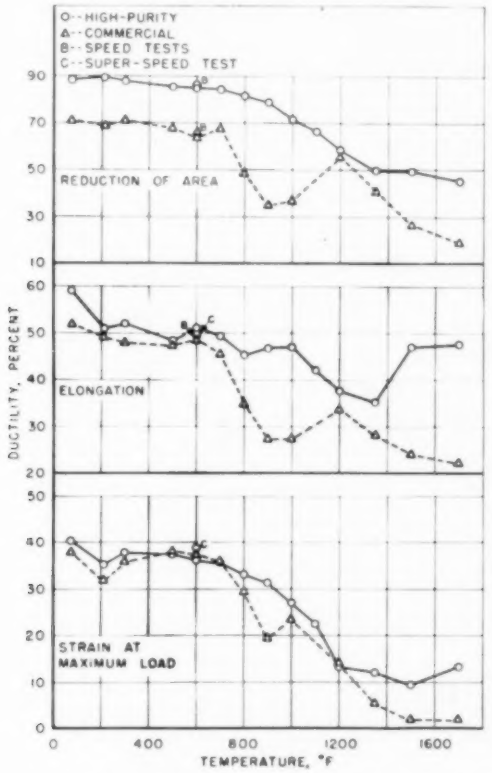

FIGURE 12. *Influence of temperature on the ductility at maximum load and at fracture.*

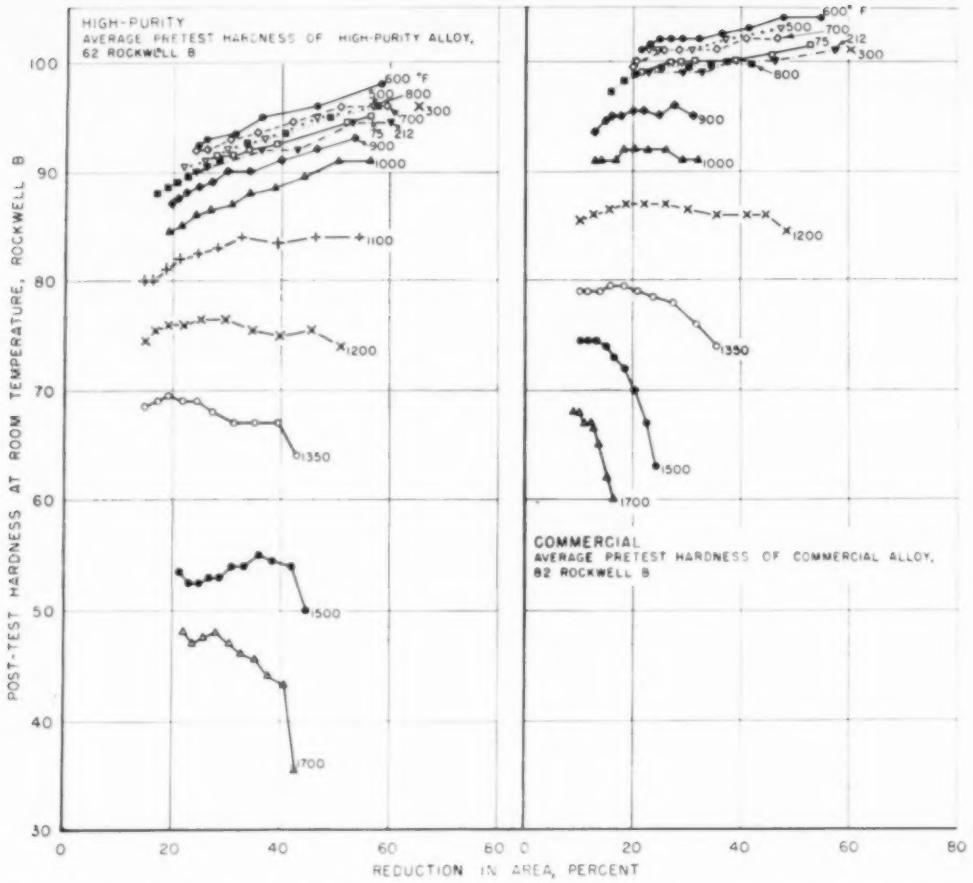

FIGURE 13. *Influence of reduction in area at different temperatures on the hardness of the alloys at room temperature.*

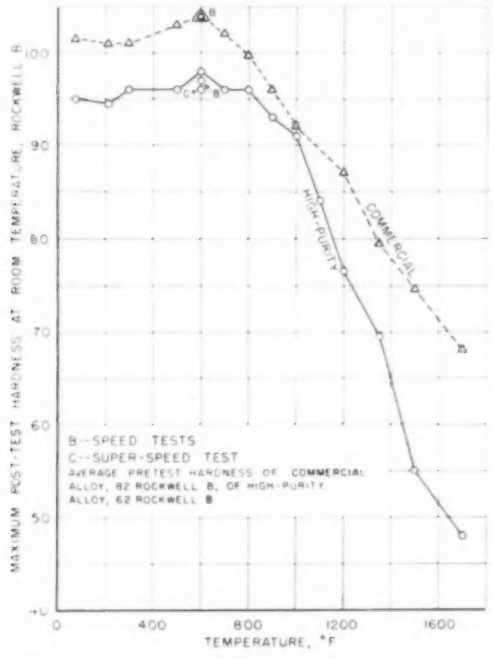
MAXIMUM POST-TEST HARDNESS AT ROOM TEMPERATURE, ROCKWELL B
TEMPERATURE, °F
HIGH-PURITY
COMMERCIAL
B--SPEED TESTS
C--SUPER-SPEED TEST
AVERAGE PRETEST HARDNESS OF COMMERCIAL ALLOY, 82 ROCKWELL B; OF HIGH-PURITY ALLOY, 62 ROCKWELL B

FIGURE 14. *Influence of test temperature and strain rate, on the maximum hardness at room temperature of specimens of the alloys fractured in tension.*

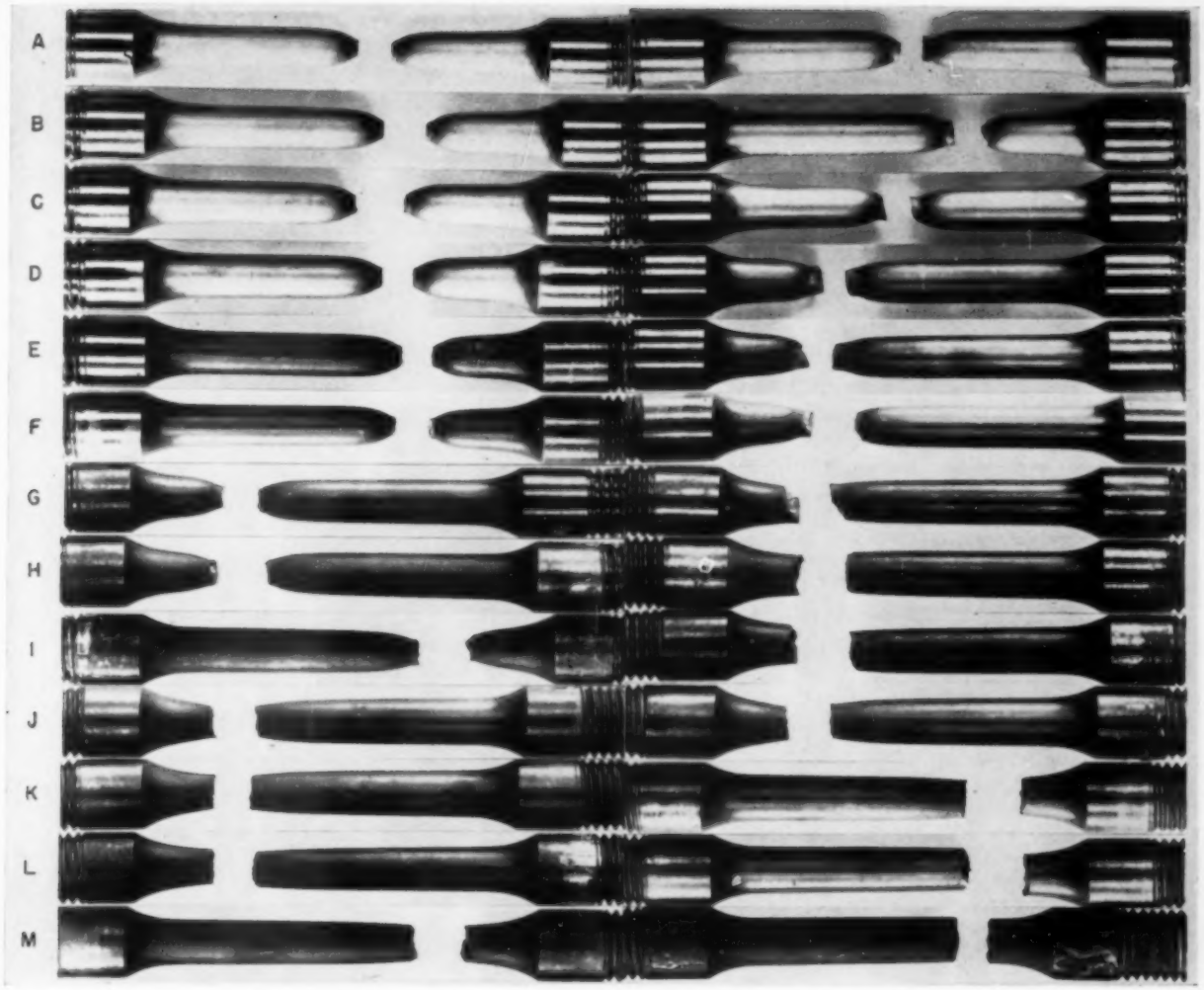

FIGURE 15. *Specimens fractured in tension at different temperatures.*

Specimens of the high-purity alloy are shown at the left and specimens of the commercial alloy at the right of the photograph. A, 75° F; B, 212° F; C, 300° F; D, 500° F; E, 600° F; F, 700° F; G, 800° F; H, 900° F; I, 1,000° F; J, 1,200° F; K, 1,350° F; L, 1,500° F; M, 1,700° F. × 1/2.

4.2. Fracture Characteristics and Microstructures

The effect of temperature on the tendency of the alloys to contract locally (neck) is illustrated by the photographs of the fractured specimens (fig. 15). At the lower range of temperature, specimens of both alloys contracted locally and fractured in a ductile manner with a relatively large rim effect (fig. 16). At the higher range of temperature, the specimens deformed more uniformly over the entire reduced section and fractured in a relatively brittle manner without a pronounced rim effect (figs. 15 and 16). However, the trend toward brittle behavior at the higher test temperatures was considerably more prominent for the commercial than for the high-purity alloy. This feature is also shown by a comparison of the curves of figure 17. It is noteworthy that the reduction-in-area—distance-from-fracture curve for the specimen of high-purity alloy tested at 1,700° F crosses all the curves for specimens of this alloy tested at lower temperatures. This fact again illustrates the complexity of the mechanisms of flow and fracture of the alloys at elevated temperatures.

The appearance of the surface and the types of fractures obtained in the alloys tested at various temperatures are shown in figure 18. No surface cracking was observed in any of the specimens of the high-purity alloy tested at temperatures up to and including 900° F (fig. 18,D); shear-type fractures and circumferential strain markings were characteristic of these specimens. Except for fewer strain markings, these characteristics were also obtained in specimens of the commercial alloy fractured at temperatures up to and including 800° F (fig. 18,A and B). Surface cracks were observed in all of the specimens fractured at the higher temperatures, and the brittleness increased with temperatures (fig. 18,D and E, C and F); the surface appearance was similar for the specimens of both alloys fractured at 1,200° F (not shown). Thus, the tendency toward brittle behavior was accentuated by the in-

creased amount of impurities and by an increase in test temperatures.

The influences of temperature on the microstructures and on internal cracking of the specimens are illustrated in figures 19 to 22, inclusive.

The initially equiaxed grains of the annealed alloys (fig. 19,A and B) were elongated in the direction of the applied stresses in the specimens fractured at temperatures below the recrystallization range (fig. 19); the extent of the elongation apparently decreased as the temperature was increased. The microcracks were confined to the region of complete fracture in the specimens of the high-purity alloy tested at temperatures up to and including 900° F (fig. 19,C and E) and in the specimens of the commercial alloy tested at temperatures up to 600° F (fig. 19,D). Appreciable microcracking, extending from the axis to the surface, occurred in the specimen of the commercial alloy fractured at 900° F (fig. 19,F and H). The formation of an oxide film (top edge of the photomicrograph of fig. 19,H) may have also contributed to the brittle behavior of this specimen.

Numerous microcracks were observed both in the region of fracture and at some distance from it in all the specimens fractured at temperatures in excess of the recrystallization temperatures (figs. 20, 21, and 22). The number of these cracks and the extent of cracking, however, varied with the temperature, composition of the alloy, and distance from the region of complete fracture. At 1,200° F, the two alloys were nearly alike with regard to cracking (fig. 20,A and B; fig. 22,A and B), and no detectable grain growth occurred.

At 1,500° F, the microcracks observed in the region of fracture were possibly somewhat less numerous but of larger size in the specimen of the high-purity alloy than in the specimen of the commercial alloy (fig. 20,C and D; fig. 21,A and B). This was true also in the region about 0.5 in. from the fracture (fig. 22,C and D.) The microcracking was confined principally to the grain boundaries, and no abnormal grain growth was detected in the recrystallized structure.

At 1,700° F, intercrystalline cracking was prominent in the vicinity of fracture and as some distance from fracture in the specimens of both alloys (fig. 20,E and F; fig. 21,C and D; fig. 22,E and F). Strain markings and twins were present in the recrystallized structures at the time of failure. Appreciable grain growth also occurred at this temperature.

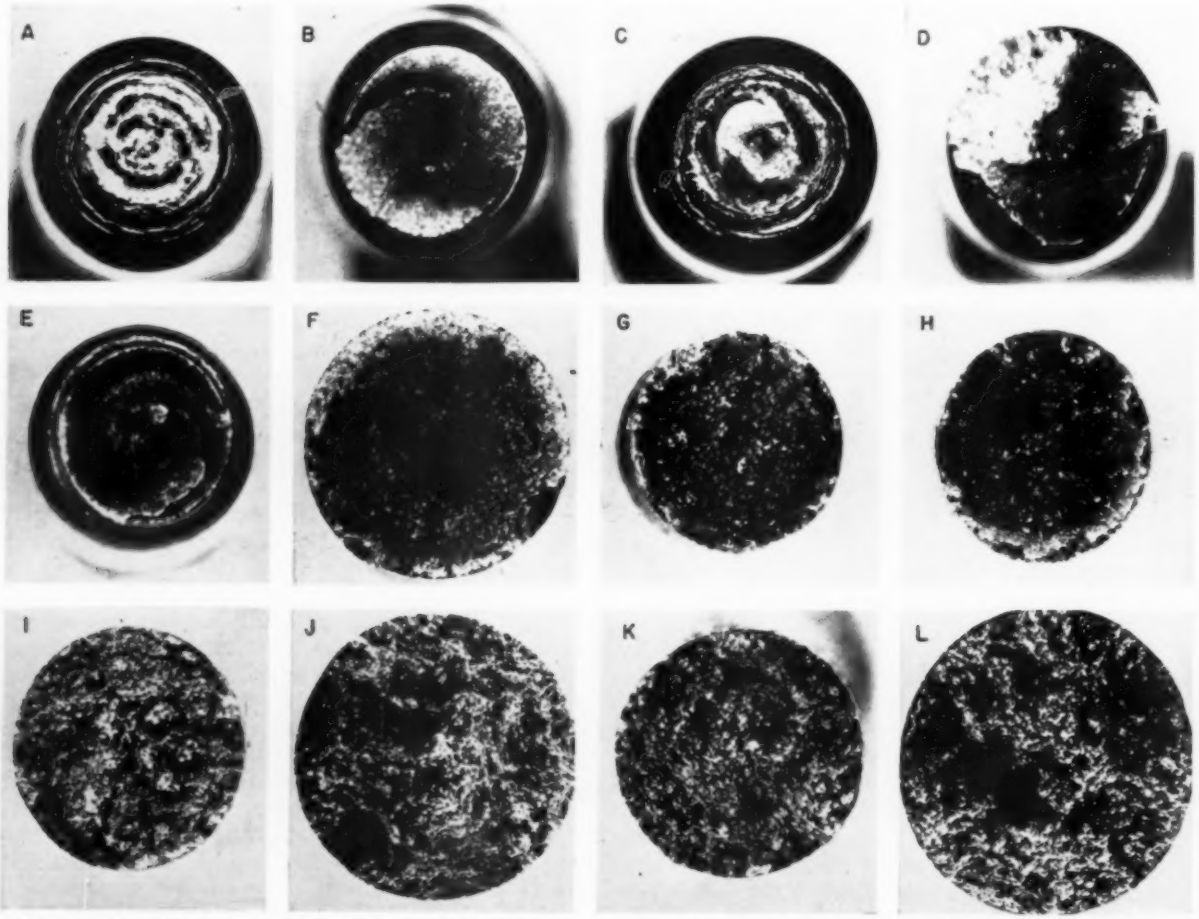

FIGURE 16. *Cross sections at fracture of specimens of the alloys fractured in tension at different temperatures.*

A, C, E, G, I, and K, Specimens of the high-purity alloy; B, D, F, H, and L, specimens of the commercial alloy. A, B, 300° F; C, D, 600° F; E, F, 900° F; G, H, 1,200° F; I, J, 1,500° F; K, L, 1,700° F. ×3.5.

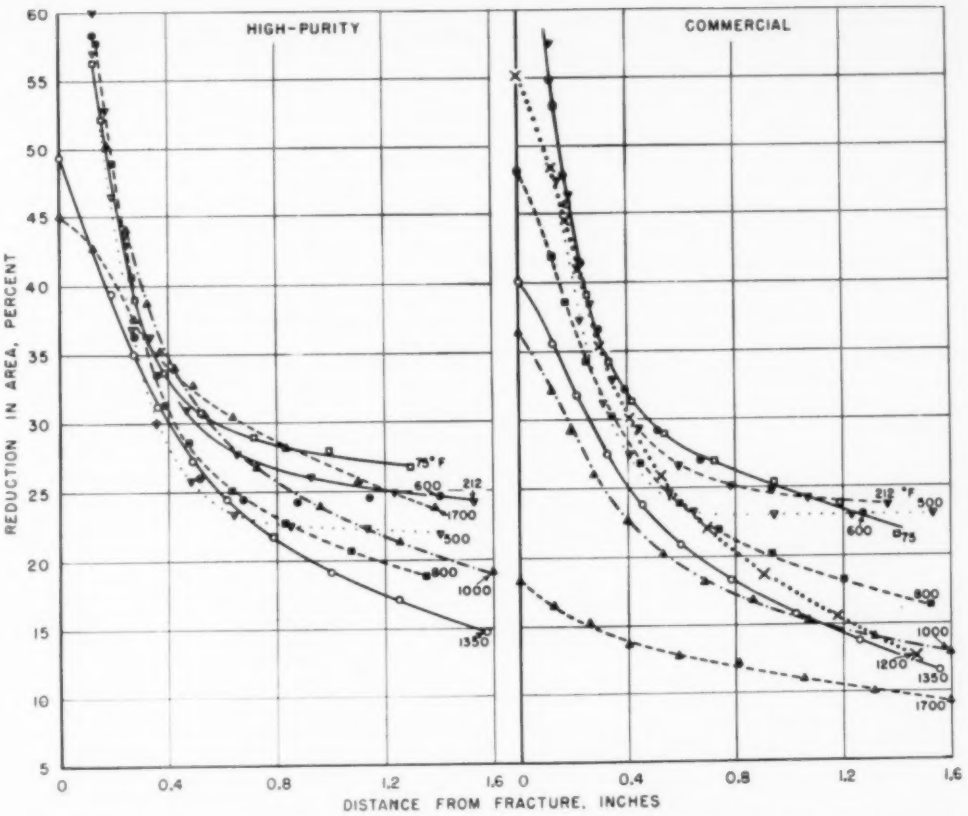

FIGURE 17. *Plastic deformation of the specimens fractured in tension at different temperatures.*

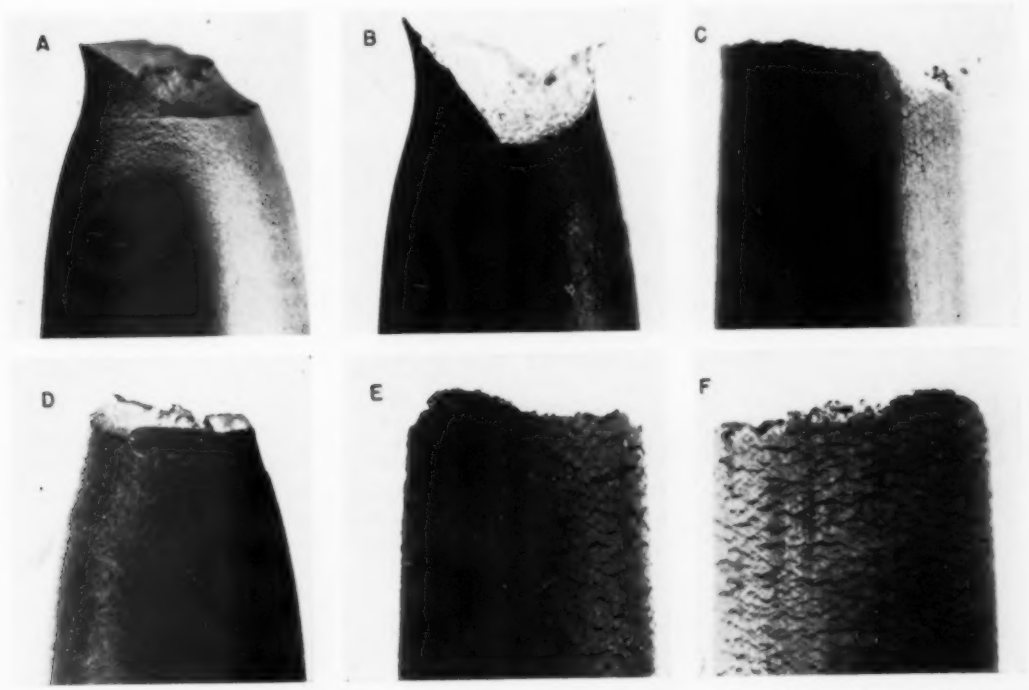

FIGURE 18. *Influence of test temperature on the appearance of the surface of the specimens at fracture.*

A, B, C, and F, specimens of the commercial alloy; D and E, specimens of the high-purity alloy. A, 300° F; B, 600° F; C, D, 900° F; E, F, 1,700° F. ×3.5.

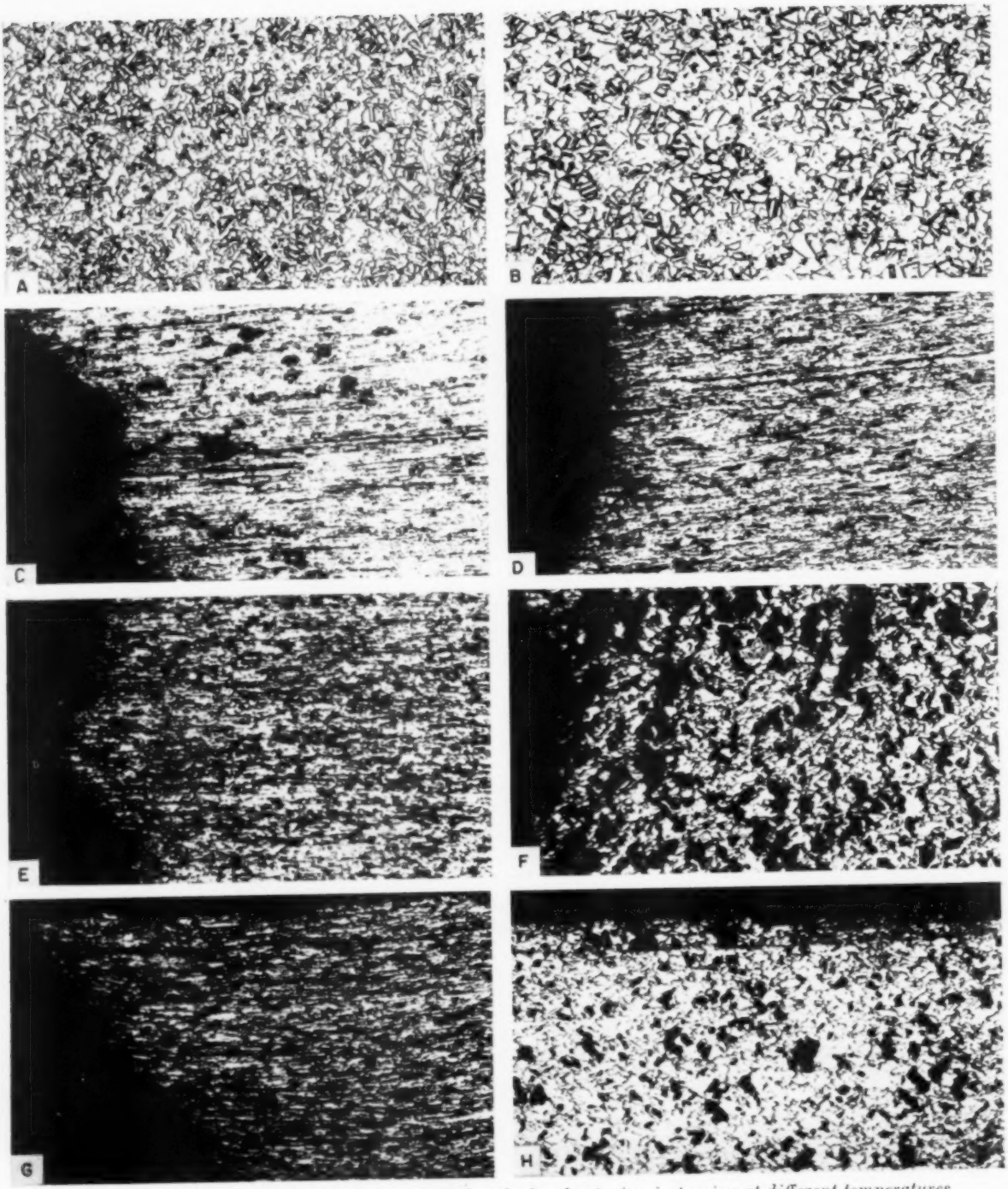

FIGURE 19. *Structure of the alloys as annealed and after fracturing in tension at different temperatures.*

Longitudinal section etched with 6 parts of nitric (concentrated) and 4 parts of glacial acetic acids. × 75.

	Alloy	Test temperature	Remarks
		°F	
A	High-purity	None	As annealed.
B	Commercial	None	Do.
C	High-purity	600	Structure near axis at fracture.
D	Commercial	600	Do.
E	High-purity	900	Do.
F	Commercial	900	Do.
G	High-purity	900	Structure near surface at fracture.
H	Commercial	900	Do.

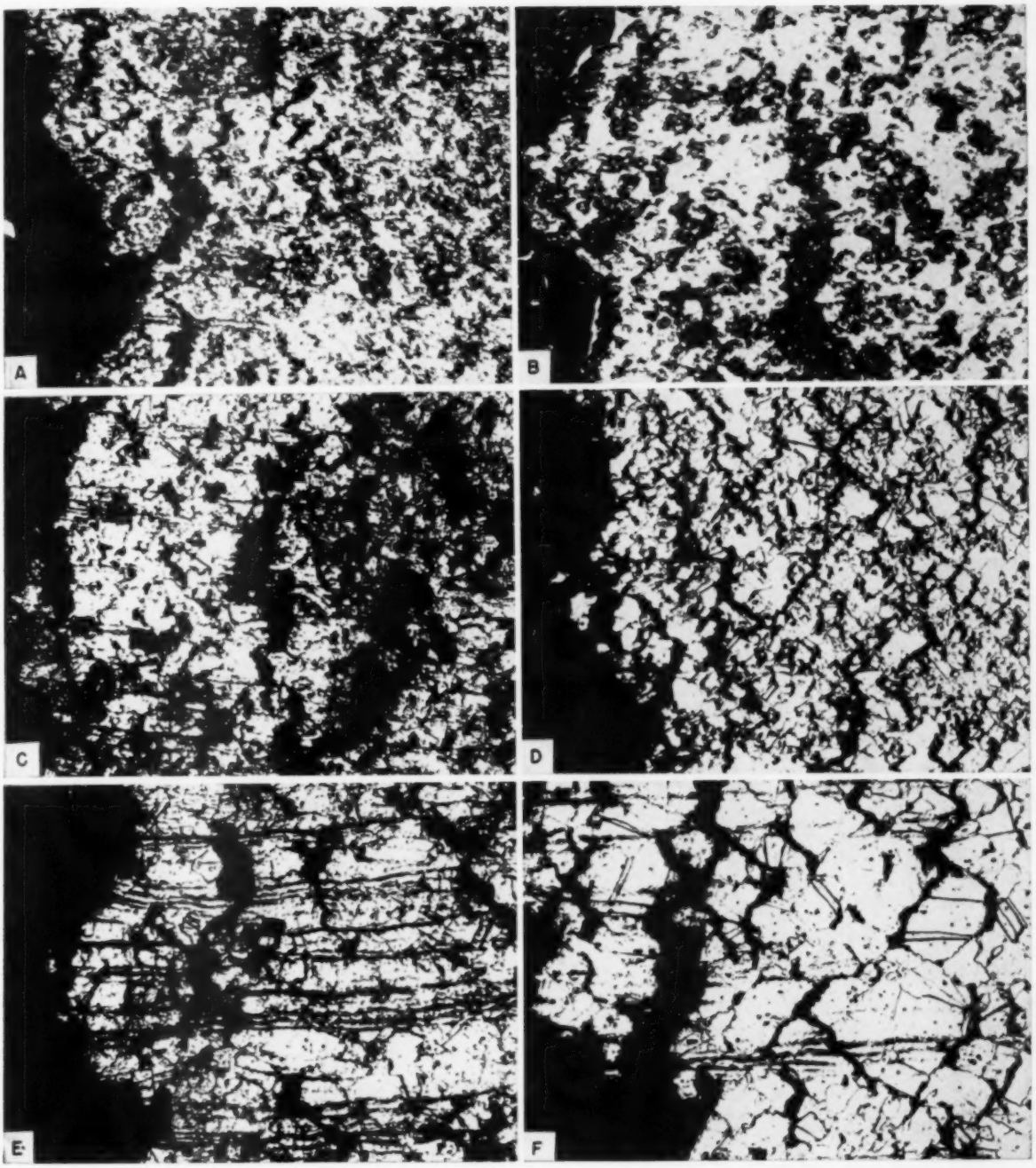

FIGURE 20. *Structure of the alloys after fracturing in tension at different temperatures above the recrystallization ranges.*

Longitudinal sections etched with 6 parts of nitric (concentrated) and 4 parts of glacial acetic acids. × 75.

	Alloy	Test temperature	Remarks
		°F	
A	High-purity	1,200	Structure near axis at fracture.
B	Commercial	1,200	Do.
C	High-purity	1,500	Do.
D	Commercial	1,500	Do.
E	High-purity	1,700	Do.
F	Commercial	1,700	Do.

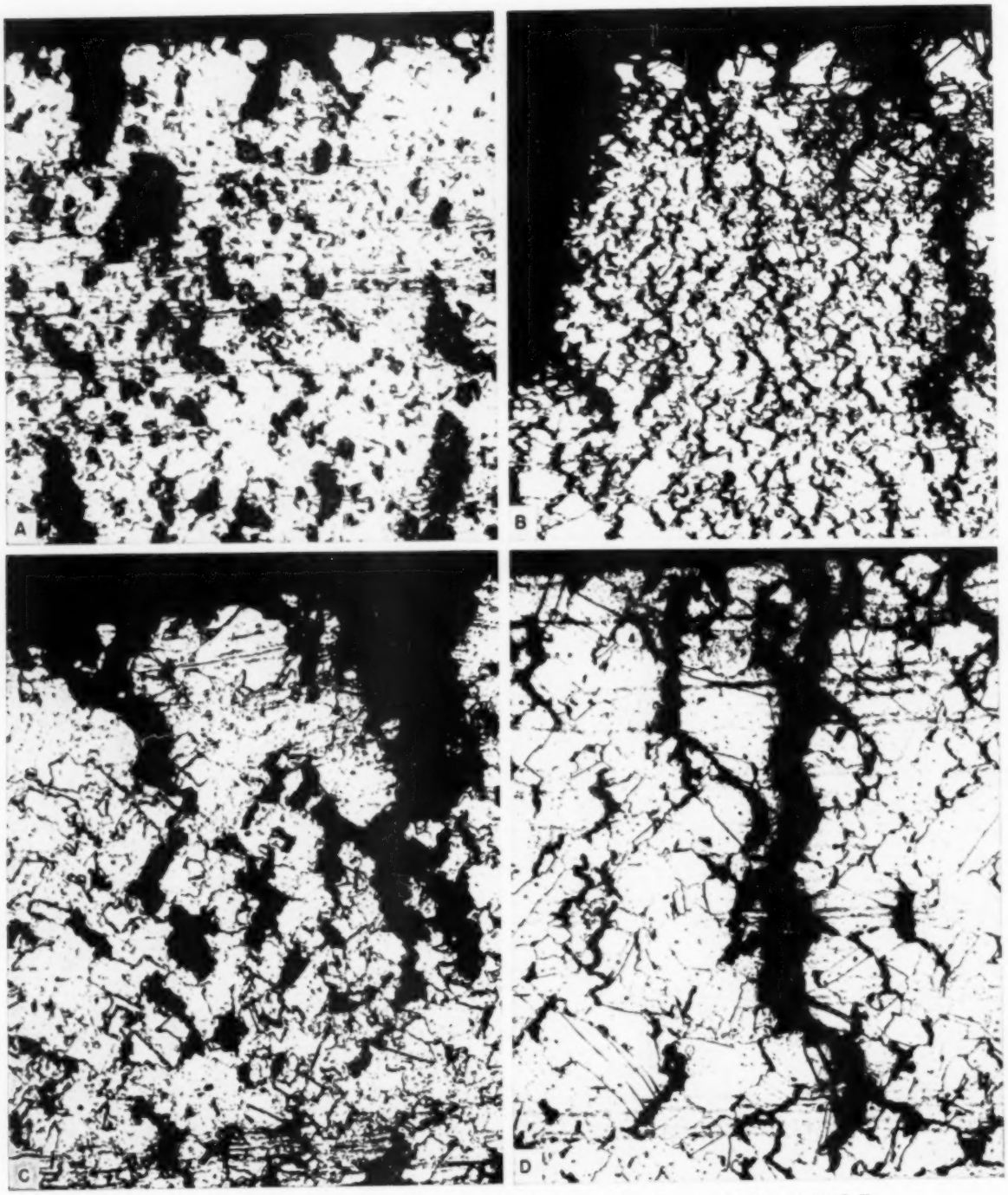

FIGURE 21. *Structure of the alloys after fracturing in tension at 1,500° or 1,700° F.*

Longitu linal sections etched with 6 parts of nitric (concentrated) and 4 parts of glacial acetic acids. × 75.

	Alloy	Test temperature	Remarks
		° F	
A	High-purity	1,500	Structure at surface near fracture.
B	Commercial	1,500	Do.
C	High-purity	1,700	Do.
D	Commercial	1,700	Do.

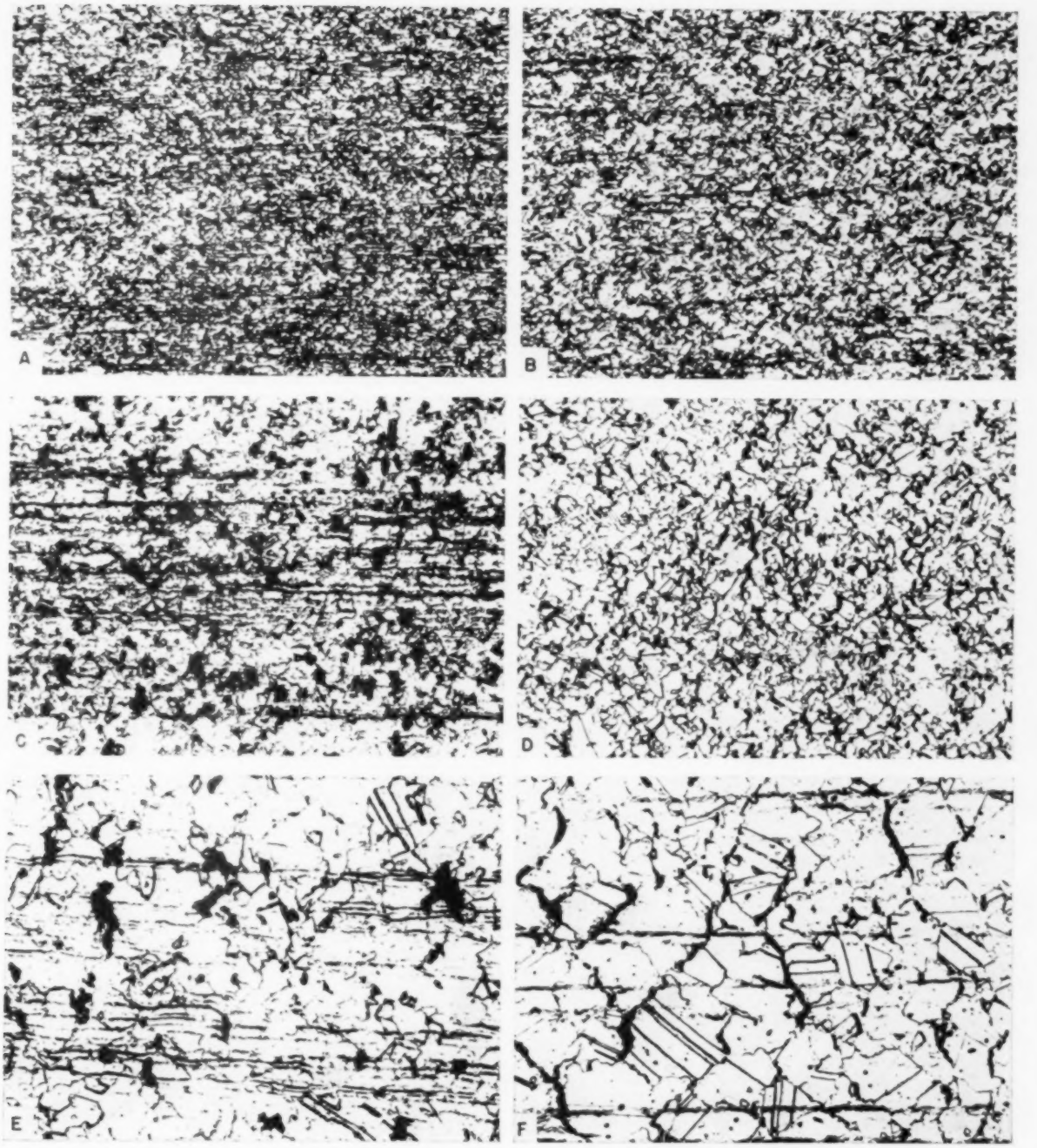

FIGURE 22. *Structure of the alloys after fracturing in tension at different temperatures above the recrystallization ranges.*

Longitudinal sections etched with 6 parts of nitric (concentrated) and 4 parts of glacial acetic acids. × 75.

	Alloy	Test temperature	Remarks
		°F	
A	High-purity	1,200	Structure at axis approximately ½ in. from fracture.
B	Commercial	1,200	Do.
C	High-purity	1,500	Do.
D	Commercial	1,500	Do.
E	High-purity	1,700	Do.
F	Commercial	1,700	Do.

5. Summary

Tensile tests were made at temperatures ranging from 75° to 1,700° F on specimens of both high-purity and commercial 70-percent-nickel–30-percent-copper alloys, each with the same initial grain size and structure.

Serrated stress-strain curves were obtained on specimens tested at temperatures ranging from 300° to 900° F. These serrations were more noticeable for the high-purity alloy than for the commercial alloy. Discontinuous flow also occurred in specimens of both alloys tested at temperatures above 900° F. The serrations were interpreted as being associated with strain-aging and other atomic rearrangements, and the discontinuous flow at the higher temperatures as being associated with recrystallization and grain growth. Strain-aging was also manifested in the strength-temperature relationships of both alloys; it was especially prominent in the curves for tensile and fracture strengths. Variations in composition of the two alloys markedly affected its strength properties (yield, tensile, and fracture) and reduction of area at temperatures below 1,100° F. Above 1,200° F, the strength properties for the two alloys were quite similar, but the values obtained for ductility (reduction of area, strain at maximum load, and elongation) were influenced by the composition of the alloys; at 1,200° F, the ductilities of both alloys were nearly the same.

The rates of work-hardening varied with the test temperature, amount of strain, and composition of the alloys.

The results of hardness tests made at room temperature on specimens of both alloys fractured in tension at different temperatures indicated the predominance of strain-aging and work-hardening at the low range in temperature, a balance of work-hardening and recovery in the intermediate range, and the predominance of recrystallization and recovery at the higher temperatures used in the tensile tests. The hardness at room temperature of the fractured specimens was also dependent upon the composition of the alloy and the amount of plastic deformation.

At temperatures below 900° F, the specimens of both alloys contracted locally before fracturing in a ductile manner with a rim. At temperatures above 900° F, specimens of both alloys deformed more uniformly before fracturing in a relatively brittle manner without a pronounced rim. The necking and fracture characteristics were also affected by the composition of the alloys.

The final structures and the microcracks produced in the specimens fractured at different temperatures varied with the test temperature, amount of plastic deformation, and composition of the alloys.

6. References

[1] G. W. Geil and N. L. Carwile, Tensile properties of copper, nickel, and some copper-nickel alloys at low temperatures, NBS Circular 520, p. 67 (1952).
[2] Nickel and nickel alloys, p. 5 (The International Nickel Co., Inc., Sec. J, 1941).
[3] Nickel and its alloys, NBS Circular 485 (1950).
[4] P. G. McVetty and N. L. Mochel, Tensile properties of stainless iron and other alloys at elevated temperatures, Trans. Am. Soc. Steel Treating **11,** 73 (1927).
[5] J. A. Bennett and D. J. McAdam, Jr. Creep rates of cold-drawn nickel-copper alloy (Monel metal), J. Research NBS **28,** 417 (1942) RP1462.
[6] D. J. McAdam, Jr., G. W. Geil, and D. H. Woodard, Influence of strain rate and temperature on the mechanical properties of Monel metal and copper, Proc. Am. Soc. Testing Materials **46,** 902 (1946).
[7] N. J. Grant and A. G. Bucklin, Creep-rupture and recrystallization of Monel from 700° to 1,700° F, Trans. Am. Soc. Metals **45,** 151 (1953).
[8] P. Shahinian and J. R. Lane, Influence of grain size on high temperature properties of Monel, Trans. Am. Soc. Metals **45,** 177 (1953).
[9] B. B. Betty, H. L. Eiselstein, and F. P. Huston, Creep properties of cold-drawn annealed Monel and Inconel, Trans. Am. Inst. Mining Met. Engrs. **161,** 441 (1945).
[10] W. D. Jenkins and T. G. Digges, Effect of temperature on the tensile properties of high-purity nickel, J. Research NBS **48,** 313 (1952) RP2317.

Washington, August 4, 1954.

Journal of Research of the National Bureau of Standards Vol. 54, No. 1, January 1955 Research Paper 2562

The System Lime-Water at 21° C and High Pressures

Charles E. Weir

Compression measurements on the binary system $Ca(OH)_2$-H_2O at 21° C and high pressures show a large discontinuity in volume at 2,800 atmospheres which involves both components. Evidence is presented that the transition is the result of formation of a hydrate of lime, $Ca(OH)_2 \cdot n\ H_2O$, where $4 \leq n \leq 6$. A pressure composition diagram for the system $Ca(OH)_2$-H_2O at 21° C is given.

1. Introduction

In a recent study of the properties of portland cements subjected to high hydrostatic pressure, a large volume discontinuity was noted in systems containing cement and free water [1].[1] By elimination procedures it was finally concluded that the volume discontinuity arose from the system $Ca(OH)_2$-H_2O. The present report describes the results of direct studies on the system $Ca(OH)_2$-H_2O at 21° C and high pressures.

The literature on hydrate formation in alkaline earth hydroxides is extensive and will not be reviewed here. It is sufficient to note that although numerous reports have been made of hydrates of $Ca(OH)_2$ at room temperature, none appear to be accepted as reliable [2] and no hydrate of $Ca(OH)_2$ is believed to exist. As a result of the present studies it is concluded that a hydrate of $Ca(OH)_2$ is stable at pressures above 3,000 atm at 21° C, and a rough pressure-composition diagram is proposed.

2. Experimental Method

Techniques and apparatus used here for studies of compression at high pressures have been described in detail [3]. Briefly, an experiment consists in forcing a leakproof piston into the bore of a heavy-walled pressure vessel that contains the specimen immersed in a light petroleum distillate (Varsol). Measurements are made of the depth of penetration of the piston at each 1,000 atm, the pressure being determined by means of a calibrated manganin pressure gage immersed in the Varsol inside the pressure vessel. Another experiment performed with a steel bar of comparable volume replacing the specimen permits calculation of the compression of the specimen in terms of that of steel, which is known.

The specimens used in these studies were mixtures of powdered $Ca(OH)_2$ and distilled water contained in a cylindrical steel tube open to the confining liquid at one end. $Ca(OH)_2$ was of chemical reagent grade and was weighed out in the tube. Freshly distilled water was also weighed into the tube, so that the weights of both components were known. Each water-$Ca(OH)_2$ mixture was stirred thoroughly to obtain a uniform mixture and then stirred with Varsol prior to compression. The dry $Ca(OH)_2$ was treated in a similar manner except that no water was added. Following compression of this specimen, the volume was determined by hydrostatic weighing in Varsol. The resulting calculated density for the $Ca(OH)_2$ was used to calculate the volumes of $Ca(OH)_2$ in all experiments in which water-$Ca(OH)_2$ mixtures were used. The volume of the water was calculated from known data for the density of water. The amount of $Ca(OH)_2$ dissolved was neglected in this calculation.

3. Results and Discussion

The results of compression measurements on the various mixtures are given in table 1. The mole fraction of $Ca(OH)_2$ in each mixture is tabulated at the head of each corresponding column of compression data. The compressions are expressed in terms of $-\Delta V/V_0$, where $-\Delta V$ is reckoned from the arbitrary zero at 2,000 atm, and V_0 is the volume of the specimen at 1 atm. Values of compression at pressures below 2,000 atm, therefore, appear as negative. The lowest pressure attained in these studies was 1,143 atm rather than 1,000 atm, and an additional measurement was made at 2,470 atm in most experiments, as shown in table 1. At the higher water contents it was not possible to attain the maximum pressure of 10,000 atm because of the excessive piston travel arising from the large transitions. In these experiments the initial readings were made at 9,000 atm. In experiments with 0.12 and 0.022 mole fractions of $Ca(OH)_2$ attempts were made to attain 10,000 atm, but the immediate crystallization of ice-VI, initiated at a pressure of about 9,300 atm, produced too large a piston travel. In the measurement with 0.080 mole fraction of $Ca(OH)_2$ the maximum pressure was only 9,100 atm and no ice-VI crystallized, but the measurement at 9,000 atm undoubtedly represents data for a metastable system.

The rather complex behavior of the tabular data is simplified by considering the compression-pressure curves shown in figures 1 and 2. Figure 1 contains the data for dry $Ca(OH)_2$ and the mixtures of high $Ca(OH)_2$ content, and corresponding data for water and the mixtures of low $Ca(OH)_2$ content

[1] Figures in brackets indicate the literature references at the end of this paper.

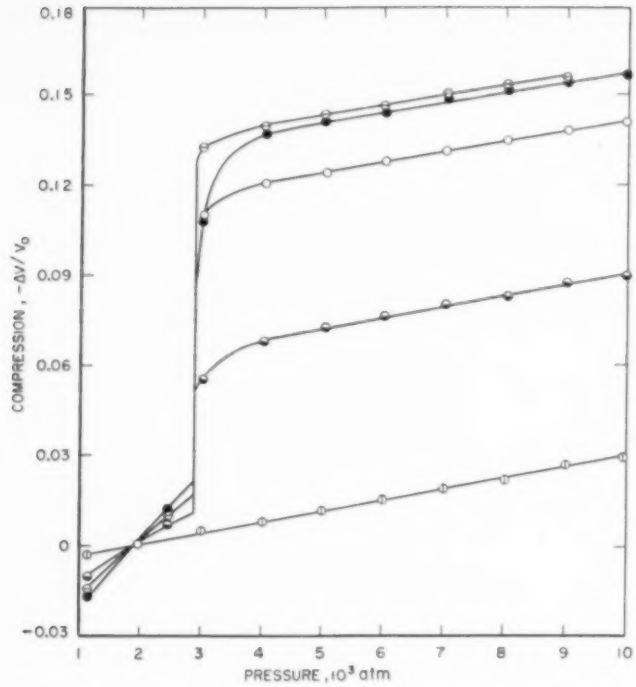

FIGURE 1. *Compression of mixtures of* $Ca(OH)_2$ *and* H_2O *rich in* $Ca(OH)_2$.

①, 100 mole percent $Ca(OH)_2$; ◒, 56 mole percent $Ca(OH)_2$; ○, 31 mole percent $Ca(OH)_2$; ●, 26 mole percent $Ca(OH)_2$; ⊖, 20 mole percent $Ca(OH)_2$.

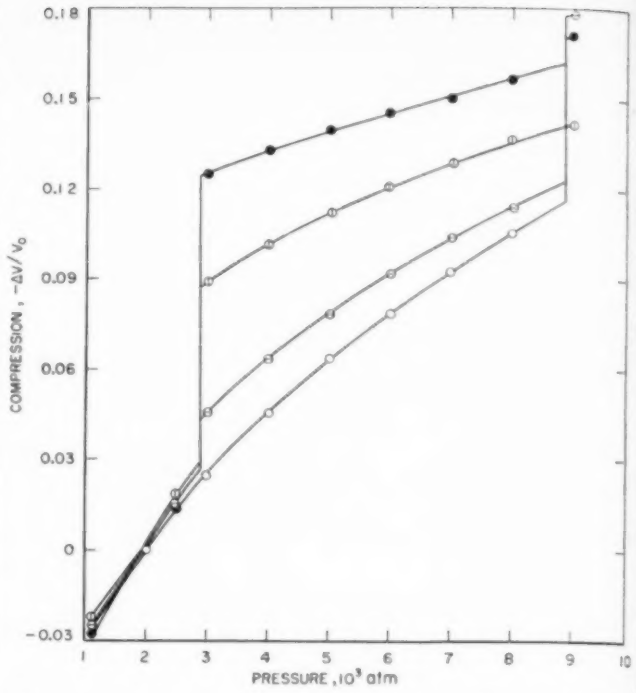

FIGURE 2. *Compression of mixtures of* $Ca(OH)_2$ *and* H_2O *rich in* H_2O.

●, 12 mole percent $Ca(OH)_2$; ①, 8 mole percent $Ca(OH)_2$; ⊖, 2.2 mole percent $Ca(OH)_2$; ○, 0 mole percent $Ca(OH)_2$.

TABLE 1. *Compression of* $Ca(OH)_2$-H_2O *mixtures at 21° C*

$-\Delta V/V_0$

Pressure	Mole fraction of $Ca(OH)_2$ in mixture							
	1	0.56	0.31	0.26	0.20	0.12	0.080	0.022
atm								
10,000	0.0296	0.0896	0.1411	0.1577	.....	.....	.....	.....
9,000	.0266	.0869	.1385	.1547	0.1559	0.1708	0.1418	0.1778
8,000	.0217	.0830	.1350	.1517	.1528	.1564	.1362	.1139
7,000	.0189	.0799	.1314	.1483	.1502	.1500	.1287	.1035
6,000	.0150	.0762	.1281	.1440	.1467	.1451	.1207	.0917
5,000	.0113	.0723	.1245	.1411	.1433	.1394	.1120	.0786
4,000	.0073	.0678	.1206	.1366	.1390	.1328	.1018	.0633
3,000	.0048	.0554	.1097	.1080	.1323	.1248	.0891	.0459
2,470	.....	.0070	.0115	.....	.0111	.0144	.0175	.0155
2,000	.0000	.0000	.0000	.0000	.0000	.0000	.0000	.0000
1,143	−.0037	−.0106	−.0149	−.0173	−.0174	−.0285	−.0218	−.0227

are given in figure 2. The data for liquid water were reported by Adams [4].

The following observations may be made from the curves of figures 1 and 2:

(1). The large discontinuity in volume in the system $Ca(OH)_2$-H_2O involves both components because no comparable effect occurs in water or dry $Ca(OH)_2$ alone.

(2). Quantitatively, the amount of the discontinuity reaches a maximum for some intermediate composition of the mixture.

(3). No evidence exists for formation of ice-VI at low water contents, but at high water contents, ice-VI separates at approximately 8,800 atm in an amount that increases with increasing water content.

(4). It may be concluded, therefore, that no liquid water is present at pressures above 3,000 atm in mixtures richer in $Ca(OH)_2$ than approximately 20 mole percent. This conclusion follows in part from observations (3) above and in part from the very low compressibilities (slopes of the $-\Delta V/V_0$ versus P curves) noted above 3,000 atm, which are characteristic of solid phases.

(5). In the presence of excess water, the discontinuity in volume at 2,800 atm is relatively sharp, but excess $Ca(OH)_2$ appears to "spread out" the discontinuity over a wider pressure range. Solid $Ca(OH)_2$, therefore, appears to act as an impurity

and produces rounding of the corners of the discontinuity. As the phases present above 3,000 atm are believed to be all solids in mixtures rich in $Ca(OH)_2$, contamination may be interpreted in terms of solid solutions.

(6). The compressibilities of the products formed above 2,800 atm in mixtures rich in $Ca(OH)_2$ seem to be slightly less than the compressibility of the parent dry $Ca(OH)_2$ (see table 2). It must be noted, however, that in this region two components are most probably present.

(7). The freezing pressure of water in mixtures rich in water is definitely below 9,000 atm. Inasmuch as pure water freezes under these conditions at approximately 8,800 atm [5], the material formed by the transition at 2,800 atm can be only sparingly soluble.

(8). The presence of excess water is clearly shown by the curvature noted above 3,000 atm in the curves of figure 2 and by the increasing resemblance of these curves to that for pure water as the water content increases. The strong dissimilarity between these curves above 3,000 atm and those of figure 1 is to be noted.

(9). The sharp drop in compressibility noticed on formation of the high-pressure phase in both figures 1 and 2 may be taken to indicate disappearance of water coincident with formation of the high-pressure phase.

TABLE 2. *Volume discontinuity and compressibility data*

Mole fraction of $Ca(OH)_2$	Discontinuity in volume $(-\Delta V/V_0)$ at 2,800 atm	Compressibility of high-pressure phase
	cm³/cm³	*atm⁻¹*
1	0	3.7×10^{-6}
0.56	0.0530	3.4
.31	.1012	3.3
.26	.1155	3.3
.197	.1172	3.3
.120	.0885	.....
.080	.0693	.....
.022	.0182	.....
0	0	.....

The compressibilities and discontinuities of volume referred to above are tabulated in table 2. These data were all obtained graphically and for this reason are not to be considered as precise. In addition, the evaluation of the discontinuity in volume is subject to obvious extrapolation errors incurred in extrapolating to 2,800 atm. The large curvature existing in the presence of excess water prevented graphical estimation of compressibilities for mixtures rich in H_2O.

As a result of the foregoing observations the reaction,

$$Ca(OH)_2 + n\ H_2O \rightleftarrows Ca(OH)_2 \cdot n\ H_2O, \qquad (1)$$

where n is an unspecified but fixed number, is believed to occur reversibly in the system $Ca(OH)_2$-H_2O at approximately 2,800 atm. The product of compression is written as a molecule containing water of hydration merely for convenience as it is recognized that this material may be a form containing a complex aquo-cation [6]. As evidence against the former type of compound, it might be anticipated that a material containing ordinary water of crystallization would be less dense and probably more compressible than the parent anhydrous material. The possibility that the volume discontinuity arises from transformation of amorphous $Ca(OH)_2$ to the more dense crystalline $Ca(OH)_2$ is discounted because liquid water would not disappear in such a process and reversibility would not be expected.

The value of n in eq (1) may be bounded in the following manner: In these mixtures the quantity of product formed will be proportional to the quantity of the component present in deficiency. That is, in the presence of excess $Ca(OH)_2$ the amount of reaction 1 will be determined by the quantity of water present, whereas in the presence of excess water the $Ca(OH)_2$ becomes the determining factor. If the discontinuity in volume is taken to be a measure of the extent of reaction 1, a plot of mole fraction versus volume change at discontinuity should produce two lines intersecting at the composition corresponding to the pure compound. Such a graph of the data of table 2 is shown in figure 3. In figure 3, it is noted that in the region of excess H_2O good linearity is obtained but in the region of excess $Ca(OH)_2$ curvature appears to exist. This may arise from interaction between the components in the presence of excess $Ca(OH)_2$, as mentioned in observation (5). As a result of this curvature and the large slope of the linear section, it is not possible to place narrow limits on n. From figure 3 it would appear that it can be stated with assurance that $3 \leq n \leq 7$ and with considerable less certainty that $4 \leq n \leq 6$.

From the foregoing considerations, a rough phase diagram for the system $Ca(OH)_2$-H_2O at 21° can be constructed. This diagram is given in figure 4, and is based on the previous discussion. In the solution region, however, no measurements have been made, as it was believed that no conclusions could be

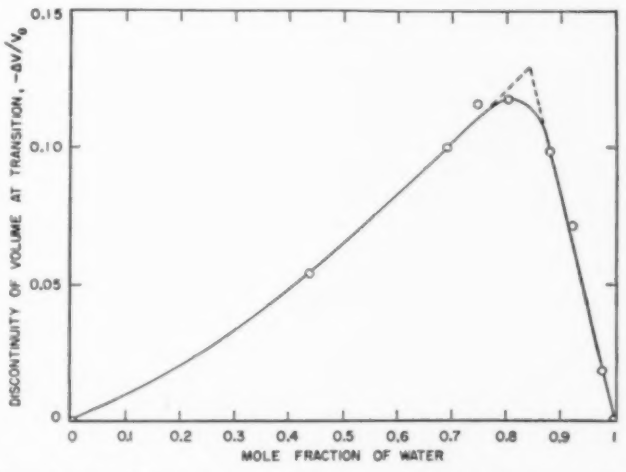

FIGURE 3. *Effect of composition on discontinuity of volume at transition.*

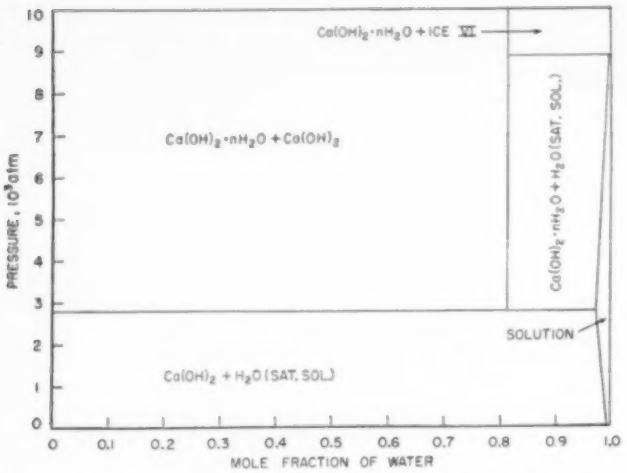

FIGURE 4. *Proposed pressure-composition diagram for system* $Ca(OH)_2$-H_2O *at 21° C.*

formed because of the slight solubility of $Ca(OH)_2$. In this region, therefore, the course of the curve has been estimated. The initially increasing solubility of $Ca(OH)_2$ with increasing pressure is inferred from the fact that its solubility increases with decreasing temperature [7]. Either this solubility decreases as is indicated at higher pressures or dissolved $Ca(OH)_2$ is transformed into the compound of eq (1), which is sparingly soluble, since the saturated solution freezes at approximately the same pressure as pure H_2O. In the latter case, the transition line at 2,800 atm would extend across the solution region. Above 3,000 atm, the solid phase may be a mixture involving a solid solution. In the light of the present knowledge, satisfactory representation of any solid solution field is of dubious value. No attempt to include such a field on the diagram was made.

It must be emphasized that the data given here were obtained on decreasing the pressure, and figure 4 represents these findings. On increasing pressure, the low-pressure forms may persist at considerably higher pressures than those indicated in figure 4 for the transition lines. This feature is quite common in most high-pressure transitions.

The results reported here may be of significance geologically because hydrolyzable calcium salts in minerals subjected to pressures above 3,000 atm may tend to exist in the form of the high-pressure hydrate. This transition was originally observed in wet hydrated cement paste and in wet hydrated tricalcium silicate, both of which contain $Ca(OH)_2$. However, it does not occur in gypsum-water mixtures at pressures as high as 10,000 atm. In view of the anomalous solubility behavior of calcium compounds and the large decrease in volume at the transition, however, there appears a distinct possibility of the occurrence of such processes at still higher pressures in the earth.

4. References

[1] C. E. Weir and C. M. Hunt (in preparation).
[2] N. V. Sidgwick, The chemical elements and their compounds, vol. 1, p. 248 (Clarendon Press, Oxford, 1950).
[3] C. E. Weir, J. Research NBS **45,** 468 (1950) RP2160.
[4] L. H. Adams, J. Am. Chem. Soc. **53,** 3769 (1931).
[5] International Critical Tables, vol. IV (McGraw-Hill Book Co., Inc., New York, N. Y., 1928).
[6] H. J. Emeleus and J. S. Anderson, Modern aspects of inorganic chemistry, p. 191 (D. Van Nostrand Co., Inc., New York, N. Y., 1952).
[7] B. Peppler and L. S. Wells, J. Research NBS **52,** 75 (1954) RP2476.

WASHINGTON, September 15, 1954.

Journal of Research of the National Bureau of Standards Vol. 54, No. 1, January 1955 Research Paper 2563

Absorption of Radiant Energy by Solid Particles in Suspension

James E. Stewart

A simple theory is developed to describe the absorption of radiant energy by particles suspended in a transparent medium and also by an absorbing medium containing transparent suspended particles. It is found that in both cases transmittance increases as particle size increases. Apparent deviations from Beer's law and other effects that might introduce difficulties in experimental work are discussed.

1. Introduction

Radiation-absorption measurements have long been used for quantitative analysis of materials in the gas and liquid phases. Solid materials, however, have been troublesome even for qualitative determinations because of the inherent difficulties in preparing specimens in a reproducible form. Until recently the standard method for study of solids has been to suspend finely divided particles in a medium such as mineral oil in order to reduce the amount of energy lost by scattering. In principle, the concentration of such a mixture, or mull, can be controlled by careful weighing, and the thickness of the mixture can be kept fixed by proper cell design [1].[1] But the method is inconvenient, and its usefulness suffers from interference by absorption bands of the suspension medium.

Recently a new technique [2, 3] has been proposed in which finely ground particles of a solid sample are mixed with an alkali halide powder, usually potassium bromide, placed in a die, and pressed until a sintered disk is formed. At the Bureau, small disks, 9.5 mm in diameter and approximately 100 mg in weight, are produced in a simple die patterned after one described by Anderson [4]. Pressure is applied with an ordinary shop vise. No special precautions are taken for drying the potassium bromide or evacuating the system while pressing. Satisfactory qualitative infrared spectra have been obtained with these pellets, and the method seems promising for quantitative measurements as well.

The purpose of this report is to present a simple theoretical derivation of an absorption law for these disks and to infer from the law certain precautions to be taken when preparing samples for quantitative measurements. The discussion applies equally well to powders suspended in liquid media. Mathematical descriptions of radiation scattered from spherical particles have long been known. But they are quite complicated and cannot be approximated satisfactorily when the particles are about equal in size to the wavelength of incident radiation. In addition, index of refraction curves in the neighborhood and interior of infrared absorption bands are not known for many covalent compounds. A few published dispersion curves [5, 6] show that over many infrared absorption bands refractive index changes very little. Price and Tetlow [7] have made the same observation from their work on Christiansen windows in infrared spectra. Accordingly, the present study is concerned with the case of no interface refraction, requiring that a perfect index of refraction match between particle and surrounding medium be assumed. In reality this condition can be only approximately true at best.

[1] Figures in brackets indicate the literature references at the end of this paper.

2. Derivation of an Absorption Law

Consider first a single particle of material with absorption coefficient a defined by Beer's law, $I/I_0=\exp(-ax)$ for a uniform layer of thickness x (see fig. 1). $d\sigma_1$ is an increment of the area s_1 on which the incident plane wave falls with irradiance [2] I_0, n is a unit vector normal to the particle surface, j is a unit vector perpendicular to the radiation wave front such that the wave travels in the $-j$ direction, and dE is the energy leaving the particle through $d\sigma_2$. Beer's law can be written for a cylindrical increment of volume

$$dE=I_0 n\cdot j d\sigma_1 \exp(y_2-y_1)a. \quad (1)$$

[2] Radiant flux per unit surface area.

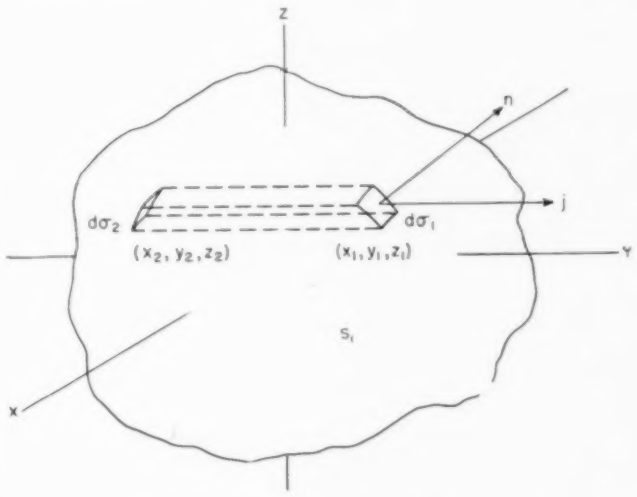

FIGURE 1. *Particle in radiant-energy field, the energy being propagated in the $-j$ direction.*

The projected cross-sectional area of the particle on the plane of the wave front is

$$A=\int_{s_1} n\cdot j d\sigma_1.$$

The average transmittance of a single particle is then

$$(I/I_0)_p=\frac{1}{AI_0}\int_{s_1} dE. \tag{2}$$

For spherical particles of radius r the integrations in (2) are easily done to give the equivalent expressions

$$\begin{aligned}(I/I_0)_{\text{sphere}}&=[1-(2ar+1)\exp(-2ar)]/2a^2r^2\\&=[\exp(2ar)-2ar-1]\exp(-2ar)/2a^2r^2\\&=2\sum_{n=0}^{\infty}\frac{(2ar)^n}{(n+2)!}\exp(-2ar)\\&=f(r,a)\exp(-2ar).\end{aligned} \tag{3}$$

Jones [8] has investigated the effect produced in the apparent absorption coefficient by holes in a layer of absorbing substance. The next step in the present development follows his method. Consider a disk containing masses m_p and m_k of sample and supporting medium of densities ρ_p and ρ_k, respectively. The sample particles are assumed to be spheres of radius r, and to be distributed uniformly throughout the unpressed disk on a cubic lattice of constant λ. The distance between layers of particles parallel to the wave front will be reduced by the pressing. It will be evident from what follows that the distribution of particles within layers can be random so long as the number of particles per layer is constant. In fact, randomness within layers will improve the validity of an approximation which will be made. The volume of disk occupied by sample and by the suspending substance is $v_p=m_p/\rho_p$ and $v_k=m_k/\rho_k$, respectively. The number of particles in the disk is

$$n_p=v_p/\tfrac{4}{3}\pi r^3=3m_p/4\pi r^3\rho_p,$$

and the mean distance between particle centers is $\lambda=[(v_k+v_p)/n_p]^{\frac{1}{3}}$. Consider first one layer of particles in cells of side λ. The ratio of the cross-sectional area, σ_p, of the sample particle contained in a single cubic unit to the cross-sectional area, σ_c, of the lattice unit is

$$\frac{\sigma_p}{\sigma_c}=\frac{\pi r^2}{\lambda^2}=\left[\frac{3\sqrt{\pi}m_p\rho_k}{4(m_k\rho_p+m_p\rho)_k}\right]^{2/3}, \tag{4}$$

and the transmittance for one layer is given by

$$(I/I_0)_1=\left(1-\frac{\sigma_p}{\sigma_c}\right)+\frac{\sigma_p}{\sigma_c}f(r,a)\exp(-2ar). \tag{5}$$

Now the number of layers in the disk is $N=\sigma_c n_p/S$, where S is the disk cross-sectional area. Substituting from above,

$$N=\frac{1}{rS}\left[\frac{3m_p}{4\pi\rho_p}\left(\frac{m_k}{\rho_k}+\frac{m_p}{\rho_p}\right)^2\right]^{1/3}. \tag{6}$$

Equation (5) gives the average transmittance of one layer of particles. We assume that the I given by (5) for one layer is the I_0 for the next layer. The irradiance after the radiation has traversed N layers is therefore

$$I/I_0=\left[\left(1-\frac{\sigma_p}{\sigma_c}\right)+\frac{\sigma_p}{\sigma_c}f(r,a)\exp(-2ar)\right]^N. \tag{7}$$

After the work reported here was completed, a similar discussion appeared in the literature [9], containing an expression for the transmittance of a potassium bromide pellet in the form $I/I_0=\epsilon^{-a(1-F)}$, in which F is the average transmittance of a single particle and a contains mass, density, and dimension parameters. A comparison of this expression expanded in a Maclaurin's series with eq (7) expanded in a binomial series demonstrates the equivalence of the equations, at least for small particles.

Now let us turn to a similar problem in which the particles are transparent and the suspension medium absorbs energy. A situation such as this is encountered in conventional mulling techniques of sample preparation but will not arise for pellets unless it becomes necessary to use suspension powders that have absorption bands. Let α be the absorption coefficient of the suspension medium and all other parameters remain as defined previously. Proceeding as above, the average transmittance for a single lattice unit is

$$\begin{aligned}(I/I_0)_c&=\frac{1}{\lambda^2}\left\{\int_{S_1}\int \epsilon^{-\alpha(\lambda-2r\pi\cdot j)}n\cdot j d\sigma_1+(\lambda^2-\pi r^2)\epsilon^{-\alpha\lambda}\right\}\\&=\epsilon^{-\alpha\lambda}\left\{\left(1-\frac{\sigma_p}{\sigma_c}\right)+\frac{\sigma_p}{\sigma_c}\frac{\epsilon^{2r\alpha}(2r\alpha-1)+1}{2\alpha^2r^2}\right\}.\end{aligned} \tag{8}$$

The transmittance for the first layer of cells equals the same value and, making the same assumption used earlier regarding the average I_0 for the next layer, the transmittance of the specimen is

$$I/I_0=(I/I_0)_c^N \tag{9}$$

3. Discussion

It is not clear how eq (2) might be generalized further in order to demonstrate the effect of particle shape.[3] However, some easily integrable shapes can be investigated. For example, a disk-shaped particle with volume and cross-sectional area equal to that of a sphere with radius r must have thickness $4r/3$. With its flat surface parallel to the radiation wave

[3] In this connection, note that $\nabla\cdot\exp a(y_2-y_1)j\equiv\nabla\cdot\exp(-a\eta)j=\frac{\partial}{\partial\eta}\exp(-a\eta)\neq 0$, so the integrand in (2) cannot be the curl of any function and Gauss's theorem cannot be applied.

front, the particle would have a transmittance of $(I/I_0)_{\text{disk}}=\exp(-4ar/3)$. For the sphere $(I/I_0)_{\text{sphere}}=\exp(-2ar)$ for sufficiently small ar.

Equation (7) for spherical particles involves the radius in a complicated manner. If ar is sufficiently small so that terms beyond those of first degree in the expansions of $\exp(2ar)$ and $\exp(-2ar)$ can be discarded, the expression becomes

$$\ln I/I_0 \approx N \ln\left[\left(1-\frac{\sigma_p}{\sigma_c}\right)-\frac{\sigma_p}{\sigma_c}\left(1+\frac{2ar}{3}\right)(1-2ar)\right]$$

$$\approx N \ln\left(1-\frac{\sigma_p}{\sigma_c}\frac{4ar}{3}\right).$$

We may now expand this expression in a Maclaurin's series, keeping only the leading term, substitute (4) and (6), and make the simplifying assumption $m_p \ll m_k$ (which is true in practice). The result is

$$\lim_{r\to 0} \ln I/I_0 = -am_p/S\rho_p.$$

This is recognized as Beer's law for a mass m_p of sample in the form of a homogeneous condensed film. For larger particles the sensitivity of (7) to changes in r can best be demonstrated by assuming some typical values for the other parameters and plotting I/I_0 versus r (see fig. 2). There is indeed a significant dependence on particle size, which is most serious for bands with highest absorption coefficient. As these are the bands most likely to be used for quantitative purposes, the necessity for controlling particle size is clear. It is also apparent that band shape should be affected by particle size. The curves of figure 2 predict that a sample prepared with large particles will have a higher apparent transmittance than a sample with the same mass of small particles. This applies also to specimens containing clusters of small particles. In this case r must be taken as the cluster radius.

It has been observed experimentally that absorption bands do become more intense as particle size is reduced. Some observations on polyvinyl chloride have been made. It is recognized that scatter plays an undetermined role in these measurements. However, it is not likely that reduction of particle size will result consistently in *greater* scatter at an absorption band, and hence in greater apparent absorption. Furthermore, no asymmetric variations in band shapes, such as Christiansen windows, were observed.

Calculations from eq (7), using typical values [4] for the parameters, provided the encouraging result that the apparent transmittance is independent of m_k within the practical measuring limits of modern spectrophotometers. In order to verify this experimentally, two pellets were prepared containing the same quantity (2.6 mg) of stearic acid but different amounts of potassium bromide (42.25 mg and 294.85 mg). Transmittance was measured relative to base lines drawn through maxima adjacent to the minimum in question. The transmittances of corresponding bands at wavelengths greater than 9.1 μ were equal for the two pellets within 2 or 3 percent. In the range 3 to 9.1 μ bands were either too nearly opaque or were too close together to permit reasonable base lines to be drawn. The combination bands near 2.4 μ had transmittances of 78.7 and 86.1 percent for the pellet containing more and less potassium bromide, respectively.

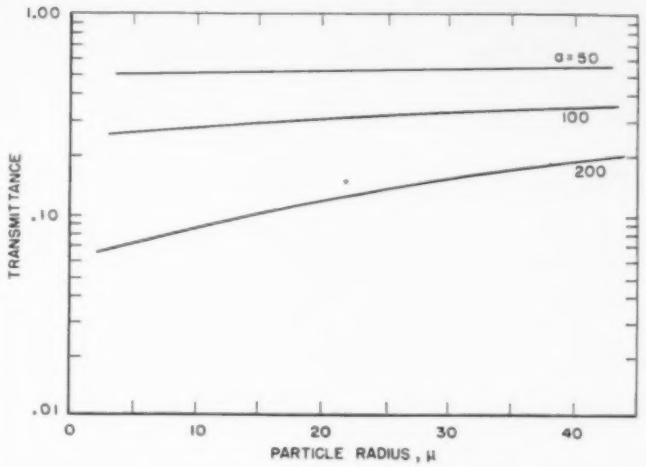

FIGURE 2. *Effect of radius of particles with various absorption coefficients on transmittance.*

Curves are calculated from eq (7), using the following values: $m_p=0.01$ g; $m_k=0.224$ g; $\rho_p=1$ g; $\rho_k=0.2$ g/cm^3; $S=0.714$ cm^2; $a=50$, 100, and 200 cm^{-1}.

In the case of alkali halide pellets the distribution of sample particles in the mixture is determined by the density of the suspending medium before pressing, that is, by the volume of material plus included air spaces. But if $m_p \ll m_k$ then ρ_k appears in (7) only in factors m_k/ρ_k so transmittance should be practically independent of ρ_k also. In the case of powder suspended in liquid the question of which value to use for ρ_k does not arise.

Figure 3 shows calculated curves plotted on semilogarithmic coordinates of I_0/I versus m_p for a condensed homogeneous film and for suspensions made with three different particle sizes. It is seen that for samples prepared from powders there are apparent "deviations from Beer's law" in the sense that straight lines are not obtained. The deviations are not great for small radii; however, it is seen again that apparent absorption is greatly reduced for larger particles or clusters.

Because there is a finite probability that radiant energy will traverse a pellet without encountering a sample particle, it is expected that the transmission for opaque particles will be somewhat greater than the instrumental transmission zero determined with an opaque shutter in the optical path. This is equivalent to stating that I/I_0 will not become zero as a approaches infinity in eq (7). Calculations using eq (7) with the parameters $a=\infty$, $\rho_p=1$ g/cm^3, $\rho_k=0.2$ g/cm^3, $S=0.714$ cm^2 $m_p=0.01$ g, and $m_k=$

[4] $m_p=2$ mg, $\rho_p=1$ g/cm^3, $\rho_k=0.2$ g/cm^3, $S=0.714$ cm^2, $a=100$ and 200 cm^{-1}, and m_k varied between 50 and 250 mg.

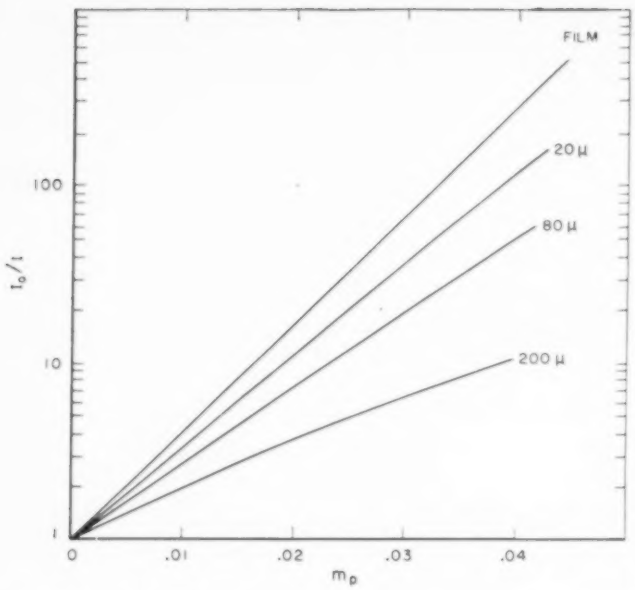

FIGURE 3. *Effect of radius of particles and mass of sample on absorbance.*

Curves are calculated from eq (7), using the following values: $a=100$ cm^{-1}; $m_k=0.224$ g; $\rho_p=1$ g/cm^3; $\rho_k=0.2$ g/cm^3; $S=0.714$ cm^2.

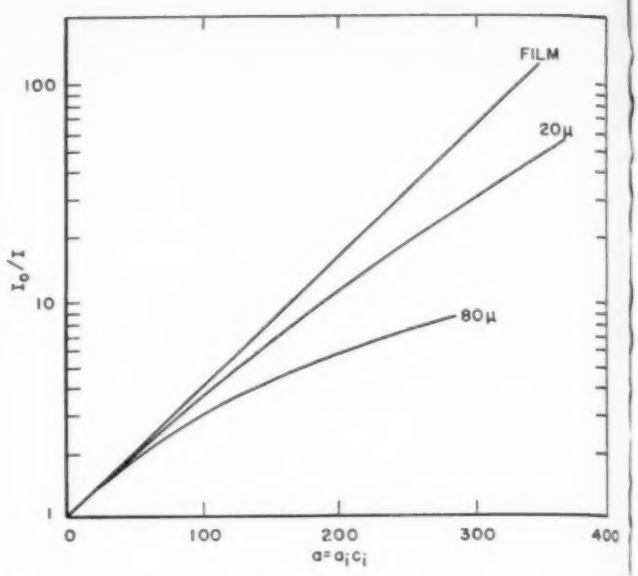

FIGURE 4. *Effect of absorption coefficient and radius of particles in multicomponent system on absorbance.*

Curves are calculated from eq (7), using the following values: $m_p=0.01$ g; $m_k=0.224$ g; $\rho_p=1$ g/cm^3; $\rho_k=0.2$ g/cm^3; $S=0.714$ cm^2.

0.224g predict that for particles up to about 47 μ in diameter the transmission zero will be raised less than 1 percent, for 72 μ diameter particles the zero will be raised to 5 percent transmission, and for 200 μ diameter particles the zero will be raised to 34 percent transmission.

Now the sample is to be considered as a multicomponent system. If the components are distributed uniformly throughout the particle, it is sufficient to define a in (3) by

$$a=\sum_i a_i c_i,$$

in which a_i and c_i are the absorption coefficient and molar concentration of the ith component. This reduces to $a=a_ic_i$ for a frequency chosen so that $a_j=0$ for $j\neq i$. It is sufficient then to discuss (7) relative to changes in a. Figure 4 contains a plot of I_0/I versus $a=a_ic_i$ for two particle sizes and a condensed homogeneous film with arbitrary values assumed for parameters m_p, m_k, ρ_p, ρ_k, and S. Deviations from linearity are serious for very large radii but can probably be disregarded for small particles uniformly distributed in the suspension. The deviations are seen to be less serious for small a. If the components are not uniformly distributed throughout the individual particles, the calculations are more difficult. An example of such a situation might occur when material undergoes chemical changes while in the form of particles. In degradation studies, for example, degradation products might be found more concentrated at the surface of the particles than in the interior.

If a is a function of p, the distance from the particle center, then Beer's law for a cylindrical increment of volume with radius z is

$$\frac{dI}{I}=-a(p)\,dx, \quad \frac{I}{I_0}=\exp\left[-\int_{r_1(z)}^{r_2(z)} a(p)\,dx\right].$$

The average transmittance of the sphere is

$$(I/I_0)_p=2\pi I_0\int_0^r \exp\left[-\int_{r_1(z)}^{r_2(z)} a(p)\,dx\right] z\,dz/\pi r^2 I_0.$$

The integration is not a convenient one even for simple forms of $a(p)$. It will not be discussed further except to stress that it is dependent on the functional form of a. It is therefore not legitimate to assume a linear "Beer's law plot" for solid particles undergoing chemical change.

We turn now to the case of transparent particles suspended in an absorbing medium. This situation occurs frequently when mulls are prepared with mineral oil, for example. It also occurs when the pellet technique is used with potassium bromide that contains some water. The limiting behavior of eq (9) for vanishing particle size may be seen by noting that $[e^{2r\alpha}(2r\alpha-1)+1]/2\alpha^2r^2$ approaches $e^{2r\alpha}$ asymptotically as r approaches zero. Further substitution of two terms of a power series for the exponentials leads to the expression

$$\lim_{r\to 0} I/I_0=\exp[-\alpha(t-\tfrac{3}{2}t_p)], \qquad (10)$$

in which t is the thickness of the suspension and t_p

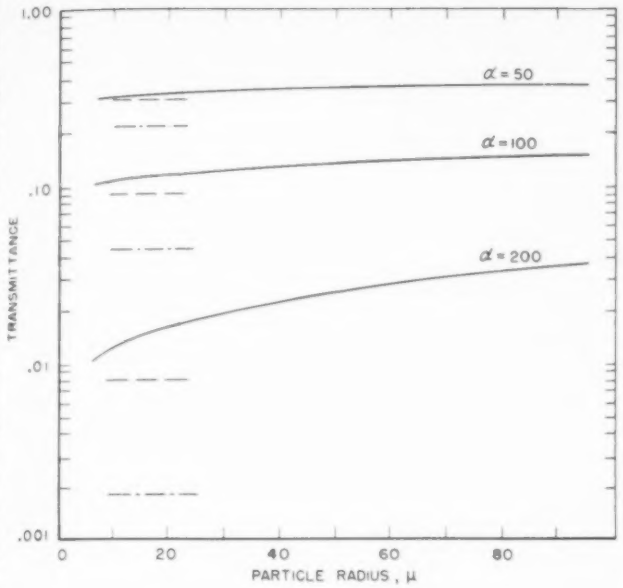

FIGURE 5. *Effect of radius of transparent particles in media with various absorption coefficients on transmittance.*

Curves are calculated from eq (9), using the following values: $m_m = 22.4$ mg; $m_p = 10$ mg; $\rho_p = \rho_m = 1$ g/cm^3; $S = 0.714$ cm^2. The dash lines represent transmittance in the limit of vanishing particle radius and the dash-dot-dash lines represent transmittance of pure material containing no particles for the corresponding absorption coefficients.

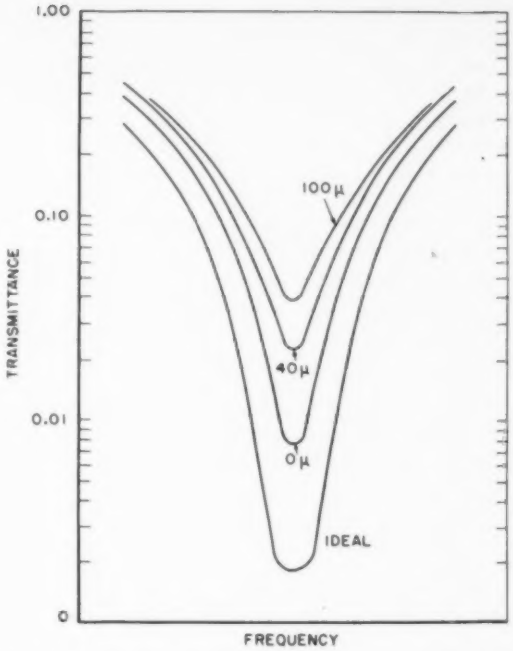

FIGURE 6. *Effect of size of transparent particles on the shape of the absorption bands of an absorbing material in which the particles are dispersed.*

The curves were drawn from the data in figure 5.

is the thickness that the powder alone would have if it were in the form of a condesned homogeneous film. The occurrence of the factor 3/2 in the exponent is surprising. Of course as r approaches zero it is no longer reasonable to integrate Beer's law over a sphere, as was done in deriving these equations. Values calculated from eq (9), using assumed parameters, are plotted versus particle size in figure 5. In general, samples containing the same amounts of material transmit more energy as the size of the suspended particles increases. The increase will occur at a greater rate for bands of higher absorption coefficient. The change in appearance of a hypothetical absorption band as particle size is varied is demonstrated in figure 6. The envelope labelled "ideal" represents liquid containing no powder as given by eq (10) without the factor 3/2.

While obtaining spectra of suspensions of polyvinyl chloride in liquid media using a double-beam spectrometer, it was observed that complete compensation for bands arising from the liquid could not be obtained. For example, if a point on each side of the band were compensated exactly by adjusting a variable thickness cell, then that portion of the band falling between these points would be overcompensated and other portions would be undercompensated. Furthermore, when a quantity of compensating liquid calculated on an "ideal" basis (i. e., from eq (10) without the factor 3/2) was placed in the reference beam, bands were strongly overcompensated. Scatter alone would not be expected to produce these symmetric changes in band shape. However, the present theory involving absorption alone gives a resonable qualitative description. For if an ideal-band envelope is calculated by using a thickness appropriate for exact compensation at points on the side of the "suspension" band, it will have greater and less transmittance than the suspension band for frequencies inside and outside these points, respectively. The difference between the two contours will produce a differential band similar to the ones observed. Attempts at compensation would be expected to be more successful with small particles.

4. Summary

A simple but plausible model of solid particles suspended in a transparent medium, with the postulate that refractive index changes over molecular-vibration absorption bands are sufficiently weak to be ignored, has yielded the following predictions:

1. The apparent absorption is dependent on particle shape.

2. The apparent absorption is dependent on particle size. Samples containing large particles transmit more energy than samples with the same mass of small particles. Absorbance as a function of mass of sample for a one component system deviates from linearity most markedly when large particles are used. For smaller particles the absorbance curve becomes linear and in fact coincides with the Beer's law plot obeyed by a condensed homogeneous film of the same material. In multicomponent systems the form of I/I_0 depends upon the way in which the components are distributed in the par-

ticles. In the case of uniform distribution within the particles, deviations from linearity in absorbance versus concentration are greatest for large particles, and again absorbance approaches that of a condensed homogeneous film for small particles. All the remarks made here regarding particle size apply to cluster size in the case of incompletely dispersed systems. The desirability of obtaining small particles and the necessity for controlling particle size distribution and for producing complete dispersion of particles in the suspension medium are clear.

3. The apparent absorption is not greatly affected by variation in mass and density of suspending material.

4. In addition, a related model of transparent particles in absorbing media has led to the conclusion that apparent transmittance of a suspending medium should increase as the size of the particles which it contains increases.

The author is grateful for discussions with Mary Reiney Harvey, F. A. Smith, and E. Carroll Creitz during the development of experimental technique. Special thanks are due D. H. Anderson for providing details of his pellet-pressing method before publication.

5. References

[1] J. E. Ard, Anal. Chem. **23,** 680 (1951).
[2] U. Schiedt, Z. Naturforsch. **7b,** 270 (1952); **8b,** 66 (1953). See also H. Hausdorff, Appl. Spectroscopy [2], **7,** 75 (1953) for a summary and some additional results.
[3] M. M. Stimson and M. J. O'Donnell, J. Am. Chem. Soc. **74,** 1805 (1952).
[4] D. H. Anderson and N. B. Woodall, Anal. Chem. **25,** 1906 (1953).
[5] A. H. Pfund, J. Opt. Soc. Am. **25,** 351 (1935).
[6] M. A. Pittman, J. Opt. Soc. Am. **29,** 358 (1959).
[7] W. C. Price and K. S. Tetlow, J. Chem. Phys. **16,** 1157 (1948).
[8] R. N. Jones, J. Am. Chem. Soc. **74,** 2681 (1952).
[9] W. R. Harp, Jr., H. Stone, and J. W. Otvos, Anal. Chem. **26,** 431 (1954). Presented at the Pittsburgh conference on Analytical Chemistry and Applied Spectroscopy (March 1954).

WASHINGTON, May 3, 1954.

Journal of Research of the National Bureau of Standards Vol. 54, No. 1, January 1955 Research Paper 2564

Branching Ratio in the Decay of Polonium-210

R. W. Hayward, D. D. Hoppes, and W. B. Mann

Using a micro-calorimeter to determine the alpha-particle activity and a sodium-iodide scintillation counter of high efficiency to measure the gamma-ray intensity, the branching ratio of polonium-210 has been found to be equal to $(1.22 \pm 0.06) \times 10^{-5}$. This value is based on the assumption that the energy of the main alpha-particle group from polonium-210 is 5.301 Mev. In the calibration of the scintillation counter the angular anisotropy of the gamma rays from cobalt-60 was found to be 1.164 ± 0.002.

1. Introduction

The number of gamma quanta emitted per disintegration of polonium-210 was recently determined by Grace, Allen, West, and Halban [1] [1] in the course of the investigation of a method for standardizing polonium sources by measurement of the hard 0.804-Mev [2: gamma radiation. The intensity of the alpha radiation emitted from a 200-mc source of polonium-210 deposited on one side of a platinum foil was measured directly by means of a low-geometry defined-solid-angle method, whereas the 0.804-Mev gamma-ray intensity was determined in terms of a source of cobalt-60 by means of a cylindrical aluminum Geiger-Müller counter of unspecified filling. The absolute disintegration rate of the cobalt-60 source, which it is assumed was of a similar geometry, to that of polonium-210, was determined by means of the method of beta-gamma coincidence counting whereas the relative efficiencies of the Geiger-Müller counter to the gamma radiations from cobalt-60 and polonium-210 were assumed to be the same as those determined for a counter of similar geometry by Bradt, Gugelot, Huber, Medicus, Preiswerk, and Scherrer [3].

The opportunity has arisen to repeat the measurement of the branching ratio of polonium-210 using, however, a micro-calorimetric method to determine the rate of alpha-particle emission and a sodium-iodide scintillation counter, of high detection efficiency, to determine the intensity of the 0.804-Mev gamma rays by comparison with a cobalt-60 source, the gamma-ray intensity of which was determined by the method of gamma-gamma coincidence counting.

2. Preparation of the Polonium-210 Sources

Experiments were performed on two polonium-210 sources, the first of which, however, was too weak to give satisfactory accuracy. This had been supplied sealed in a nickel tube about 1.5-cm long and 0.15-cm in external diameter. The gamma-ray spectrum indicated some energetic gamma-emitting contamination, but with an activity corresponding to 3.7 mc only a very approximate value for the branching ratio of 1.1×10^{-5} gamma quantum per alpha particle was obtained.

The second polonium-210 source was prepared from some 60 mc of solution that had been carefully purified prior to delivery. This purification consisted of depositing polonium-210 onto a silver foil from a stock solution containing approximately 130 mc of polonium-210. The silver foil was then washed free from solution and dissolved in concentrated nitric acid. After expelling most of the nitric acid by evaporation the silver was precipitated by means of hydrochloric acid. The solution was filtered from the silver chloride and its acidity adjusted for deposition on a second silver foil, which was again processed in the same way as the first, the filtrate from the silver chloride being the final solution containing some 60 mc of purified polonium-210.

Upon receipt of this solution its acidity was adjusted to a value of pH equal to 1 and 0.1 g of finely powdered silver was allowed to stand in the solution overnight. After standing for this time the solution was filtered through a plug of glass wool in a glass tube having external and internal diameters of approximately 3 and 2 mm. The silver powder that was retained by the glass-wool plug was ultimately found to have extracted some 50 mc of the polonium-210. The glass tube was then fused off below the glass-wool plug and above the silver powder to give a source 37-mm long and whose approximate form is illustrated in figure 1. On examination of its gamma-ray spectrum, this source was found to be free from the contamination that had been present in the first source.

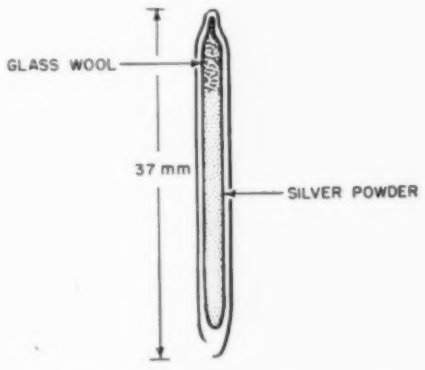

FIGURE 1. *Polonium-210 source.*

[1] Figures in brackets indicate the literature references at the end of this paper.

3. Measurement of the Alpha-Particle Activity

The alpha-particle intensity of the polonium-210 source was determined by means of a gold-cup radiation balance that was constructed to compare four national radium standards [4]. The energy emission was combined with an average value [2] of 5.301 Mev for the energy of the polonium-210 alpha particles to give their intensity.

As this radiation balance had previously been used primarily for relative measurements, it was carefully recalibrated so as to give absolute rates of energy dissipation. Such a calibration consists essentially in determining an average value of dE/dT for the two Peltier couples, and for this purpose a completely new set of compensated calibration coils, encased in copper sheaths and with permanent potential leads, was constructed. Previous calibrations had been made with coils that had been wound on glass of such dimensions as to simulate the United Kingdom and the United States Hönigschmid primary radium standards and the Canadian national radium standard [4]. The results obtained for dE/dT with the "Hönigschmid", "Canadian", and the new copper-sheathed coils are shown in table 1.

TABLE 1. *Measurement of the thermoelectric power, dE/dT at 25° C*

Coil	dE/dT[a]
	$\mu w/deg$
"Hönigschmid"	58.86
Do	58.95
"Canadian"	58.71
Do	58.59
Copper-sheathed	58.49
Do	58.67
Do	58.89
Do	58.79
Do	58.79
Do	58.60
Do	58.70
Do	58.62
Do	58.53

[a] The average value of dE/dT is 58.71 μw/deg at 25° C.

The source of polonium-210, that is illustrated in figure 1, is such as to enable a further important check to be made in connection with the operation of the radiation balance. It has been assumed [4] that the thermal "mixing" in the gold cups is of such a magnitude as to render any differences in temperature distribution in the cups due to difference in source geometry unimportant. A series of measurements was carried out therefore with the polonium-210 source, and a dummy source containing a glass-wool plug and inactive silver powder, in which the energy emission from the source in the erect position, as in figure 1, was compared with that as measured with the source and dummy upside down. In the erect position the polonium-210 is concentrated in the lower part of each cup in turn, whereas in the upside-down position a relatively good thermal insulator, the glass-wool plug, is in close proximity with the Peltier couples at the bases of the cups.

[3] From values 5.304 and 5.298 Mev [5, 6].

TABLE 2. *Energy dissipation from polonium-210 source as measured in erect and upside-down positions*

Date, 1954	Energy emission (erect)	Energy emission (upside down)
	μw	μw
June 22	1323.6	1332.4
June 29	1276.9	1275.9
July 6	1235.2	1234.9
July 20	1151.2	1151.2

TABLE 3. *Energy dissipation from polonium-210 as a function of time*

Date, 1954	Time (EST)	Hours from zero	Observed energy emission	Energy emission corrected to zero date [a] (using half-life of 138.39 days)
			μw	μw
June 22	13.30	−167.75	1325.6	1278.1
June 29	13.15	0	1276.9	1276.9
July 6	15.05	169.75	1235.2	1279.8
July 13	14.40	337.25	1190.5	1277.3
July 20	14.20	505.25	1151.2	1279.2
August 24	13.25	1344.25	961.43	1272.8
August 31	10.05	1508.75	929.29	1273.2
September 7	14.30	1681.25	899.37	1277.5

[a] Average value is 1276.9 μw, with a standard deviation of 0.2 percent.

As is seen from table 2, there is no significant difference between the measurements in the two positions; the difference between the first two measurements is not outside the possible range of experimental error.

Finally, in table 3 the results are shown for rate of energy emission from the polonium-210 source on various dates of measurement. Also shown are the values that have been obtained after correction, using a half-life of 138.39 days [7], to a zero date of 13.15 hours EST on June 29, 1954, on which date, in the morning, the gamma-ray intensity was determined.

Using an alpha-particle energy of 5.301 Mev, which corresponds to a total disintegration energy of 5.404 Mev, and the average value of 1276.9 μw for the energy emission, the alpha-particle activity at the above time is found to be $1{,}475\times10^6$ disintegrations per second. As the gamma-ray measurements were made some 3 or 4 hours earlier, it is appropriate to correct this value to $1{,}476\times10^6$ disintegrations per second at the time of the gamma-ray experiment.

4. Measurement of the Gamma-Ray Intensity

The intensity of the gamma radiation from the same polonium-210 source as used in the above experiment was determined by comparison with a cobalt-60 source, in the form of cobaltous chloride in aqueous solution, through the use of a sodium-iodide scintillation counter of high detection efficiency. The disintegration rate of the cobalt-60 source had been determined absolutely by the coincidence method.

The experimental procedure was as follows: The polonium-210 and cobalt-60 sources of identical dimensions as in figure 1 were placed alternatively on the axis of, and 3 in. from the face of, a cylindrical sodium-iodide, thallium-activated, crystal, 5 in. in diameter and 4 in. long, as shown in figure 2. This crystal was hermetically sealed in a thin aluminum container, using magnesium oxide as a diffuse reflector on all surfaces except that which was viewed by a 5-in. diameter photomultiplier (type K1198). The output of the photomultiplier tube was fed through a linear amplifier into a single-channel differential pulse-height analyzer from which the intensity versus pulse-height spectra shown in figure 3 were obtained. As the sodium-iodide crystal is not quite totally absorbing, the relative efficiency for the detection of the gamma rays from the polonium and cobalt sources must be calculated. This relative efficiency is given by

$$\epsilon=\frac{\int_0^{\alpha}(1-e^{-\mu(E_1)\rho r(\beta)})\sin\beta\,d\beta}{\int_0^{\alpha}(1-e^{-\mu(E_2)\rho r(\beta)})\sin\beta\,d\beta}, \qquad (1)$$

where

$r(\beta)=t\sec\beta \qquad 0\leq\beta\leq\tan^{-1} r/(D+t)=\beta'$

$r(\beta)=r\csc\beta-D\sec\beta \qquad \beta'\leq\beta\leq\tan^{-1} r/D=\alpha$

$\mu(E)$ = mass absorption coefficient for energy E

ρ = density.

The values of $\mu(E)$ for sodium iodide were obtained from the tables of White [8] for energies corresponding to those of 0.804 and 1.25 Mev, the latter value being the average energy of the cobalt-60 gamma rays; this artifice introduces negligible error. For the geometry and dimensions given in figure 3, one obtains a value 1.123 for the relative detection efficiency, ϵ, by numerical integration of eq (1). The disintegration rate for the polonium gamma ray is given by

$$N_{0\gamma}(\mathrm{Po}^{210})=\frac{A(\mathrm{Po}^{210})}{\epsilon A(\mathrm{Co}^{60})}N_0(\mathrm{Co}^{60}), \qquad (2)$$

where A is the area under each of the spectra of figure 3. The area under the cobalt-60 spectrum is given proper weight to take into account the cascade nature of the gamma radiation. Four determinations of the relative areas give a value $A(\mathrm{Po}^{210})/A(\mathrm{Co}^{60})=0.648$, thus we obtain a value for the disintegration rate of the polonium gamma ray in terms of the Co^{60} disintegration rate, i. e.,

$$N_{0\gamma}(\mathrm{Po}^{210})=0.5770N_0(\mathrm{Co}^{60}).$$

The estimated error of this relationship may be as great as 5 percent because of the uncertainty in correcting for secondary effects, such as backscattering into the detector.

The disintegration rate of the cobalt-60 source was determined by the gamma-gamma coincidence method. This disintegration rate in terms of ob-

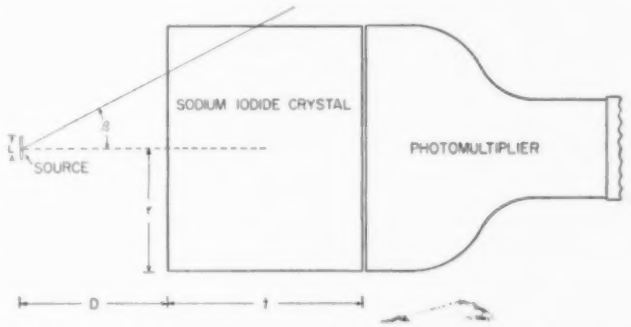

FIGURE 2. *Geometrical arrangement for comparison of gamma-ray spectra of cobalt-60 and polonium-210 sources.*

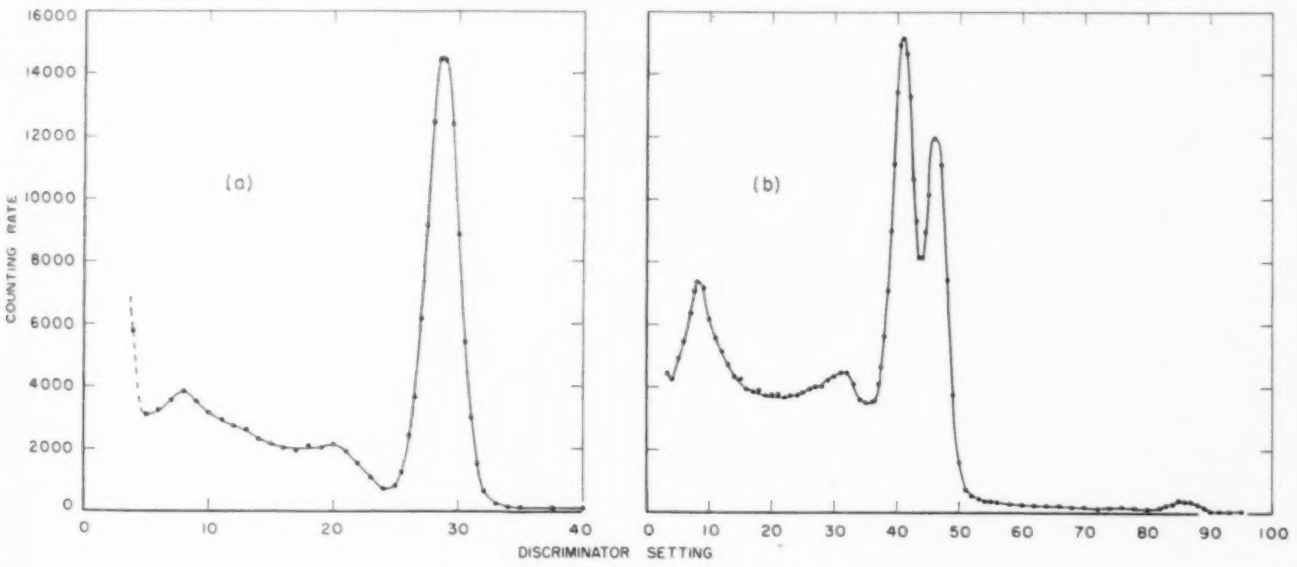

FIGURE 3. *Scintillation pulse-height spectra of* (a) *polonium-210 source,* (b) *cobalt-60 source.*

servable quantities is given by

$$N_0=\frac{N_1N_2}{N_c}\frac{\zeta_1+\zeta_2}{(\zeta_1+1)(\zeta_2+1)}f(\vartheta), \tag{3}$$

where N_1 and N_2 are the counting rates in each of two similar counters, N_c is the number of coincidence counts between the two counters, ζ_1 and ζ_2 are the ratio of efficiencies for the two gamma rays in the first and second counters, respectively, and $f(\vartheta)$ is a function depending on the geometry of the source, counters, and any angular correlation between the coincident gamma rays. For the cobalt-60 source where there is a definite angular correlation, this function takes the form (9).

$$\begin{aligned}f(\vartheta)=1&+(J_2/J_0)^2 0.1020P_2(\cos\vartheta)\\&+(J_4/J_0)^2 0.0091P_4(\cos\vartheta)\\&+\tfrac{1}{4}(L/D)^2[1-P_1(\cos\vartheta)]\{0.1020P_1(\cos\vartheta)\\&+0.0091[P_1\cos\vartheta+\tfrac{7}{3}P_3(\cos\vartheta)]\}\end{aligned} \tag{4}$$

The terms containing J_l are attenuation coefficients due to the finite angular resolution of the counters, where the J_l is given by

$$J_l(\alpha)=\int_0^\alpha P_l(\cos\beta)(1-e^{-\mu(E)\rho x(\beta)})\sin\beta\,d\beta. \tag{5}$$

The expression for $x(\beta)$ is of the same form as in eq (1). The last term in eq (4) is a correction term [10] due to the finite length of the source. The numerical coefficients of the Legendre polynomials are theoretical values for a cascade transition between states with spins $4\rightarrow2\rightarrow0$ [11].

With a geometry as shown in figure 4, the theoretically expected anisotropy is $f(\pi)/f(\pi/2)=1.150$. The experimentally observed value was 1.147, indicating that when the corrections for the finite sizes of source and counters are accounted for, the measured differential anisotropy of 1.164 is well within the probable error (approximately 1 percent) of being the same as the theoretically expected value of 1.167 [11].

Several determinations of the disintegration rate under different geometrical conditions gave a value

$$N_0(\mathrm{Co}^{60})=(3.087\pm0.030)\times10^4\ \mathrm{dps}.$$

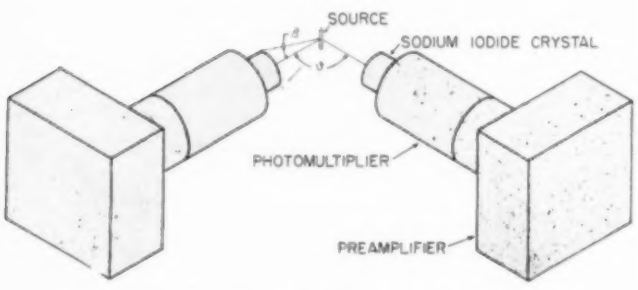

FIGURE 4. *Geometrical arrangement for coincidence measurements on cobalt-60 source.*

Using this value, we obtain as the intensity of the polonium-210 gamma rays

$$N_{0\gamma}(\mathrm{Po}^{210})=(1.782\pm5\%)\times10^4\ \mathrm{dps}.$$

5. Branching Ratio

Combining the gamma-ray and alpha-particle intensities, the following value for their ratio is obtained:

$$\frac{N_{0\gamma}}{N_{0\alpha}}=\frac{1.782\times10^4}{1.476\times10^9}$$

$=(1.20_7\pm0.06_0)\times10^{-5}$ gamma quantum per alpha particle.

This value of $(1.21\pm0.06)\times10^{-5}$ is to be compared with that of $(1.8\pm0.14)\times10^{-5}$ obtained by Grace, Allen, West, and Halban [1] and $(1.6\pm0.2)\times10^{-5}$ by M. Riou [12]. The internal conversion of K-shell electrons in polonium-210 is 0.0084 [13] and correction for L-shell conversion electrons [14] gives a total conversion coefficient of 0.0107. Using this value, the branching ratio is found to be $1.22\times10^{-5}\pm5$ percent.

Grateful acknowledgment is made to A. Schwebel for his assistance in preparing the polonium–210 source from the solution received, to H. B. Kearney and M. Pavey of the Canadian Radium and Uranium Corporation for their cooperation in the preparation of the purified polonium-210 solution, and to H. W. Koch for the use of the large sodium-iodide crystal.

6. References

[1] M. A. Grace, R. A. Allen, D. West, and H. Halban, Proc. Phys. Soc. **64**, 493 (1951).
[2] R. W. Pringle, H. W. Taylor, and S. Standil, Phys. Rev. **87**, 384 (1952).
[3] H. Bradt, P. C. Gugelot, O. Huber, H. Medicus, P. Preiswerk, and P. Scherrer, Helv. Phys. Acta **19**, 77 (1946).
[4] W. B. Mann, J. Research NBS **53**, 277 (1954) RP2545.
[5] E. R. Collins, C. D. McKenzie, and C. A. Ramm, Nature **167**, 682 (1951).
[6] W. J. Sturm and V. Johnson, Phys. Rev. **83**, 542 (1951).
[7] D. C. Ginnings, Anne F. Ball, and D. T. Vier, J. Research NBS **50**, 75 (1953) RP2392.
[8] G. R. White NBS report 1003 (unpublished).
[9] M. E. Rose, Phys. Rev. **91**, 610 (1953).
[10] J. S. Lawson, Jr., and H. Frauenfelder, Phys. Rev. **91**, 649 (1953).
[11] S. P. Lloyd, Phys. Rev. **83**, 716 (1951).
[12] M. Riou, J. phys. radium **13**, 244 (1952).
[13] M. E. Rose, G. H. Goertzel, and C. L. Perry, K-shell internal conversion coefficients, ORNL Report No. 1023 (1951).
[14] D. E. Alburger and G. Friedlander, Phys. Rev. **81**, 525 (1951).

WASHINGTON, September 22, 1954.

Journal of Research of the National Bureau of Standards Vol. 54, No. 1, January 1955 Research Paper 2565

Mechanism of High-Speed-Waterdrop Erosion of Methyl Methacrylate Plastic

Olive G. Engel

A mechanism for the high-speed-waterdrop erosion of methyl methacrylate plastic is postulated as a result of a parallel study of the damage that is done by the impacts of steel spheres and of deforming lead pellets. Results of the parallel study are described. The mechanism can be extrapolated with safety only to other brittle materials of low tensile strength, the other characteristic properties of which are closely similar to those of methyl methacrylate plastic.

1. Introduction

The erosion that waterdrops cause when they strike solid surfaces at very high velocities has recently received considerable attention because of the damage that is produced when high-speed aircraft fly through rain. This erosion is essentially the same as that which occurs in steam turbines because of the waterdrops in wet steam. The process has been studied for the past 25 years [1],[1] but no clear understanding of the complete damage mechanism has emerged.

Any attempt to explain the damage that results from high-speed-waterdrop impingement must take into account the properties of the waterdrop under impact conditions because the high-speed waterdrop is the damage tool. That is, the destructive force that causes this type of damage is a result of the impact of the waterdrop against the solid surface. Under impact at a velocity of the order of the speed of sound in air, water acts as though it were hard, but it retains its liquid property of flow. It has recently been estimated [2] that the impact pressure that results from a collision of this type at an impact velocity of 600 mph is of the order of 30,000 psi and that the radial-flow velocity is close to 1,400 mph.

The damage that results from these high-speed liquid-to-solid collisions is equally a function of the properties of the structural material that sustains the damage. The response of materials of different properties will be different enough to introduce notable modifications in the erosion process.

The analysis of a difficult problem may sometimes be accomplished by reducing it to a simpler problem that is easier to understand. It was suggested by Schröter [3] in regard to cavitation erosion, for example, that physically parallel studies might be more rewarding than further observations of the cavitation progress itself because the cavitation cannot be reduced to slow motion nor separated from other phenomena. As just pointed out, under impact conditions a waterdrop behaves like a hard sphere, but unlike a sphere of hard, solid material, it retains its liquid property of flow. The results of the parallel study of the impact of steel spheres, and especially of deforming lead pellets, on methyl methacrylate plastic appears to indicate the mechanism of high-speed-rain erosion.

[1] Figures in brackets indicate references at the end of this paper.

2. Collision of Steel Spheres and of Deforming Lead Pellets with Methyl Methacrylate Plastic

The plastic blocks used for this study were of Plexiglas I–A obtained from the Rohm & Haas Co. in ¼-, 1-, and 3-in. thicknesses. The projectiles were 7/32-in. steel spheres, 0.22-in.-diameter soft deforming lead pellets that were shot with small charges of powder from a 0.22-caliber gun, and 5/16-in. steel spheres that were shot from a 0.30-caliber gun. The impact velocities were determined by momentum transfer to a pendulum through the block of plastic.

The impacts resulted in a characteristic type of fracture of the plastic. At relatively low velocities of impact, circles of short, very fine, straight cracks were observed (see figs. 1, 2, and 3). These straight cracks were perpendicular to radii from the central point of impact. The center spot of the impact was, however, completely without any such cracks. At relatively high velocities of impact, the circular region of fine cracking on the impact surface was bounded by a very well-defined circular crack when the projectiles were steel spheres. Such a crack was not observed at these velocities when the projectiles were lead pellets. However, in the latter case, a circular subsurface shear crack was produced. These subsurface shear cracks appear as large dark circles, with their center at the center of the damage site in figure 3. They are out of focus with the surface details.

Radial cracking resulted from the impacts of steel spheres but not from those of deforming lead pellets. On thin plates of Plexiglas I–A and at low velocities the radial cracking appeared first on the side of the plate opposite to the impact face. At high velocities on these thin plates the radial cracks penetrated through the plate to the impact surface. On the thick plates, very short radial cracks appeared on the impact surface itself. They were observed only at relatively high velocities.

A detailed discussion of the specific types of cracking and of a model that explains the observations is contained in the following sections.

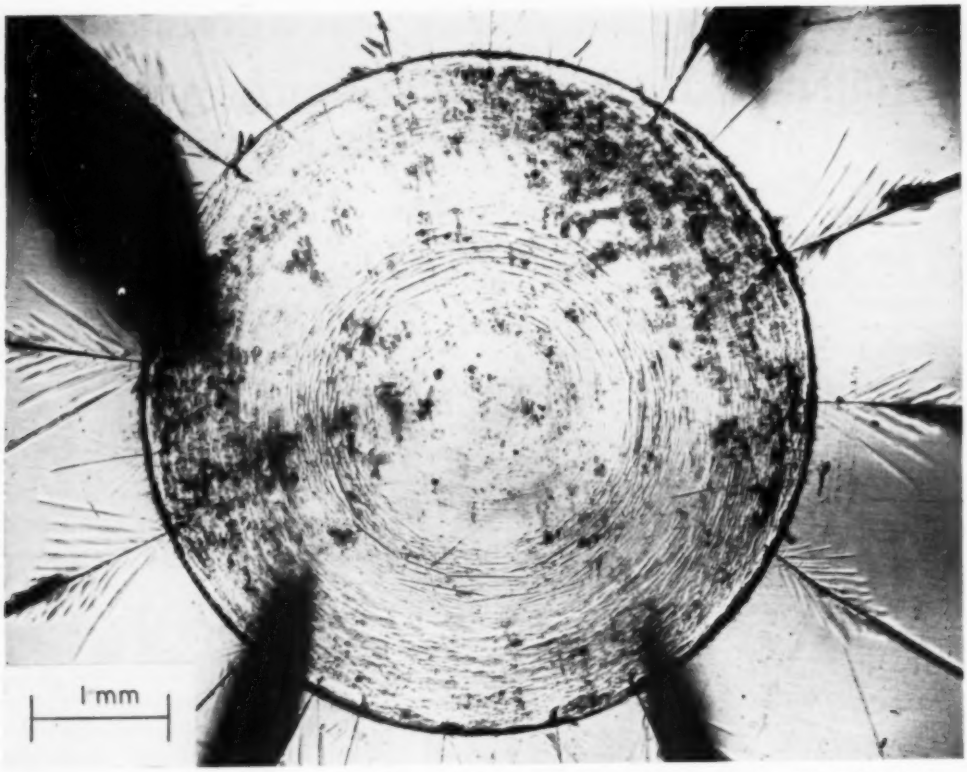

FIGURE 1. *Damage site produced by a steel sphere on impinging against Plexiglas I–A.*

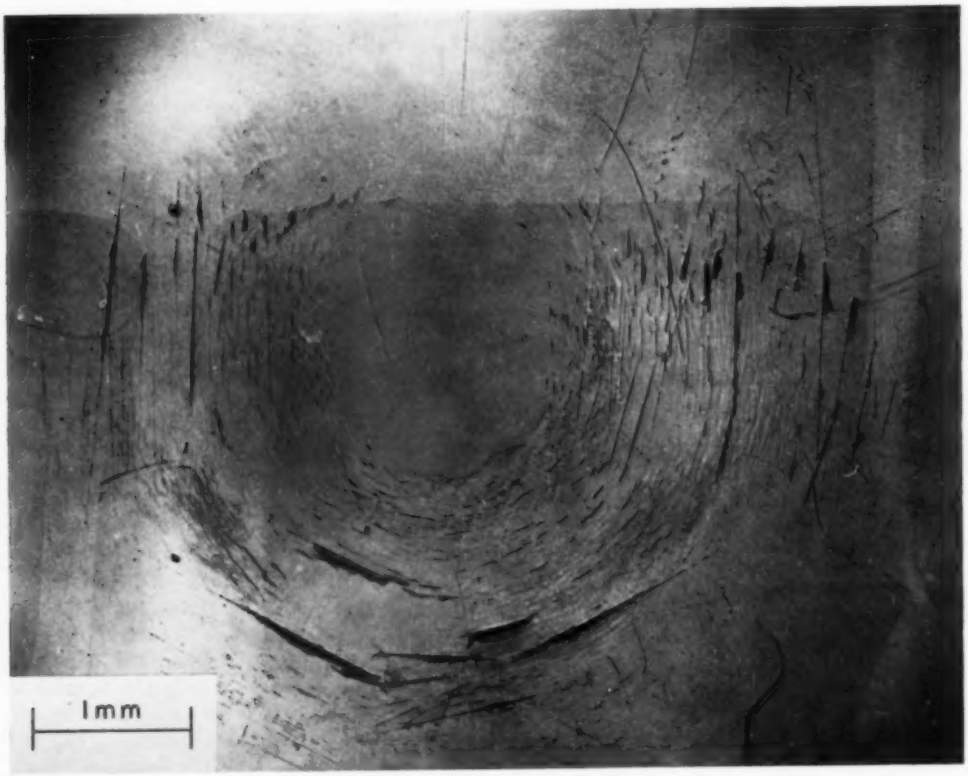

FIGURE 2. *Damage site produced by a deforming lead pellet on impinging against Plexiglas I–A.*

FIGURE 3. *Damage site produced on Plexiglas I–A as a result of a multiple shot with deforming lead pellets.*

The center area of two shots can be seen in the picture. Part of the damage caused by two other shots can be seen to one side.

2.1. Circular Crack and Fine Cracking in the Circular Zone

At low impact velocities both for impacts of steel spheres and for impacts of deforming lead pellets the damage consisted only of a few circles of fine, short, straight cracks that enclosed the central point of the impact. The central point of the impact itself was free of any cracking (see figs. 1, 2, and 3). As the velocity was increased, the amount of fine cracking increased, and the diameter of the zone of fine cracking increased. Finally, a velocity was reached at which a well-defined crack formed around the circular zone of fine cracking when steel spheres were used as projectiles (see fig. 1). This outer crack was too deep for a depth measurement with the interferometer. When deforming lead pellets were used, subsurface shear cracks formed at high velocities. The subsurface shear cracks appear as broadened arcs of a circle out of focus with the surface details (see fig. 3).

The diameter of the circular zone of fine cracking for comparable velocities was influenced by the thickness of the plastic plate only in the case where the plate thickness was as low as ¼ in. Comparison of the diameters of damage sites on 1-in.-thick and on 3-in.-thick blocks of Plexiglas I–A for 5/16-in. spheres at comparable velocities showed that they

FIGURE 4. *Cross section of a region of fine cracking bounded by a well-defined circular crack similar to that shown in figure 1.*

were essentially the same. Comparison of the diameters of damage sites on ¼-in.-thick and on 3-in.-thick Plexiglas I–A for 5/16-in. spheres at comparable velocities showed that the diameters on the ¼-in.-thick material were larger.

The diameter of the circular zone of fine cracking for comparable velocities also varied with the diameter of the steel sphere. Comparison of the diameter of the damage site produced by a 7/32-in. sphere with that produced by a 5/16-in. sphere on ¼-in.-thick Plexiglas I–A at the same velocity showed that the damage site produced by the larger sphere was the larger.

An interferometric study of the circular region bounded by fine cracking indicated that the cross section of this region must be as indicated in figure 4.

When deforming lead pellets were used, the cracks were widened and material was broken out of the surface. The widening of the cracks was in the direction of the radial flow of the lead. The breaking out of material was along cracks, was in the direction of the flow of the lead, and was on the side of the crack away from the center of the impact (see figs. 2 and 3). The widening of cracks and the breaking out of material was notably absent where steel spheres were used as projectiles.

2.2. Radial Cracking

Cracks appeared that went out radially from the circular crack in the case of the impacts of steel spheres. They were especially evident in the damage marks left by the impact of steel spheres against the thick blocks of plastic. These cracks extended only a very short distance within the circular region of fine cracking. In figure 1 they appear as feather-like structures around the circular crack.

There was also another type of cracking that occurred as a result of the impact of steel spheres when the plastic plates were thin. This was a radial, or star-shaped, cracking similar to that which results from the impact of a small, hard object against thin glass plates. In the case of ¼-in.-thick Plexiglas I–A these radial cracks appeared on the *side of the plastic opposite the impact face* at relatively low velocities. They converged under the central point of the collision. They did not extend all the way through the plate to the impact surface. Furthermore, there was no circular crack or circular area of fine cracking on this reverse face of the plate. At high velocities these radial cracks extended completely through the plate to the impact surface.

These radial cracks were quite long. In the case of impacts of 5/16-in. spheres at the relatively low velocities of 232 and 269 ft/sec the cracks were over 2 in. long and for the higher of these two velocities

were close to 3 in. long. On the other hand, radial cracks that resulted from the impact of 7/32-in. spheres at the high velocities of 611 and 943 ft/sec were only about 1½ in. long. From this it would appear that the length of these cracks may be a function both of velocity and of sphere diameter. It would seem that the total crack length should correlate with the energy transferred to the plastic by the sphere.

Bowman, Smith, and Kies [4] have plotted total length of radial cracking against velocity and have found a maximum in the curve for Plexiglas I–A at a velocity of 775 ft/sec, and for Plexiglas II at a velocity of about 875 ft/sec. They were using 5/16-in.-diam steel spheres. The shots were made against 6-in.-square plates of plastic that were ¼ in. thick. The reported maximum is a suppressed maximum that was observed under these experimental conditions. They found, furthermore, that Plexiglas II that had been subjected to hot-work reached maximum crack length at a lower velocity than Plexiglas II in the as-received condition.

2.3. Crazing in a Circle

The fine cracking that has been observed at the damage sites produced by the impacts of steel spheres and of deforming lead pellets on Plexiglas I–A may be designated as crazing. In the case of the cup-shaped depression that must form when a steel sphere or lead pellet strikes a plastic surface, the tensile stresses extend as radii from the central point of impact, which is under compression, to the rim of the cup-shaped cavity. The fine cracking that forms as a result of these tensile stresses is more or less parallel in tiers that form at an angle to one another, but the individual fine cracks are not mutually parallel.

Recently, Wolock and Newman [5] have traced the cross section of a craze crack of the generally accepted type with the interferometer. They have found that the surface material is raised on both sides of the crack (see fig. 5). It may be postulated that such cracks form as stress relievers after the material has reached the limit of stress relief from plastic flow, or if plastic flow cannot take place fast enough. If plastic flow has occurred either prior to or concomitant with the formation of the craze crack, the material will tend to come back into its original position after the stress is relieved, and the crack will be raised on each side as is observed. As a part of the present investigation, Dr. Newman made a similar interferometric study of the fine cracking that was produced by the impact of a steel sphere on Plexiglas I–A and found that a raised ridge exists on both sides of the crack, as shown in figure 5.

FIGURE 5. *Cross section of a craze crack (or fine crack) as found by use of the interferometer.*

2.4. A Model for the Impact Damage of Deforming Lead Pellets and Steel Spheres on Methyl Methacrylate Plastic

The observations that have been described can be explained rather easily by a simple model in which it is assumed that the impact of a steel sphere or of a deforming lead pellet produces a cup-shaped cavity in the plastic by compressing it. Tensile stresses should then be introduced in the regions indicated as A, B, and C in figure 6. The stresses in region A should become important as soon as any depression takes place, regardless of how shallow it may be. On the other hand, stresses that are introduced in the regions indicated as B and C may only become appreciable after the cup-shaped cavity reaches the more acute stage of depression indicated schematically in figure 6. The stresses in region B exist over the relatively sharp angle between the undisturbed surface and the wall of the depression.

It is postulated in section 2.3 that craze cracks may form as stress relievers after a material that is under tensile stress has reached the limit of stress relief from plastic flow or if plastic flow cannot take place fast enough. Similarly, the fine cracking, which appears to be crazing, should serve to relieve the tensile stresses, indicated as A in figure 6, that are produced as the plastic material is depressed by the impact. A cavity as deep as that indicated schematically in figure 6 will only be produced at high impact velocities and only by a sphere that does not flow on impact. Hence, the tensile stresses at B should only become acute at high velocities, and then only in the case where a steel sphere rather than a deforming lead pellet is the projectile. These stresses may be responsible for the well-defined circular crack that forms at high impact velocities around the circular region of fine cracking in the damage sites produced by the impact of steel spheres. The tensile stresses, indicated as C in figure 6, may be responsible for the feather-like cracks that go out

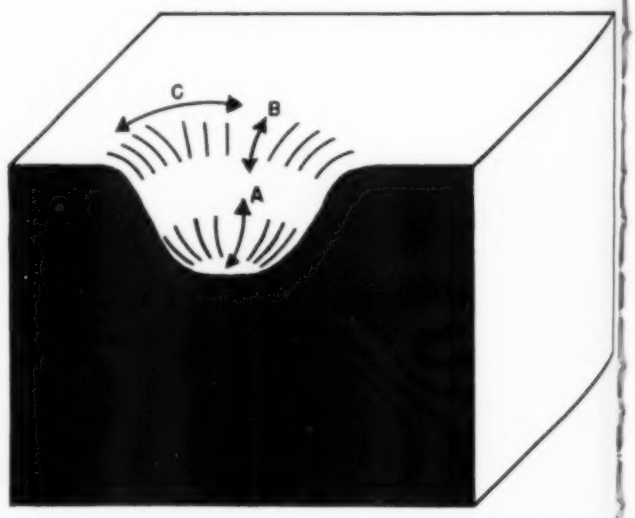

FIGURE 6. *Tensile stresses at a cavity formed by pressing hard sphere into deformable material.*

radially from the circular crack in the case of the impacts of steel spheres.

On this model, figure 6, there should be severe compression during the impact where the hard sphere is bearing against the plastic to form the cup-shaped cavity. McAdam, Geil, and Jenkins [6] have pointed out that material under compression does not tend to undergo a tensile failure. It is notable that there is no fine cracking in the severely compressed region at the center of the damage sites (see figs. 1, 2, and 3).

In the light of the model that has been assumed, essentially the same diameter of circular cracking would be expected to occur on a 1-in.-thick plate as on a 3-in.-thick plate of plastic, that is, for those plate thicknesses that are large in comparison with the shot diameter. It is also expected that for a much thinner plate, the diameter of the damage site would be increased by the bowing of the plate as a whole around the impinging sphere or pellet. This was observed to be the case.

Furthermore, on the model that has been assumed, a gradient of tensile stress would be expected up the sides of the cup-shaped depression, that is, along the arrow marked A in figure 6. Griffith [7] derived an expression that showed that there should be a maximum crack length for every value of stress that produced a crack. A magnification of the fine-cracked circular region produced by one of the shots shows some evidence that the lengths of the fine cracks at any given distance from the central point of impact are, in general, qualitatively of the same size, and that there is a size gradient from the rim to the bottom of the depression. However, there are many exceptions to this observation.

The radial cracks that are observed when the projectiles are steel spheres and that appear first on the reverse side of the plate can be explained as tensile failures. After the compressional wave produced by the impact on a relatively thin plate (one-dimensional case) has just moved through the plastic, the plastic material on the free face opposite the impact surface should tend to bulge when the compressional wave reflects there as a tensile wave. It is possible that a star-shaped hole may open to relieve the tensile stress. After the compressional wave has reflected as a tensile wave, the plastic material should snap back into a star consisting of radial cracks only. A search was made for this effect by H. L. Smith [8], using a high-speed camera operating at 15,000 frames a second. The star-shaped crack appeared, however, in the space of one frame. It is possible that the stress may be relieved sufficiently by crack formation alone, and that a star-shaped hole may never form. A camera having a higher operating speed will be needed to determine this.

The deforming lead pellets used as projectiles flowed on impact to approximately twice their original diameter. This flow of the lead produces a force against any surface irregularity in its path which, in conjunction with the restraint of the irregularity by the underlying material, results in a torque tending to break the material in the irregularity away from the underlying material. The raised ridges along the fine cracks could constitute bearing points for this torque and offer an explanation for the observed fact that where lead pellets were used as projectiles the cracks were widened and material was broken out of the surface along the cracks and in a direction away from the center of the impact (the direction of the flow of the lead) (see figs. 2 and 3).

This flow property of the lead also explains the subsurface shear cracks that appear as large dark circles out of focus with the surface details in figure 3. The flow of the lead over the surface while it is simultaneously compressed against the surface would tend to move the surface layer of the plastic with respect to the under layers. The subsurface cracks are not observed in the damage sites produced by the steel spheres, which did not flow as a result of the collision.

It is the flow property of the deforming lead pellets that makes the damage sites produced by them different from the damage sites produced by the steel spheres. The fracture that results from the impact of deforming lead pellets is more nearly related to what must happen when liquid drops strike a surface than is the fracture that results from the impact of steel spheres. In the case of waterdrops, of course, the damage from a single blow cannot be as decisive as that which results from a single impact of a deforming lead pellet because the density of water is so much lower than that of lead. The damage caused by high-speed impact of waterdrops on methyl methacrylate plastic is discussed in detail in the following sections.

3. High-Speed-Rain Erosion of Methyl Methacrylate Plastic

The preceding study of the impact of steel spheres and of deforming lead pellets on methyl methacrylate plastic is a physically parallel study to the high-speed-rain erosion of brittle plastics of low tensile strength. To make a realistic approach to the mechanism of the high-speed-rain erosion process, it is essential to keep in mind that the projectile is a water sphere that acts as though it were hard but that is capable of an extremely fast radial flow the instant after it impinges.

The process of high-speed-rain erosion should be very similar to the process of producing damage by impacts with deforming lead pellets. For plastics that are similar in properties to methyl methacrylate plastic, radial fine cracking should form around the point of impact of a hard, impinging, spherical waterdrop due to the tensile stresses that are produced when the compressive impact stress forms a cup-shaped cavity in the material. A breaking out of material from the surface should be observed as a result of the rapid radial flow of the water after the collision over the raised ridges of the fine cracks that have formed.

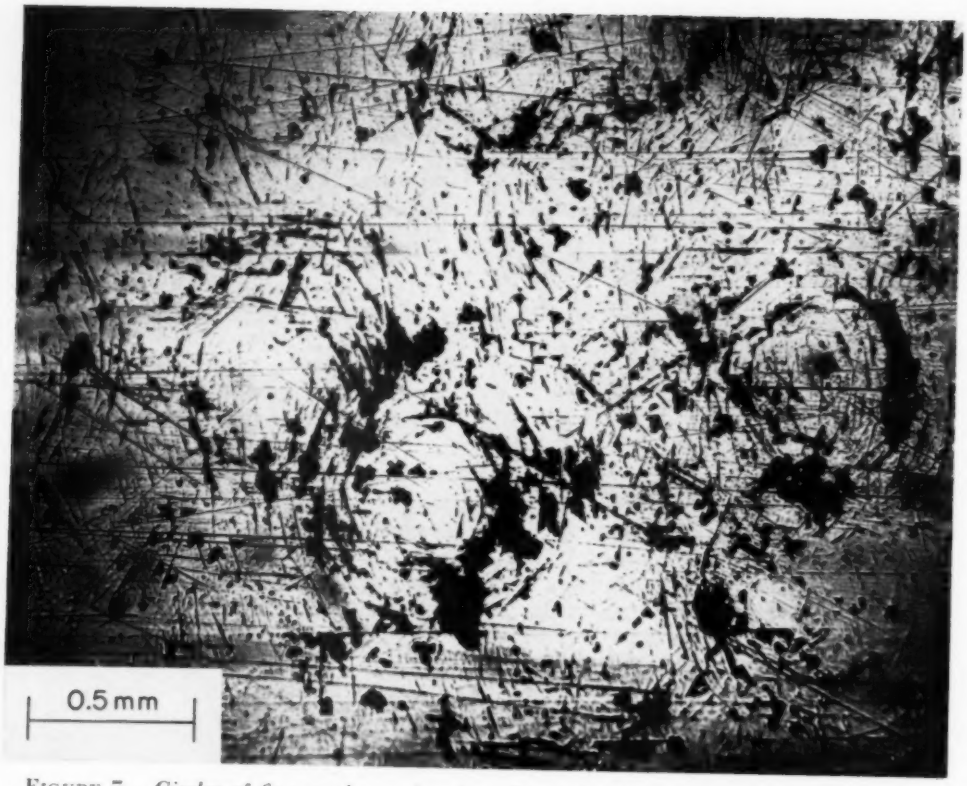

FIGURE 7. *Circles of fine cracks produced on Lucite by high-speed-waterdrop impacts.*

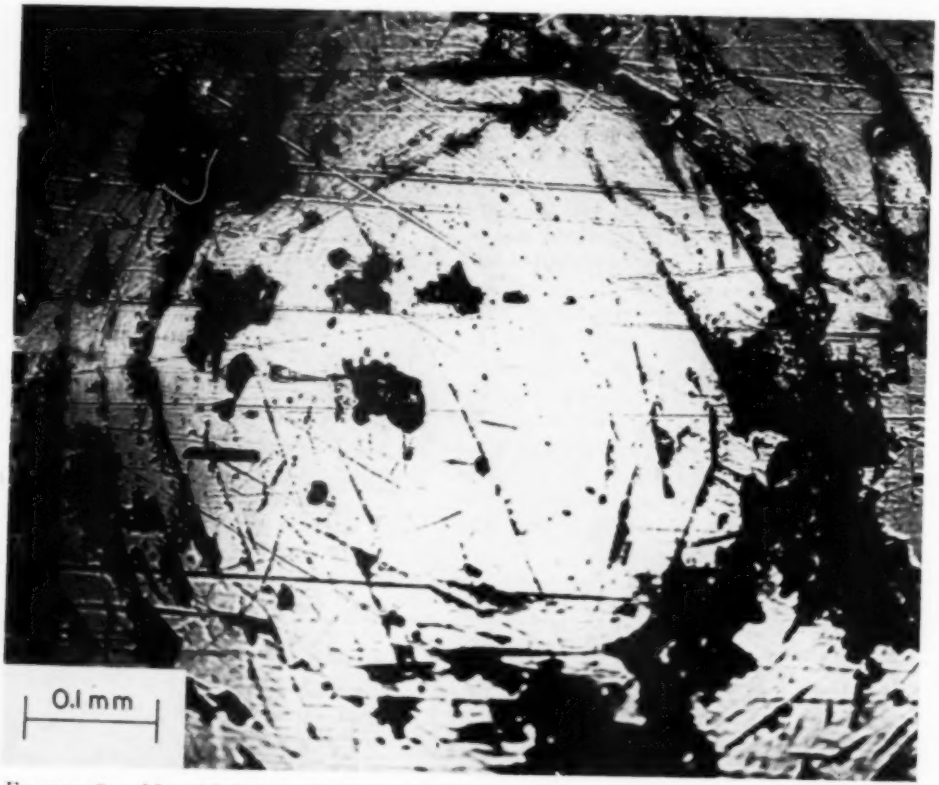

FIGURE 8. *Magnified view of the most prominent circle of fine cracks shown in figure 7.*

3.1. Circular Fine Cracking as a Result of High-Speed-Water Blows

A search for damage sites comparable to those that are observed as a result of impacts of deforming lead pellets was at first unrewarded. Specimens of methyl methacrylate plastic that were rotated at a velocity of 500 mph through 1-in./hr artificial rain at the Cornell Aeronautical Laboratory for periods of 30 to 40 sec were already in an advanced stage of erosion. The first damage sites were obscured by later overlapping impacts, so that nothing could be concluded in regard to their initial configuration. No general pattern was visible, and all that could be concluded from them was that the erosion damage went out from cracks and crack intersections that may or may not have been there before the water struck.

However, individual damage sites could be seen on a specimen similarly exposed for only 25 sec. Figure 7 shows the result. The configurations that stand out in the photograph are the circles of fine cracking. Here again, the circles of parallel lines in tiers can be seen. It is also notable that here again the craze cracks meet at an angle. In figure 7 the widening of these cracks due to the outward flow of the water from the central point of impact can be seen. Direct comparison should be made with figures 2 and 3, where the same configuration of lines and the same widening of cracks can be seen as the result of the impact and flow of deforming lead pellets.

Figure 8 is a higher magnification of the most prominent circle shown in figure 7. In figure 8 the angular meeting of the parallel lines is apparent as is also the widening of the cracks by breaking out of the surface material along them in a direction away from the central point of impact as a result of the radial flow of the water. From figures 2, 3, 7, and 8 the conclusion can be drawn that *the mechanisms of damage produced by the impact of deforming lead pellets and by the high-speed impingement of waterdrops on methyl methacrylate plastic are identical.* The difference between them is one of degree only.

3.2. Comparison of the Destructive Action of the Impact of Lead Pellets and the Impact of Waterdrops

The destructive action of these flowing projectiles is due (A) to the impact of the hard sphere that constitutes the projectile itself, and (B) to the radial flow of the projectile after the collision, as follows:

(A) The first of these two types of damage is the production of a circle of fine cracks. With respect to this type of damage, the impacts of lead pellets are more destructive than the impacts of waterdrops, as can be seen by comparing the amount of fine cracks produced by a single impact in figures 2 and 3 with that produced by a single impact in figure 7. The impact velocity of the lead pellets that produced the damage sites shown in figure 3 was about half that of the waterdrops that produced the damage sites shown in figure 7. The lead-pellet velocity that produced the damage sites shown in figure 3 was appreciably higher than that which produced the damage site shown in figure 2. It is easy to see that the extent of damage observed in figures 2 and 7 is a logical result of the kind of flowing projectile that produced it. The impact pressure that results when a spherical liquid projectile strikes a flat, solid surface that has an infinite modulus of elasticity is given by [2]

$$P=(\alpha/2)c\rho v_0, \tag{1}$$

where P is the impact pressure, α is a coefficient less than unity that arises from the flow property of the liquid projectile, c is the speed of sound in the liquid projectile, ρ is the density of the liquid projectile, and v_0 is the impact velocity. Lead has a much higher density than water and a value of α that is closer to unity. Therefore, according to eq (1), a lead pellet should exert a greater impact stress than a water sphere. The lead pellet should form a deeper depression than the waterdrop does in the surface of the plastic as a result of its collision, should produce more tensile stress in the surface about the depression that it produces, and consequently should produce more fine cracking.

(B) The second type of damage is (a) the widening of the surface cracks and the breaking out of material from the surface, both of which are observed in the damage sites produced by waterdrops as well as in those produced by lead pellets, and (b) the subsurface shear cracks that are observed only in the damage sites produced by the lead pellets. The damage (a) may result from the application of the external torque exerted by the rapid radial flow along the surface against irregularities in the surface. In this connection the raised ridges of the craze, or fine cracks, may be a factor. The damage (b) appears to be due to a shear stress that tends to move the surface layer of the plastic solid with respect to the underlying layers.

Whether the damage caused by the flow as a result of impact of a waterdrop or of a lead pellet is considered more severe depends on the criterion that is taken for the extent of damage. The waterdrop flows out to many times its original diameter and therefore breaks a large amount of material from the surface. The lead pellet flows only to about twice its original diameter and hence is less effective than water in this respect. On the other hand, the shear stress exerted by the flow of the lead is much greater than that exerted by the flow of the water, because it produces subsurface shear cracks, which the water does not produce even when its impact velocity is about double that of the lead. On the basis of its shear stress, therefore, the radial flow of the lead is more destructive than that of the water.

3.3. Shear Stress Due to the Radial Flow of an Impinging Waterdrop

The shear stress, τ, between layers of liquid in laminar flow is given by the product of the viscosity, μ, and the velocity gradient through the moving sheet of liquid perpendicular to its direction of flow. That is,

$$\tau=\mu\frac{\partial v}{\partial z}, \tag{2}$$

where v is the velocity of the sheet of liquid, and z is the direction through the thickness of the liquid sheet. The layer of liquid molecules in direct contact with the solid has zero velocity, but the velocity gradient is not zero, and the shear stress is applied to the solid.

Faust [9] and Hyde [10] have found that the viscosity of liquids not only increases with pressure, but it increases at an increasing rate as the pressure rises. Hence, it seems entirely reasonable to conclude that water impacts will produce subsurface shear cracks at sufficiently high impact velocities, even though they are not observed in the views shown in figures 7 and 8, where the relative impact velocity was 500 mph.

It is possible to estimate roughly the shear stress exerted by the radial flow of a waterdrop that strikes a solid surface at a relative velocity of 500 mph. In developing an equation for the impact pressure under an impinging water sphere [2], it was shown that the thickness, δ, of the sheet of water in radial flow when the pressure is at a maximum is given by

$$\delta=4r(1-\alpha)^2\left(\frac{v_0}{c}\right)^2, \tag{3}$$

where r is the radius of the flattened water sphere, α is a coefficient that arises from the flow property of the liquid and that is very close to unity at high impact velocities, v_0 is the relative impact velocity between the water sphere and the surface that it strikes, and c is the speed of sound in water. The median radius of 1-in./hr raindrops, such as were used in producing the damage sites in figures 7 and 8, is 0.095 cm, so that the radius of the flattened sphere is 9.5 cm. If the coefficient α is taken to be 0.99, then δ is found to be 0.00008 cm.

The average velocity of the radial water flow at the time of maximum pressure also was found [2] to be given by

$$v=\sqrt{c\alpha v_0}. \tag{4}$$

For a relative impact velocity, v_0, of 500 mph, the radial flow velocity, v, is found to be about 58,000 cm/sec. As this is an average value of the radial flow velocity, a rough estimate of the velocity gradient through the radially moving sheet of water can be made by taking it to be equal to $\Delta v/\Delta z$, where Δz is half the value of δ. To this degree of approximation, τ is found to be 210 psi, because the viscosity of water at room temperature is about 0.01 poise. This value is too low because of the increase of viscosity with pressure. From the data of Faust the viscosity of ethyl alcohol increases by a factor of about three for an increase of pressure comparable to the impact pressure that is produced when a waterdrop strikes a solid surface at a relative velocity of 500 mph. If the increase in the viscosity of water, which is also an associated liquid, is about the same as that of ethyl alcohol, then τ is about 630 psi for the radial flow of a waterdrop that strikes a solid surface at the relative velocity of 500 mph. This is below the static shear strength of methyl methacrylate plastic, which is about 8,000 psi [11].

The calculated value of τ is rather sensitive to the value that is chosen for α. The value of 0.99 for α was used in place of the value 0.9, which has been assumed to be the value of α in previous calculations for this magnitude of the relative impact velocity in order to make the shearing stress as high as possible. It will be interesting to know at what impact velocity subsurface shear cracks will be found to be produced experimentally on methyl methacrylate plastic by water blows. This may come to light when a method to produce higher relative impact velocities between a water sphere and a solid surface is developed.

4. Mechanism of High-Speed-Rain Erosion on Methyl Methacrylate Plastic

The effect of high-speed-waterdrop impingement on methyl methacrylate plastic correlates with the damage produced in the parallel study of impacts of steel spheres and especially of the impacts of deforming lead pellets. In the parallel study it was assumed that a cup-shaped cavity is produced in the plastic surface as a result of the compressive load exerted by the impinging projectile. It was further assumed that depressing the surface in this way introduces tensile stresses that, for a brittle material of low tensile strength, produce cracks. In the case of a flowing projectile the cracks are widened, and material is broken out of the surface along the cracks and at crack intersections by the torque that the ultrarapid radial flow exerts.

At high impact velocities a waterdrop behaves like a hard sphere, but unlike a sphere of hard solid material, it retains its liquid property of flow. These properties of the waterdrop under impact conditions make it comparable to the steel sphere and to the deforming lead pellet. It is logical that the mechanism by which it damaged the plastic surface should be entirely comparable to that by which the steel spheres and the deforming lead pellets damaged the surface.

Beal and Wahl [12] have found that for a given relative impact velocity the impingement of waterdrops at a 3-in./hr rain rate, in which the median drop size is 2.5-mm diam, produces more damage than the impingment of waterdrops at a 1-in./hr rain rate, in which the median drop size is 1.9-mm diam. They also found that where three nozzles, each of which produced 1-in./hr rain with a median drop

ue of 1.9-mm diam, were used, the 3-in./hr volume of rain was not proportionately more severe than the 1-in./hr volume of rain if the drop size is the same in each. They concluded that the greater damage produced by the 3-in./hr rain rate with the median drop size of 2.5-mm diam must be due to the larger drop size rather than to the increased number of drops per unit time. In the light of the mechanism that has been postulated, it would follow that this should be the case Comparison of the diameters of damage sites produced by a $\frac{7}{32}$-in. and by a $\frac{5}{16}$-in. steel sphere at the same relative impact velocity and on methyl methacrylate plastic of the same thickness showed that the damage site produced by the larger sphere was the larger (see section 2.1). Similarly, the damage site produced by the average 3-in./hr raindrop will be larger than the damage site produced by the average 1-in./hr raindrop. The 3-in./hr raindrop will also provide a larger volume of water to produce damage in the process of radial flow. It is notable that eq (1) for the pressure produced by the impact of a water sphere against a flat surface is not a function of the drop size.

Although it would appear that the rain-erosion mechanism on methyl methacrylate plastic has been explained by this study, one cannot safely extrapolate the result to *all* other brittle plastics of low tensile strength. As pointed out in section 1, the erosion mechanism is not only a function of the impact properties of the waterdrop, but it is also a function of the specific properties of the solid material against which the waterdrop impinges. The mechanism that has been postulated for methyl methacrylate plastic can be extrapolated with safety only to other brittle plastics of low tensile strength having other characteristic properties that are comparable to those of this plastic. Furth and Born [13] have advanced the concept that breaking is a form of melting: "melting being nothing else than a breaking due to the action of the heat movement of the atoms; or putting it the other way round, breaking is nothing else than melting enforced by the action of the stress" (see also references [14, 15, 16]). If this concept is correct, a brittle plastic of low tensile strength that differs appreciably from methyl methacrylate plastic either in heat conductivity or in actual melting temperature could respond in a very different manner to the high-speed-water blows.

The author thanks George Irwin of the Naval Research Laboratory for suggesting the parallel study, and Herschel L. Smith and Mark Bowman of the Naval Research Laboratory for making the shots with steel spheres and deforming lead pellets on Plexiglas I–A.

The work described in this paper was sponsored by the Wright Air Development Center. The results that are given were taken from a report submitted to that agency. Their assistance and interest are gratefully acknowledged.

5. References

[1] Olive G. Engel, Wright Air Development Center Technical Report 53-192, Part 2 (August 1953).
[2] Olive G. Engel, Wright Air Development Center Technical Report 52-192, Part 1 (July 1953).
[3] H. Schröter, Z. Ver. Deut. Ing. **80,** 479 (1936).
[4] Mark Bowman, H. L. Smith, and J. A. Kies, N.R.L. Mem. Report 181 (June 1953).
[5] S. B. Newman and Irvin Wolock, (publication pending).
[6] D. J. McAdam, Jr., G. W. Geil, and W. D. Jenkins, Proc. ASTM **47,** 554 (1947).
[7] A. A. Griffith, Trans. Roy. Soc. (London) **221** [A] 163 (1920–21).
[8] H. L. Smith (publication pending).
[9] O. Faust, Z. physik. Chem. **86,** 179 (1914).
[10] J. H. Hyde, Proc. Roy. Soc. (London) **97** [A] 240 (1920).
[11] Plexiglas Handbook for Aircraft Engineers (Rohm & Haas Co., 1951).
[12] John L. Beal and Norman E. Wahl, Air Force Technical Report 6190 (1951).
[13] R. Furth and M. Born, Nature **145,** 741 (1940).
[14] M. Born, J. Chem. Phys. **7,** 591 (1939).
[15] R. Furth, Proc. Roy. Soc. (London) **177** [A] 217 (1941).
[16] R. Furth, Proc. Cambridge Phil. Soc. **37,** 34 (1941).

Washington, August 31, 1954.